Phenomena Associated with Individual Discharges during Plasma Electrolytic Oxidation

Samuel Christopher Troughton

Robinson College

Department of Materials Science and Metallurgy

University of Cambridge

This dissertation is submitted for the degree of Doctor of Philosophy

August 2018

Preface

This dissertation is submitted for the degree of Doctor of Philosophy at the University of Cambridge. The research described herein was carried out by myself in the period from October 2014 to August 2018, under the supervision of Professor T.W. Clyne, in the Department of Materials Science and Metallurgy at the University of Cambridge.

I hereby declare that, except where specific reference is made to the work of others, the contents of this dissertation are original. No part of this dissertation, or any similar to it, has been, or is currently being submitted for consideration for any other degree or qualification at any other University or similar institution. This dissertation is the result of my own work and includes nothing which is the outcome of work done in collaboration except where specifically indicated in the text and Acknowledgements. It is fewer than 60,000 words in length.

Samuel C. Troughton

Abstract

This work presents information obtained from high-speed video and electrical monitoring of electrical breakdown (discharge) events during plasma electrolytic oxidation (PEO) of aluminium alloy substrates. Discharges were found to occur in extended sequences termed “cascades” at particular locations. This was a feature common to all the substrates and processing frequencies investigated. As the coating thickness increases, the characteristics remained broadly similar, although discharges become more energetic and longer-lived.

Short PEO treatments were applied to existing PEO coatings in order to investigate the microstructural effects of discharge cascades. It was found that cascades persist at particular locations due to the residual deep pore channel left by previous discharges in the cascade. Observations were made of the way the coating was restructured around a cascade location.

Samples were illuminated with very high intensity flashes during PEO processing, revealing that relatively large (1 mm diameter) bubbles form where a discharge emerges from the surface of a coating. Analysis of the overall energy consumption, as well as the energetic processes occurring within an individual discharge, indicate that the bubble growth occurs due to rapid volatilisation of water originating from the electrolyte. It is postulated that the growth of this bubble causes the electrical resistance to rise and is responsible for the termination of the discharge current.

Investigations of high frequency (2,500 Hz) processing lead to the discovery of discharges occurring during the cathodic half-cycle, after a certain coating thickness had been achieved. Cathodic discharges were more energetic than anodic discharges, and created large craters in the coatings. Gas evolution was found to exceed the electrochemical Faraday yield, and was similar at low and high frequency initially. Once cathodic discharges began, the gas evolution rate increased and the coating mass gain levelled off.

Acknowledgements

I would particularly like to thank my supervisor, Professor Bill Clyne, for his invaluable support, guidance, and advice throughout this project, and, of course, for all the summer BBQs and punt trips. He has created an environment within the Gordon Lab that has been a welcoming and fun place to conduct research. Elsewhere in the department there have been a number of people who have helped make this project possible, particularly Kevin Roberts and Sue Gymer in the Process Lab, Bob Stearn in the Gordon Lab, all the workshop personnel, and Giovani Orlando who was always willing to help fix equipment after (small) electrical fires. Additionally, I would like to thank Dr Steve Hutchins and Dr Robin Francis of Keronite for technical discussions and their enthusiasm for PEO.

I gratefully acknowledge the financial support of the Sims Fund and Scholarship, and the financial and technical support of Keronite International Ltd.

This project really would have been very different without my collaboration with Dr Alexandre Nominé and Mrs Anna Nominé. They introduced me to high-speed photography in the first month of my PhD, discussed crazy experimental ideas, and were always willing to travel to Cambridge on the X5 bus from Milton Keynes for three experimental campaigns which contributed to the work in chapters 5 and 6. Additionally, I have worked with two summer students, Jeremy Duan and Jamie Bragg (Jeremy even decided to continue with a Part III project), helping produce work for a

paper on Ti PEO for photocatalysis, and work on cathodic discharges and gas evolution respectively.

All of the members, both past and present, of the Gordon Lab have made their mark over the past few years, making this an unforgettable experience. Particularly Catalina, Joe, and Rob for being welcoming when I first started, and Tom, Max, Matt, Amy (even though she is in Rolls Royce), Julia and everyone else for all the enjoyable pub/punt/BBQ/spoons trips and events. Lastly, Jimmy should get his own sentence (very needy), for having been with me through the whole Cambridge journey—doing Robinson, Natural Sciences, Materials, and PhDs in the Clyne group together—thanks for the good times and friendship.

Outside of the Lab there are a number of people and clubs to thank, all of whom helped kept me sane throughout. I should acknowledge my boatie past, including everyone in the crews that won a Uni IV blade and Lent bumps blade during the first year of my PhD. Coaching the college boats is still a great distraction, and convenient excuse to attend BCD. The Pool Club, for evenings in various Cambridge pubs and my first Varsity win! However, special thanks are due to all the members of CURUFC, who have made the last two years an awesome experience, particularly the 22 other guys in the final Varsity squad. GDBO.

Finally, I would like to thank my parents for all the support and encouragement they have provided me with during my PhD.

Contents

Nomenclature

Roman Symbols

C_P	Specific heat capacity
D	Diameter
E	Energy
E_g	Electronic band gap
G	Gibbs free energy
H	Enthalpy
I	Current
P	Pressure
Q	Energy to vaporise a certain mass of material
R	Resistance
R_a	Arithmetic mean roughness
T	Temperature
V	Voltage
f	Frequency
i	Current density
m	Mass
n	Number of moles
r	Radius
t	Time
v	Volume
x	Coating thickness

Greek Symbols

γ	Interfacial energy
ε_r	Dielectric constant
μ_L	Kinematic viscosity
ρ	Resistivity
ρ_L	Liquid density
τ	Time period
$\varnothing$	Diameter

Subscripts

a	Anodic
B	Bubble
c	Cathodic
event	Discharge event
init	Initiation
p	Plasma
peak	Peak

Acronyms

AC	Alternating Current
BP	(Pulsed) Bi-Polar
BSE	Back-Scattered Electron
DC	Direct Current
EDX	Energy Dispersive X-ray (spectroscopy)
FPAC	Full Power Alternating Current (testing)
LPDCT	Low Power Direct Current Testing
LTE	Local Thermal Equilibrium
MAO	Micro-Arc Oxidation

OES	Optical Emission Spectroscopy
PEO	Plasma Electrolytic Oxidation
RMS	Root Mean Squared
SEM	Scanning Electron Microscopy
SE	Secondary Electron
TEM	Transmission Electron Microscopy
XRD	X-Ray Diffraction

Chapter 1

Introduction

Plasma electrolytic oxidation (PEO) is a method for producing thick, protective oxide coatings on metals such as aluminium, magnesium, and titanium. Coatings are strongly adhered to the substrate, and complex geometries can be coated easily. The coatings enhance tribological performance and corrosion resistance, enabling these metals to be used in demanding applications. PEO has similarities to conventional anodizing, but the applied potentials (typically a few hundred V) and current densities (tens of A dm^{-2}) are higher and the coatings are thicker. The process has been called microarc oxidation (MAO), spark anodizing, anodic spark deposition or microplasma oxidation, but plasma electrolytic oxidation has become the predominant term and will be used in this work.

During the process, a substrate is suspended in an electrolytic bath and connected to a power supply. The applied potential is raised above the breakdown potential of the oxide coating, causing through-thickness electrical discharges, which produce visible sparks on the surface. Each discharge constitutes a plasma, which facilitates oxidation (via thermal, anodic and plasma-chemical reactions) of the substrate, with the possibility of deposition of elements from the electrolyte, to form an oxide coating.

PEO is now a relatively well-established industrial process. The current market leader, in terms of supply of PEO technology is Keronite (UK), although activity is global, with available products including those from Ceratronic (France), Kepla-Coat/Magoxid-

Coat (Germany) and Tagnite (USA). Despite this industrial development, the process is rather poorly understood, and developments are largely based on empirical observations and trial and error. Currently, around half of all the coatings produced by Keronite require additional post process treatments, such as polishing to remove a porous outer layer or sealing of porosity to enhance corrosion resistance. The PEO process is very energy intensive, and inefficient considering that it is thermodynamically favourable to covert these metals into their oxides.

1.1 Applications

PEO coatings are attractive for many applications requiring resistance to sliding or abrasive wear. The main attributes of PEO coatings making them suitable for such applications are their high resistance to spallation (due to strong adherence to the substrate and relatively low macroscopic stiffness), and high hardness conferred by crystalline phases.

There has been a lot of work on optimization of the wear resistance of PEO coatings [1-8], focusing on many different control variables, although the majority of such studies present empirical outcomes, rather than identifying the key microstructural features and the mechanisms by which they are being manipulated.

PEO coatings are also commonly employed for corrosion protection, and there are many reports of considerable enhancement to corrosion resistance over uncoated metal substrates [9-12]. This is particularly true for Mg alloys [13-17], which are often very vulnerable to corrosive degradation without surface treatment. There are many examples of improved corrosion resistance being obtained through changes in electrolyte composition or processing parameters, although these are often just empirical outcomes, specific to particular environments. It may also be beneficial to ensure that fluids cannot readily penetrate into the coating and various kinds of surface sealing operation are routinely employed, such as painting or impregnation with a polymer.

Ti is known to be a highly biocompatible material, which means that it is actually the titania native oxide on the surface that is biologically benign. In particular, bone cells have a high affinity to titania, and tend to grow into porous regions of it, or at least adhere well to them and proliferate effectively on them. This is relevant to the production of strong bonding between (Ti alloy) implants and surrounding bone tissue. The idea of creating a highly porous TiO_2 coating using PEO, or even incorporation of bioactive phases such as hydroxyapatite into the coating, has been around for a number of years. There are numerous studies on the topic [18-22], although it is yet to be employed commercially.

There is also strong interest in Mg as a biomedical material [23]. Magnesium ions are necessary for many biological processes in living cells, so that, in general, corrosion products are not inherently harmful. Additionally, the mechanical properties (particularly the density and Young's modulus) of Mg alloys are a closer match to bone than those of Ti alloys. However, corrosion of Mg alloys can be very fast, generating excessive hydrogen and causing harmful local changes in pH. PEO coatings can be used to improve corrosion resistance, and can enhance biocompatibility by incorporating calcium and phosphorus from the electrolyte [24-28].

TiO_2 is also known to be a very effective photo-catalyst, for oxidation of various organic pollutants and pathogens, under the action of suitable radiation [29]. It is common to use UV radiation, but certain measures, such as the introduction of Ag nanoparticles into the surface [30], allow longer wavelength (visible) radiation to be effective. As with bioactivity, this has been known for a long time and the possibility of a Ti PEO surface being attractive, in view of its high specific surface area, and its potential for the creation of robust structures, was proposed some time ago. There have been many investigations [31-37], with the potential now well established. The anatase phase of TiO_2 is thought to be more effective than the rutile phase [38] and, with this effect in mind, there have been studies [39] in which efforts have been made to raise the anatase content of PEO coatings.

1.2 Research aims and thesis structure

Progress has been made in recent years on the characterisation of coating properties, including porosity, stiffness, and thermal characteristics. Some of these attributes, as well a brief overview the PEO process (including details of the systems used) are presented in Chapter 2. Understanding of the actual mechanism by which the process proceeds is still limited. Without this fundamental knowledge, improvements and control over the coatings produced can only occur by comparing large numbers of different processing conditions. This is time-consuming, expensive, and does not guarantee that the optimal conditions will be found.

Therefore, the aim of this project is to improve the current understanding of the fundamental mechanisms involved in PEO process. The discharge events strongly affect the microstructure and properties of the coating. Chapter 3 reviews the literature focused on individual discharge characteristics, and the suitability of metals to undergo PEO processing.

Chapter 4 presents the experimental methods used in this work. The main experimental developments employed here were the use of synchronised high-speed video and electrical monitoring, as well gas evolution monitoring.

Establishing a correlation between individual discharge events and microstructural features would allow improvements to the final coating properties to be made. Chapter 5 presents the results of high-speed video, and high-speed video synchronised with electrical monitoring work on aluminium, in which short PEO treatments were applied to investigate microstructural effects of discharge cascades. Implications for the discharge mechanism are also discussed.

Chapter 6 examines the formation and kinetics of the gas bubble that forms around a discharge site. Analysis of the energetics of individual discharges is performed, to determine how the large amount of electrically injected energy is consumed. This provides scope for future work that aims to reduce the energy consumption of the process.

It has been widely reported in the literature that PEO coatings produced under alternating current conditions produce superior (harder, more dense) coatings. However, the through-thickness electrical discharges are predominantly reported to occur only under anodic polarisation. Chapter 7 presents investigations of high frequency processing, which was found to induce discharges during the cathodic half-cycle. The microstructural effects are examined and the gas evolution is monitored. The processes occurring at high frequency and during the cathodic half-cycle are discussed.

The conclusions and further work are presented in Chapter 8.

Chapter 2

The Plasma Electrolytic Oxidation Process

The following provides a brief overview of the systems used to produce PEO coatings, as well as the structure and properties of PEO coatings. There are a large number of variations, with almost every research group using a different set-up, and often employing more than one. The basic similarities are that the component to be coated must be connected to a power supply and submerged in an electrolytic bath containing a counter-electrode, often a stainless steel mesh, or the tank itself. The electrolyte is circulated through a heat exchanger to maintain an approximately constant electrolyte temperature, and ensure good mixing of the electrolyte. Variations come in the form of the power supply, processing time, and electrolyte composition, which are discussed in the following subsections.

2.1 Background and development

The PEO process originated from anodizing, and the experimental set-up is broadly similar. During anodizing, a voltage (~10–80 V) is applied between the work-piece and an inert cathode. Certain metals, such as Al, Mg and Ti, form an oxide coating on their surface in an electrochemical process. Coatings often have a columnar structure, containing nano-scale pores, but can be produced with a sponge-like morphology or as a barrier layer, depending on the electrolyte composition and processing conditions. Anodized coatings tend to be largely amorphous or partially amorphous with fine-grained crystalline regions.

PEO employs higher voltages (~250–750 V), usually operating with an AC electrical supply. The high voltage causes repeated dielectric breakdown (conventionally during the anodic half-cycle) through the thickness of the growing oxide layer, creating multiple, short-lived, electrical discharges which are distributed over the surface of the work-piece. Oxidation is not via an electrochemical process in the case of PEO; instead, metal and oxygen atoms or ions combine as the plasma, that is created by each discharge, cools and collapses. This allows thicker coatings with higher crystallinity to be formed. This often results in harder, more wear-resistant coatings.

2.2 PEO processing

2.2.1 Power supply and electrical parameters

A component is suspended in an electrolytic bath and connected to a power supply. This can be a simple direct current (DC) supply, mains frequency alternating current (AC) supply, or a pulsed, variable frequency, supply, either uni-polar (anodic pulses only) or bi-polar (BP) (alternating anodic and cathodic pulses). Schematics are shown in Figure 2.1. Operation may be under constant voltage (potentiostatic), constant current (galvanostatic) or constant capacitance conditions. Simple DC power sources are not commonly used, since there is little control over discharge processes and they produce inferior coatings to AC or pulsed sources [40].

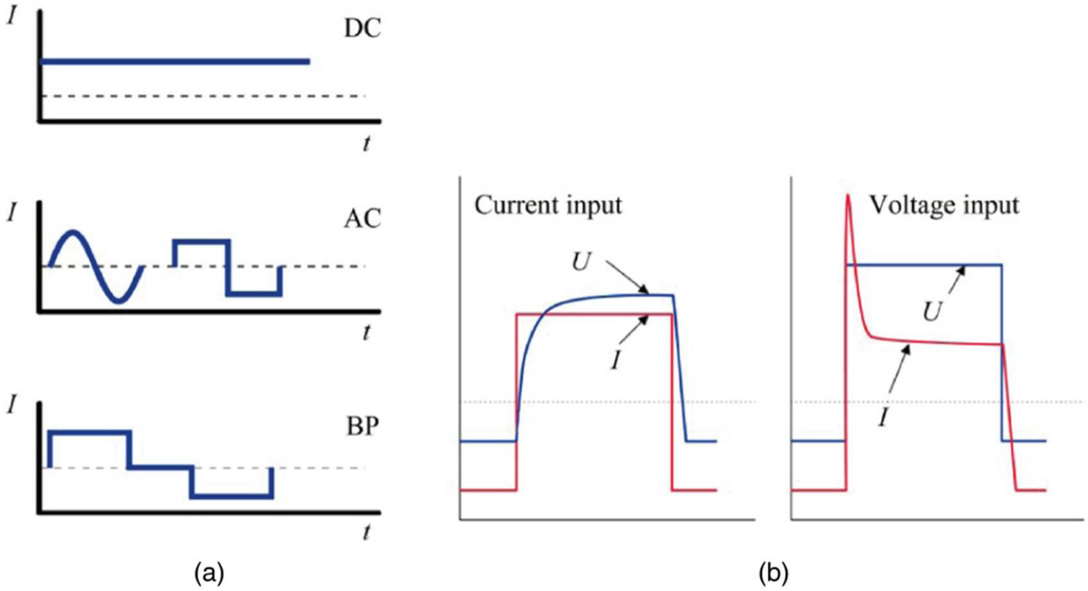

Figure 2.1 Schematic power supply modes used in PEO processing (a), and representations of current and voltage controlled signals (b), from [**41**].

Figure 2.2 shows a typical 50 Hz AC processing rig, which is often used in laboratory or small scale industrial settings, although pulsed square waveforms and higher frequencies are being increasingly exploited in research and in commercial use. The system is relatively simple with only the processing variables being time and applied current density, which is usually in the region of tens of A dm^{-2}.

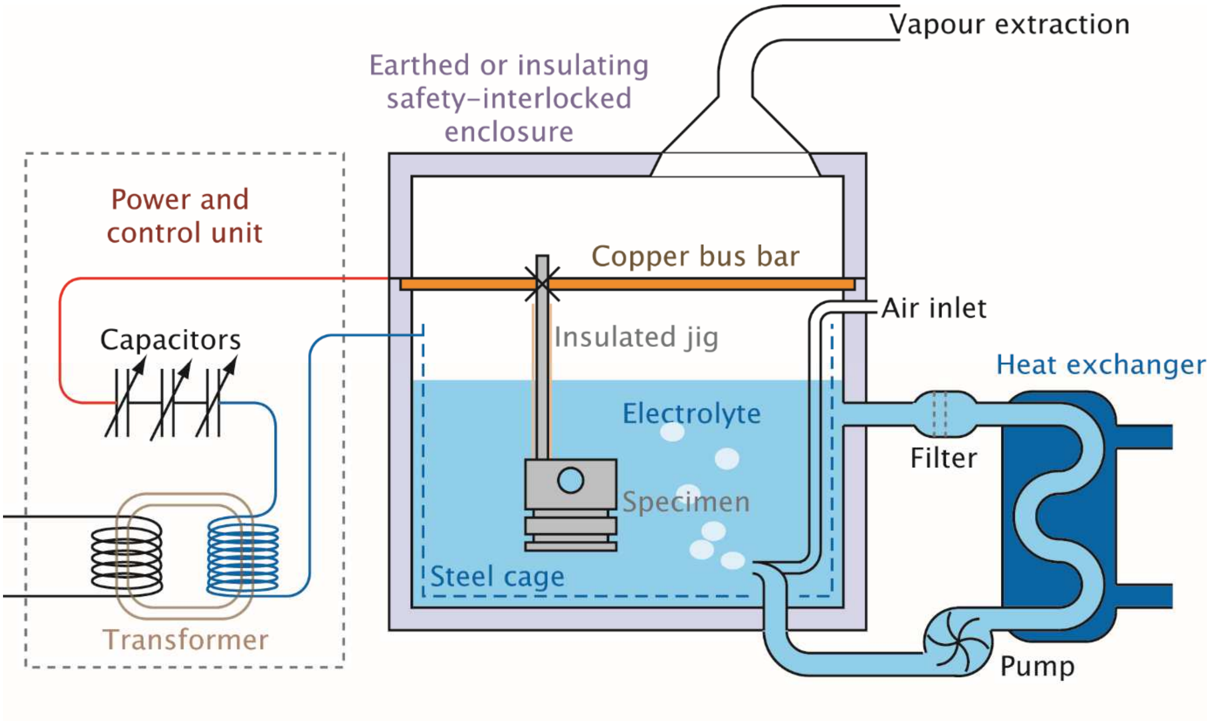

Figure 2.2 Schematic of a 10 kW Keronite™ processing rig [42].

A typical example of the bulk electrical waveform for 50 Hz AC processing of aluminium is shown in Figure 2.3. An initial sharp rise in the applied potential is followed by a much more gradual increase after around one minute of processing. This is a common feature in PEO processing. The initial rise is attributed to thickening of the native oxide layer by conventional electrochemical processes, before the onset of discharges as the voltage levels off. The important point to note here is that the growth rate of PEO coatings is usually linear with processing time (see §2.3.2), but the applied potential does not scale in the same way. The PEO process involves local dielectric breakdown of the coating. In order to maintain the necessary electric field across the coating, one would expect the potential to increase linearly with coating thickness. One interpretation of this is that breakdown actually only occurs across a thin barrier layer at the substrate-coating interface. This is further discussed in §2.3.3 and §2.3.4 in relation to the microstructure and porosity of PEO coatings.

In recent years, pulsed sources have become more popular, due to the greater degree of control [43-46]. Parameters including frequency, current, voltage, and duty cycle (ratio of the anodic time period to the total time period) can all be varied independently. A study by Yerokhin et al. [44] compared coatings produced on aluminium using 50 Hz AC source and pulsed bi-polar source in the kHz range. The energy consumption per unit thickness of coating for the pulsed bi-polar source was lowest between 2 and 3 kHz, but was still higher than the reference 50 Hz coating. However, the bi-polar coating was denser and surface roughness was reduced. Hussein et al. [46] found that coatings produced using a pulsed bi-polar supply were more compact and less porous than those produced using a pulsed uni-polar supply.

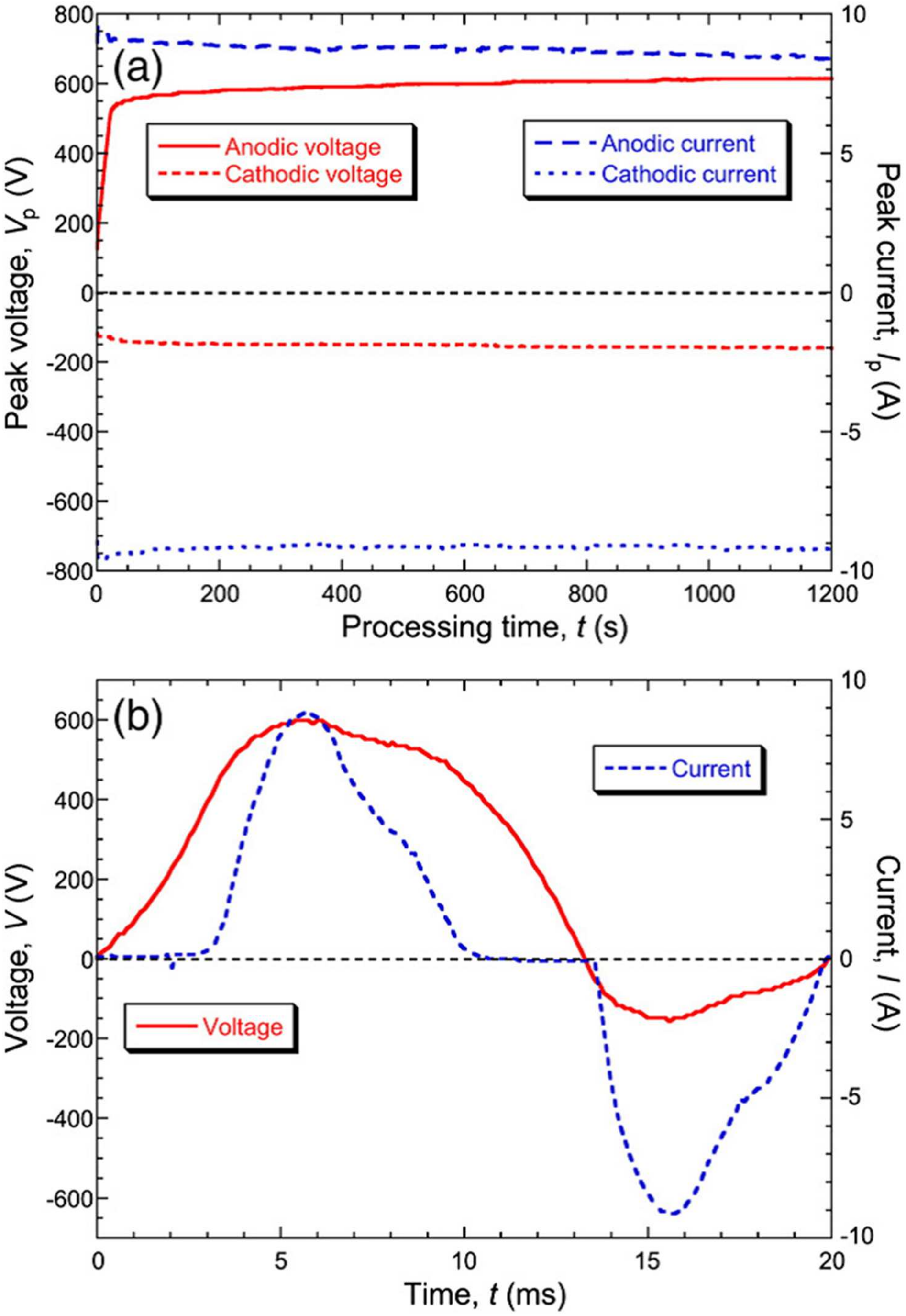

Figure 2.3 (a) Typical variation of the peak anodic and cathodic voltage and current during the first 20 minutes of PEO processing and (b) voltage and current waveforms during a single cycle, after 10 min of processing. Reproduced from [47].

2.2.2 Electrolyte Composition and Additives

Electrolyte compositions used in PEO vary widely according to the substrate and application. There is considerable potential for influencing the nature of discharges, as well as the resultant microstructure, by altering the electrolyte composition. Electrolytes are generally a dilute alkaline solution, with pH values reaching up to ~13, which have significant environmental advantages over the strong acids and chromate-based electrolytes used in conventional anodizing. It is not entirely clear why a high pH is optimal for PEO, particularly since anodizing is often carried out in acidic electrolytes. Furthermore, it is possible to perform PEO in acidic electrolytes, particularly for Ti [48-51]. The electrolyte conductivity is also significant, since it affects current flow [52] and voltage drops across columns of electrolyte in pores within the coating, and can thus have an influence on the ignition of discharge plasmas [53, 54]. Conductivity values are commonly in the range 5-100 mS cm^{-1}.

Electrolytes typically contain sodium or potassium hydroxide (~1–10 g L^{-1}) with additions of silicates, phosphates, and/or aluminates. The purpose of the NaOH or KOH is to increase electrolyte conductivity and create an alkaline solution in which silicates are stable. Silicates, phosphates and aluminates promote passivation of the metal surface, which would otherwise dissolve in the alkali solution [55]. However, many other species have been added to electrolytes such as fluorides (particularly for Ti), borates, and acetates [56].

The role of the chemical species added to the electrolyte goes beyond simply changing the pH and conductivity of the bath. Species are likely to enter the discharge plasma, where they may influence reactions such as oxidation, and become incorporated in the coating themselves. The colour, for example, can be influenced by the species in the electrolyte with reports of yellow [57], green [58], grey [59], red [60], blue [61] and black [62-64], among many others, being created with certain chemical additions. Other features, such as surface roughness, hardness, and reflectance, have also been reported to be affected by certain additions. However, the vast majority of these observations are simply empirical and are difficult to decouple from other parameters such as coating thickness. It has also been noted [65] that “ageing” of electrolytes can influence the PEO process. This is unsurprising, since there is considerable scope both for chemical changes to take place over time in unused electrolyte and, during use, for species from the substrate to enter the electrolyte in some form, with potential for contamination effects. It is common practice to use freshly prepared electrolytes where practicable, although clearly this can be difficult in an industrial environment.

There have been various attempts to incorporate additions such as fine particulate into PEO coatings, by adding them to the electrolyte. A review is available [66] concerning this type of measure. Depending on a number of factors (chemical, physical and electrical), particles may simply become physically entrapped in the coating as it grows or may undergo reactive incorporation. Some success has been reported [11, 67-71] for such measures, although there will commonly be a danger that such dispersions are damaged or removed during the restructuring associated with repeated discharge formation. Nevertheless, it is clear that in some cases even very fine particulate can be successfully introduced into PEO coatings in this way.

2.3 Coating Structure and Properties

2.3.1 Free surface morphology

Electron microscopy is usually employed to examine the free surface of PEO coatings. This provides useful information on the conditions experienced by the coating during the PEO process. PEO surfaces have a characteristic appearance, containing relatively coarse pores or discharge channels (~few microns diameter) surrounded by a smooth circular “pancake” structure, which is attributed to the discharges. The central pore is created as coating material is vaporised during a discharge and the surrounding pancake is created by local melting and re-solidification of the coating material caused by the high temperature plasma. An example of the evolution of the free surface structure with processing time is shown in Figure 2.4, which shows the size of the discharge channel and surrounding pancake structure increase with processing time until finally the discharges become too violent and the structure becomes very inhomogeneous. Radial cracks are often seen in the melt-pool structures. These cracks are caused by thermal stresses generated by rapid cooling of the oxide once a discharge has extinguished, see Figure 2.5. Under standard conditions diameters were found to increase linearly with processing time, as shown in Figure 2.6 [45, 72].

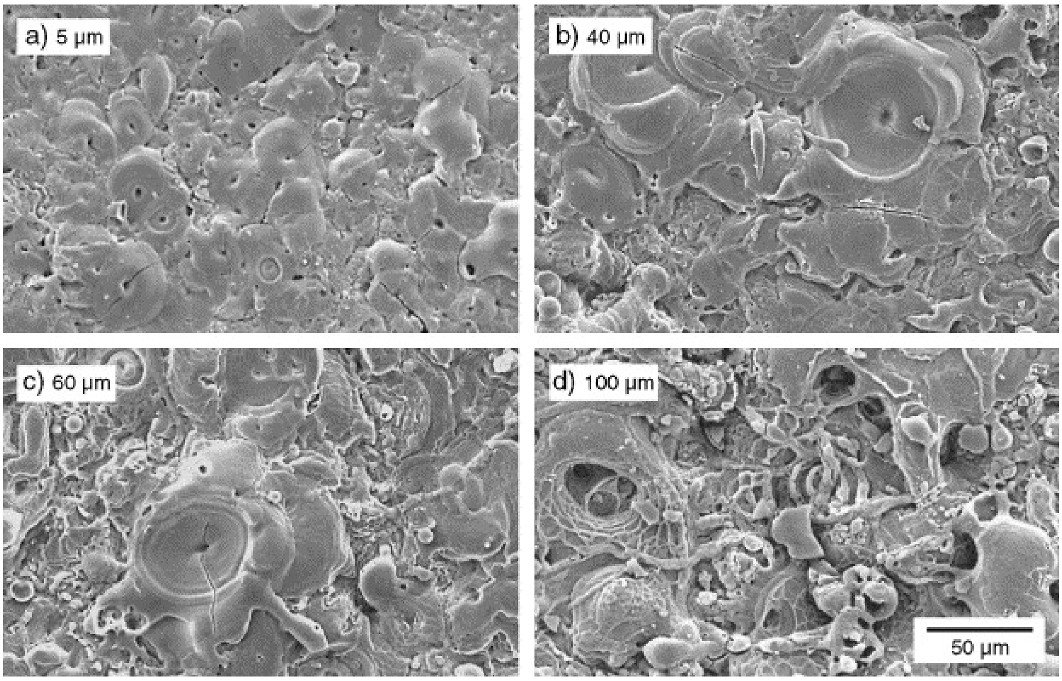

Figure 2.4 SEM micrographs showing free surfaces of coatings with different thicknesses, revealing trends in surface topography. Reproduced from [73].

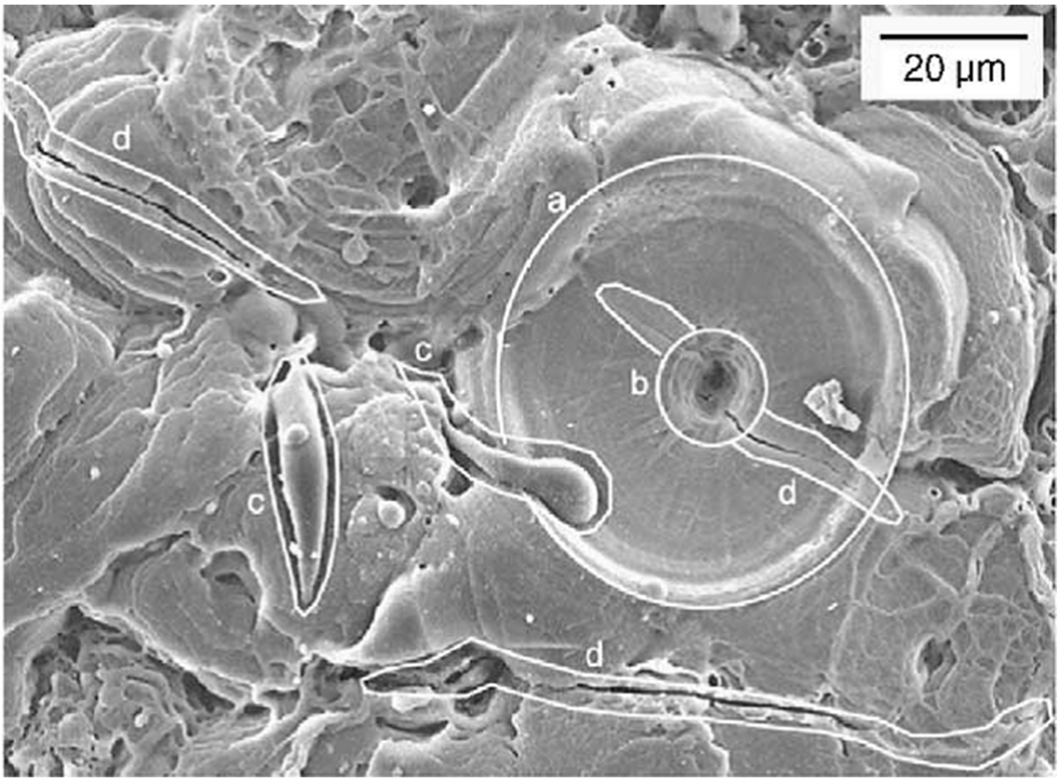

Figure 2.5 An SEM micrograph showing typical features of the free surface of a 40 µm thick coating. These include (a) a re-solidified pool or crater, (b) the central sink-hole ("pipe") in such a pool, (c) material ejected from such pools and (d) localised microcracking. Reproduced from [73].

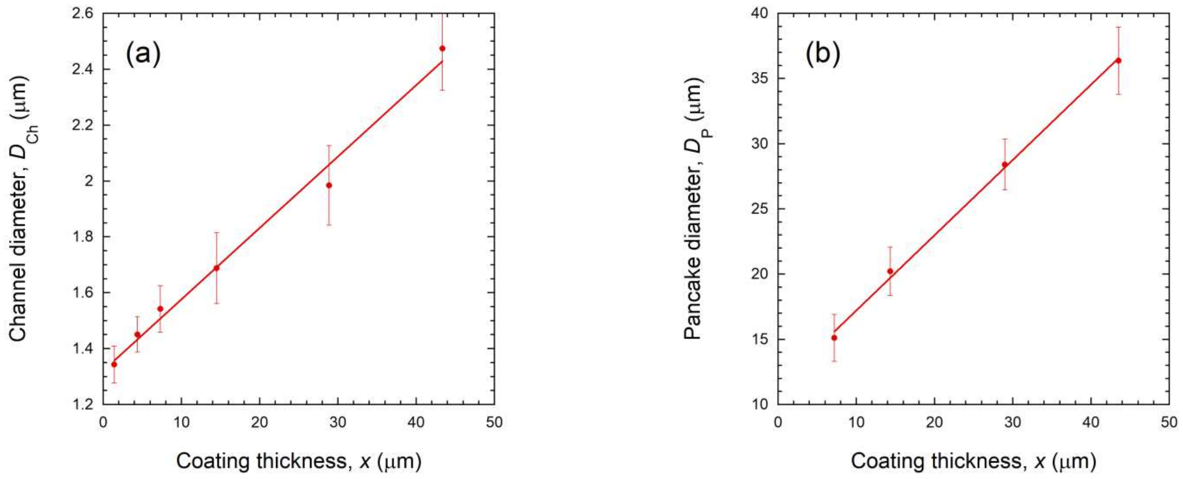

Figure 2.6 Variation in diameter of the discharge channels (a), and "pancake" diameter (b) as a function of PEO coating thickness. Figure produced using data taken from [72].

The surface roughness of PEO coatings is commonly evaluated, and used to as an indication of the scale of discharge events that occurred during the process. The arithmetic mean roughness, R_a, is widely reported to increase with process time [72]. Curran and Clyne [73] found R_a (averaged from three 150 μm × 110 μm areas) increased approximately linearly up to coating thicknesses of ~80 μm, when it levelled off at around 8 μm. Dunleavy et al. [74] correlated the upper bound of the plasma energy with the coating roughness, showing that R_a provides a reasonable measure of the energy associated with discharges. The results are shown in Figure 2.7, along with the variation in coating thickness across a sample. Martin et al. [43] found that roughness increased towards the edges of samples, although there was also an increase in coating thickness towards the edges of samples.

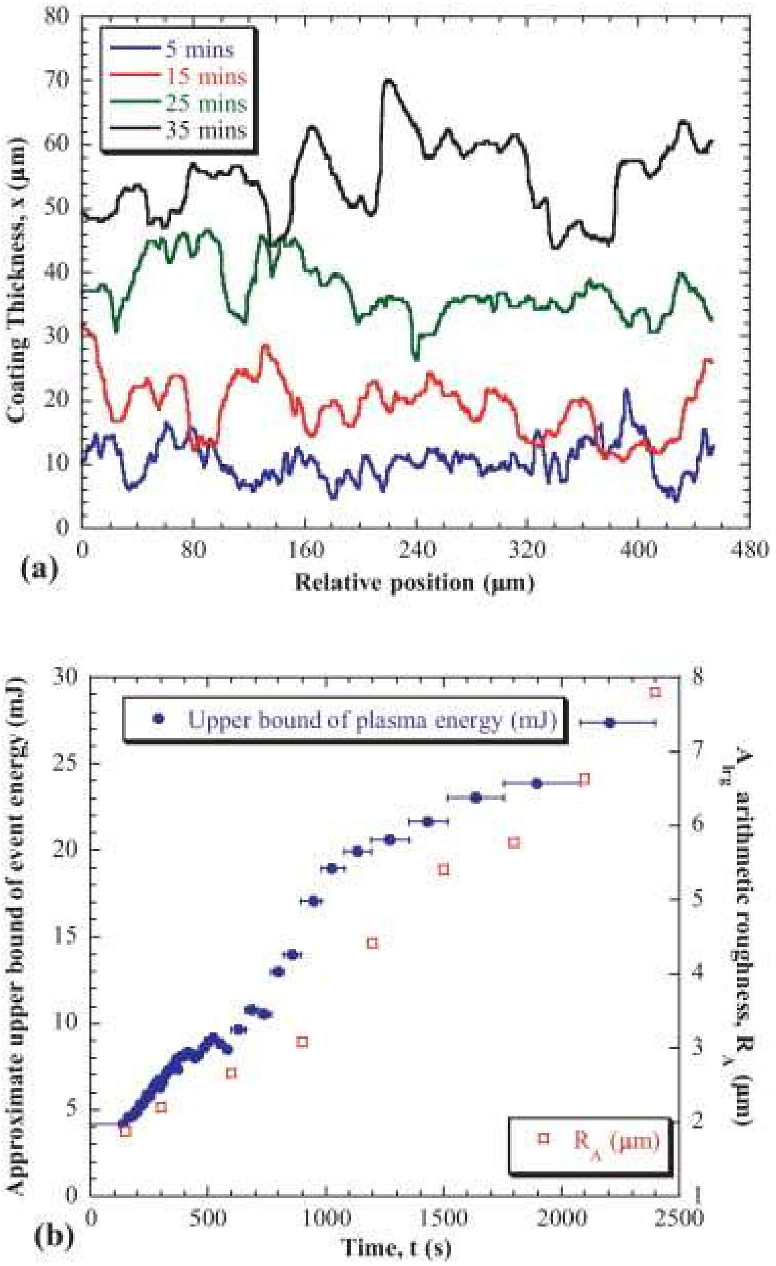

Figure 2.7 Segments of coating thickness profiles for different processing times (a), and estimated upper bound of electrical energy, E_{up}, supplied to a plasma discharge against coating arithmetic roughness, R_a (b). Reproduced from [74].

2.3.2 Growth rates

There is a large body of evidence in the literature that PEO coating thickness increases approximately linearly with process time, up to ~100 µm coating thickness [43, 72, 75-77]. Comparison of growth rates is difficult, due to the huge variations in experimental conditions used by different authors. Electrolyte composition, electrical conditions, substrate composition, and geometry all cause variations in the growth rate. However, the approximate growth rates reported range from a few hundred nm to several μm per minute. Certain electrical conditions can cause deviations from linear growth rates, which usually involve a pulsed power supply [44, 78].

2.3.3 Internal microstructure

Typically, coating cross-sections are examined using electron microscopy. It is often reported that coatings have a two-layered structure, with the outer layer described as loose, porous, or friable and the inner layer descried as dense, compact, or functional [79]. The ratio of thickness of these two layers is often taken as a measure of the quality of a coating. However, the distinction between these layers is highly subjective. When viewed using a secondary electron image, cross-sections can appear homogenous and dense. However, polishing of cross-sections often masks the true structure of the coating, which becomes apparent when viewing the equivalent back-scattered electron image. A network of relatively coarse pores and cracks is revealed in a back-scattered electron image, see Figure 2.8. It should be noted that PEO coatings are continually restructured, and the observed structure was actually only generated by the most recent discharges. Therefore, any layered structures are a result of the last few discharges rather than being built up over time.

TEM studies suggest that there is a thin (few hundred nm) amorphous "barrier" layer between the substrate and coating material on Al, Mg, and Ti [51, 75, 80-82]. In the coating material above the barrier layer, a combination of nanocrystalline material, amorphous material, and fine scale (nm) porosity can be seen. The authors attributed this porosity to the production of oxygen or hydrogen during processing via electrochemical reactions. Porosity of PEO coatings is discussed further in §2.3.4.

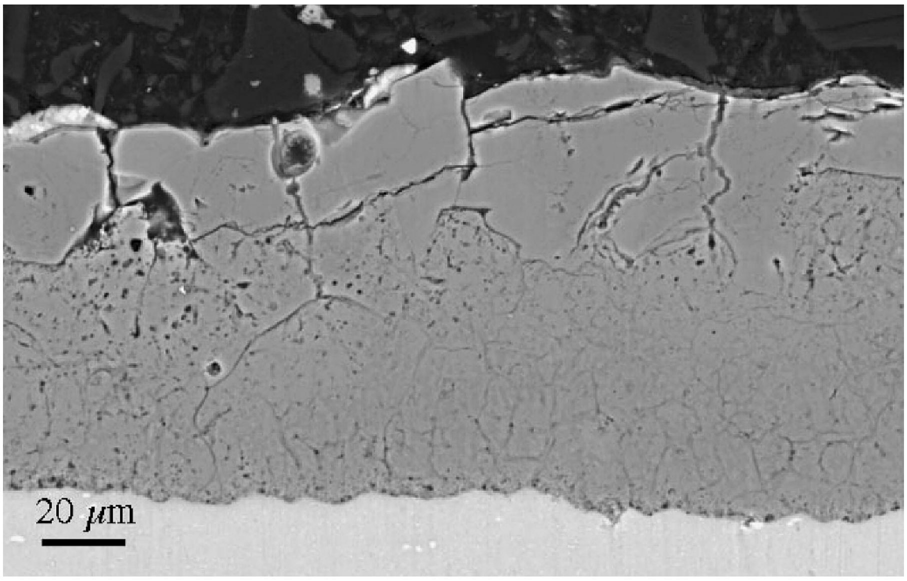

Figure 2.8. SEM image (back-scattered electron mode) of a polished section from a PEO coating on an aluminium alloy substrate, showing the fine network of channels created by individual discharge events, apparently representing a porosity level of the order of a few per cent. Reproduced from [83].

2.3.4 Porosity

PEO coating usually contain relatively high levels of porosity, in the region of ~10-20%, covering a wide range of length scales [79, 83, 84]. Measurement techniques include dimensional measurements and weighing, mercury intrusion porosimetry, isothermal nitrogen adsorption (BET), hydrostatic weighing (for skeletal density), helium pycnometry (for surface-connected porosity), and X-ray tomography.

Skeletal densities are very close to theoretical densities, meaning the majority of porosity is surface-connected. The implication of this is that coatings are likely to be filled with electrolyte right down the substrate, in which case dielectric breakdown only need occur across the thin boundary layer (see §2.3.3) at the coating-substrate interface. This is consistent with the fact that the bulk-applied potential does not vary significantly during the process, although the growth rate is linear. Mercury intrusion porosimetry indicates a significant fraction of the porosity is nm scale, explaining why it was overlooked in early studies of PEO.

The presence of these levels of porosity is actually often very beneficial. This is clear for some applications, such as, bio-medical implants where osseointegration is desirable, and photocatalytic surfaces where a large specific surface area is important. Moreover, PEO is commonly used to create a good keying surface for further surface treatments, such as painting. Perhaps the most important, but least well recognised, benefit is the mechanical stability that results from the reduced stiffness of PEO coatings (compared to fully dense ceramic). This reduction is considerable, a typical change in Young's modulus compared with fully dense material being from ~400 GPa to something of the order of 30-50 GPa in the case of PEO alumina [73, 85], and is due to the porosity and micro-cracks in the coating. The strain tolerance of the PEO coatings is greatly enhanced because of the reduced stiffness, since the stresses that arise during deformation, or differential thermal expansion with the substrate, are reduced.

2.3.5 Phase composition and grain structure

The microstructure of PEO coatings is relatively complex. Local regions will have undergone very rapid solidification (quenched by the electrolyte after the most recent discharges), although regions in the immediate vicinity of those discharges may have effectively been heat-treated (raised to fairly high temperature and then allowed to cool). In general, however, several features are observed that are characteristic of rapid solidification. These include a very fine grain structure (possibly close to, or actually, amorphous) and the presence of metastable phases. It is worth noting that it is difficult to deliberately heat treat PEO coatings so as to modify these structures, since the range of temperature needed to effect significant change for such oxides would commonly be above, or at least close to, the melting temperature of the metallic substrate. Substrate composition, electrical parameters, electrolyte composition, and coating thickness all influence the final phases and elements present in a coating. Identification and quantitative proportions of phases present can be determined by X-ray diffraction (XRD) methods, while energy dispersive X-ray (EDX) analysis is commonly used to determine the elemental composition of coatings.

For Al, γ, η and ε phases of alumina are sometimes present, in addition to the stable α phase [86-88]. Anatase and rutile are usually both present in Ti PEO coatings [89, 90], and processing of the most common Ti alloy (Ti-6Al-4V) can generate significant quantities of the mixed oxide $Al_2O_3.TiO_2$ (aluminium titanate) [91, 92]. PEO coatings on Mg generally consist of a mixture of crystalline phases such as MgO, Mg_2SiO_4, Mg_2SiO_3 and Mg_3PO_4. For all substrates, some amorphous material is usually present. The proportions of phases present vary through the thickness of coatings, due to different thermal conditions, an example of the variation in phase proportions at different depths is shown in Figure 2.9.

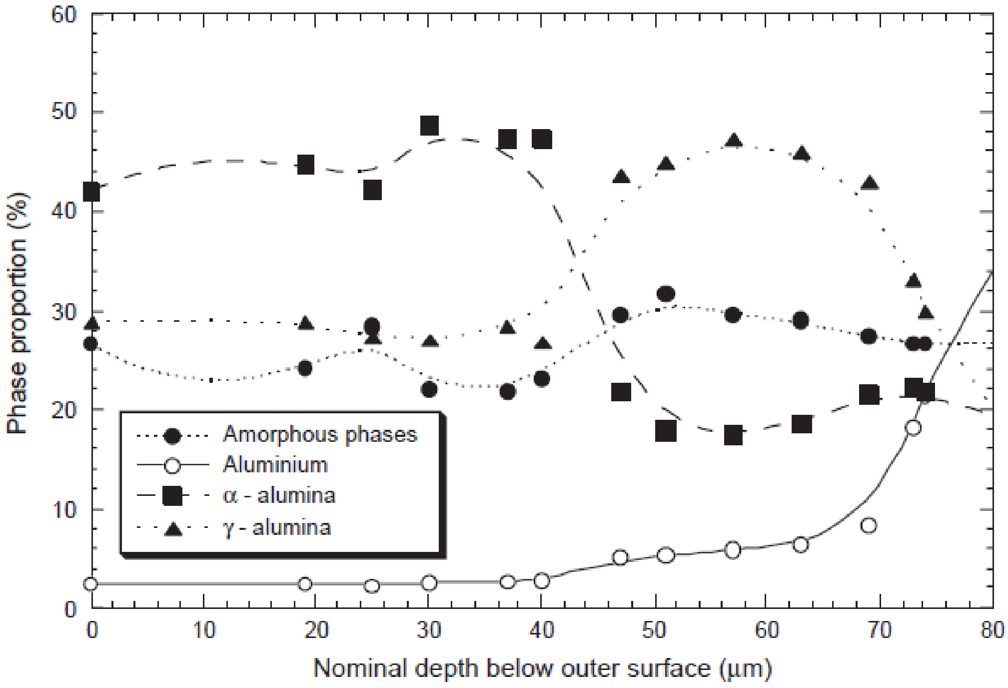

Figure 2.9 X-ray diffraction data in the form of a plot of the phase proportions against the nominal depth below the free surface for surface scans during the progressive grinding of a 100 μm thick coating, reproduced from [73].

As discussed in §2.2.2, species from the electrolyte may also be incorporated or deposited during coating production. Silicon from the electrolyte is often concentrated in the outer region of coatings [44, 75, 93, 94], while phosphorus is concentrated near the substrate-coating interface [94]. Monfort et al. [94] sequentially processed Al in a silicate based electrolyte for 30 minutes, followed by a phosphate-based electrolyte for just 15 s. EDX found phosphorous had reached the substrate-coating interface in this short time. Diffusional mass transport through the existing bulk oxide coating could not occur this quickly; therefore, the discharges facilitate “short circuit” mass transport between the electrolyte and substrate, allowing coating growth rates to remain approximately linear.

Chapter 3

Discharge Characteristics

Discharges clearly play a central role in the formation of PEO coating, and improvements in understanding discharge mechanisms is likely to lead to improvements in industrial practice. This chapter reviews the current literature relating to discharge characteristics during PEO, including the factors that affect the ability of a metal to undergo PEO, and recent efforts to characterise individual discharge events.

3.1 Factors affecting discharge formation

3.1.1 The "Valve Metals" and charge transfer

It is sometimes stated that PEO processing (and anodizing) are applicable only to the "valve metals" [95]. This terminology is not very well-defined, but the concept is usually taken to mean that electrical current can only flow in one direction in the metal-oxide-electrolyte system [96]. The understanding is that electrons can only flow through the oxide layer when the metal is cathodic (i.e. from the metal to electrolyte). In the anodic half of the cycle, it is assumed that electrons cannot flow through the oxide. The field across it builds up as the applied voltage is raised, and it may reach the breakdown potential (dielectric strength) for the oxide, at which point a discharge occurs. This rectification effect is presumed to arise at the metal/oxide junction, across which electron flow can occur only from metal to oxide.

In fact, there is not complete agreement about the set that constitutes the valve metals. A list such as Al, Mg, Ti, Ta, Nb, Zr and Be is commonly quoted, but it is quite certain that these could not have been identified from a knowledge of the rectification characteristics of the metal/metal oxide junctions concerned. Depending on their band gap (see §3.1.3 below), many oxides can be regarded as semiconductors and such rectification, known as a Schottky barrier, is exploited in various devices containing metal-semiconductor junctions. The sense of the rectification, whether electron flow can take place in the metal-to-semiconductor direction or in the reverse direction, is determined by the relative positions of the Fermi levels in the two constituents and hence by the nature and level of the doping in the semiconductor. However, this approach evidently cannot be used to identify or rationalize the set of valve metals. Most of the valve metal oxides actually have large band gaps (see §3.1.3 below) and so cannot really be treated as semiconductors—and certainly not as deliberately doped semiconductors. This increasingly outdated approach to classifying metals as being suitable for PEO (or for anodizing) is clearly flawed, although it is still quoted on occasion.

On the other hand, there is certainly asymmetry, in the sense that PEO discharges usually, but not invariably (see §3.4 below), occur only during the anodic part of the cycle. Furthermore, conventional anodizing (oxidation) only occurs when the metal is made the anode. However, a more plausible explanation for this is that it arises because of asymmetry in what is taking place within the electrolyte with the two different polarities and thus has at least some sensitivity to the electrolyte composition. This is illustrated in Figure 3.1, which gives a schematic depiction of the key steps during both anodizing[†] and PEO under anodic and cathodic polarity. For anodizing, oxidation is expected to take place only when the metal is the anode, since OH^- ions will then be

---

[†] Flow of ions through the oxide layer during anodization requires a very high field, and hence can only occur if it remains very thin (few nm). While it is common to depict this layer as if it has a significant thickness, it should be borne in mind that it must in fact be considerably thinner than the scale of the column structure.

transported through the electrolyte towards the interface, and this is a source of the necessary oxygen. In fact, it is usual for anodization to be carried out in acidic electrolytes (low OH^- concentration) and there may be some breakdown of water molecules to release oxygen.

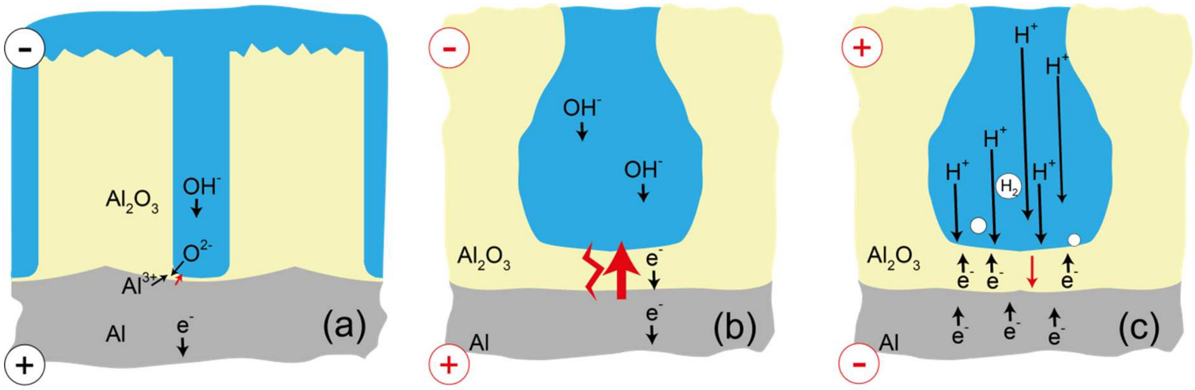

Figure 3.1 Schematic depictions of the transport phenomena taking place during (a) anodizing, (b) PEO with anodic polarity and (c) PEO with cathodic polarity.

During PEO, on the other hand, oxidation of the metal takes place as the plasma collapses and cools, so the key issue is whether the electric field across the residual oxide layer reaches the level necessary for dielectric breakdown. Under anodic polarization, flow of electrons through the oxide is limited by the relatively slow rate of arrival of the OH^- ions, which are moving through the electrolyte under the influence of the applied potential. This relatively slow rate of charge flow through the residual oxide layer ensures that the field across it reaches a level sufficient for discharge formation. Under cathodic polarization (Figure 3.1(c)), H^+ ions are attracted towards the oxide layer. These are much smaller and significantly more mobile than the OH^- ions, allowing a greater rate of flow of electrons through the oxide layer, with hydrogen gas being released at its top surface. The structure and dynamics of H^+ and OH^- ions in aqueous solutions are actually quite complicated, with various complexes being formed [97], but nevertheless the outcome is understood to be that H^+ ions do move significantly more quickly under the influence of an electric field.

Quantification of ionic motion in the electrolyte may be instructive and work on this is now starting [98]. This easier current flow in the cathodic half-cycle may limit the magnitude of the field across the oxide layer, reducing the likelihood of dielectric breakdown. Sensitivity might be expected to the rate at which hydrogen ions combine to form molecules on the oxide surface. There are certainly variations in this catalytic efficiency between different surfaces, for example Pt surfaces exhibit the highest activity for the hydrogen evolution reaction [99]. This issue is addressed in §3.3 below.

3.1.2 Thermodynamics of oxidation

Clearly, the magnitude of the free energy change associated with a metal being converted to its oxide is relevant to PEO. This change is negative at ambient temperature for all metals (except gold), so oxidation is energetically favourable in virtually all cases. However, as the plasma created during PEO collapses and cools, there may be competing oxidation reactions[†] for which the driving force is higher. Metal ions are present in the plasma as a result of volatilization from the substrate during a discharge. The plasma will contain hydrogen, due to the dissociation of water molecules at high temperature, so oxidation of metal ions is only expected to take place to a significant extent if it is energetically more favourable than oxidation of hydrogen to reform water.

Information of this type is provided by the Ellingham diagram for oxidation [100, 101]. Some such data are shown in Figure 3.2, covering most of the metals of potential interest for PEO (excluding rare metals and others of limited interest, such as those that react strongly with water and very high atomic number elements). This graph actually shows only the enthalpy change associated with oxidation, per mole of oxygen (i.e. the

---

[†] It should be recognized that this is not a purely thermodynamic issue. Oxide formation can only occur when the plasma temperature has become relatively low (perhaps <~3,000 K, depending on the metal and its concentration) and at this point it is being rapidly quenched, perhaps passing through the temperature range concerned in a time as short as ~10 μs. The kinetics of combination is therefore important. Of course, the presence of an excess of a competitor with a higher affinity for the oxygen, such as hydrogen in the case of some metals, will certainly slow down the kinetics of formation of the metal oxide and may inhibit it completely.

free energy change at 0 K). However, this is sufficient for approximate ranking purposes, since the rate of decrease of the magnitude of this energy change with increasing temperature is similar in most cases. This reflects the fact that the change in entropy is similar in each case, mainly due to a reduction in the number of moles of gas as the oxygen is consumed. It can be seen that, for metals with low energy changes (Cu, Ni, Fe, Sn, Mo and W), the driving force for oxidation is similar to, or lower than, that of hydrogen being converted to water. These metals are therefore unlikely to oxidize as a PEO plasma collapses and cools, particularly since the hydrogen concentration there is likely to be relatively high. It is worth noting there are some very common types of metal (copper alloys, steels, and Ni-based superalloys) that are expected to be unsuitable for PEO processing, and this is generally found to be the case experimentally. There have been reports [102, 103] of successful PEO processing to produce coatings on steels, but in such cases it is probable that much of the oxide formation took place via deposition from the electrolyte, leading to friable and poorly-bonded coatings. There is then a second group of metals (including Cr, Nb, Ta and V) for which the oxidation energy is higher than for hydrogen, although not dramatically so. Finally, there is a third group (including Ti, Al, Mg, Be, Hf, Zr, Y and Sc) with very high values, such that there will clearly be a very strong thermodynamic driving force for oxidation.

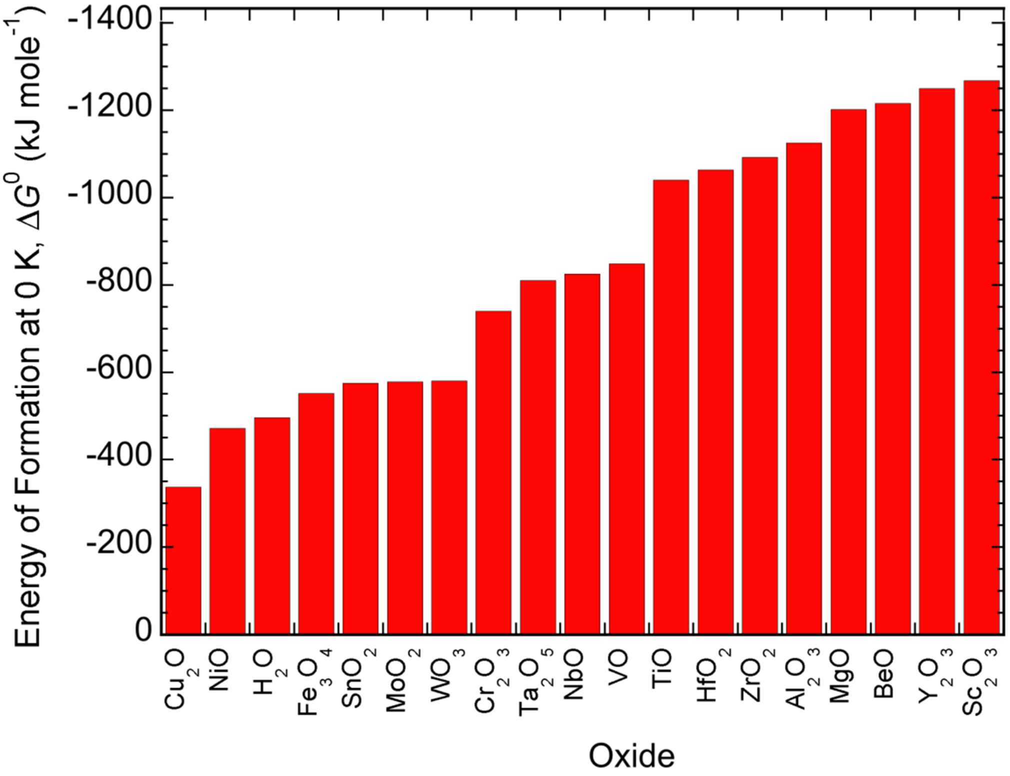

Figure 3.2 Free energy values [100, 101] for formation of various oxides from the metal, and of water from hydrogen, at 0 K. These energies are all expressed per mole of oxygen. For metals that can form more than one oxide, the data refer to the one for which the largest amount of energy is released.

This is a crude classification, and it must be borne in mind that the active oxidizing agent in a PEO plasma as it cools is unlikely to be molecular oxygen and the temperature at which oxidation takes place is unknown, but will be relatively high. Additionally, the concentration of metal ions in the plasma is also unknown, but will be relatively low. Data for the free energy changes under these conditions are simply not available. It should also be emphasized again that oxidation is not favoured for any metal at the temperatures typical of these plasmas [104] and it is only towards the end of their collapse and cooling that combination with oxygen can occur. Nevertheless, it is relevant to observe that this last group contains the three metals (Al, Mg and Ti) that are most commonly, and successfully, subjected to PEO treatment. It might be noted that there is a common perception that Ti is not as easy to PEO process as the other two. In addition, the oxide formed is invariably TiO_2, despite the fact that, according to the thermodynamic data, TiO is more stable (although there is some uncertainty about this issue, and more than one phase [105] with the approximate stoichiometry of TiO). Of the others in this group, there have been several reports [106-108] that Zr can be PEO processed. There appear to be no reports about PEO of Hf, Sc or Y, and very few [109] concerning Be, although it is sometimes included [110] in listings of metals that are suitable.

As mentioned above, it is clear that metals such as Ni, Fe, Cu, Sn, Mo and W cannot normally be processed by PEO. However, it may be possible with heavily alloyed versions, such as NiTi shape memory alloy [111]. Also, the PEO conditions may have an influence and it has been shown [112] that Mo can be processed in an electrolyte of borax, water and ethylene glycol under cathodic polarisation. However, the metals put here into the central group (Cr, Nb, Ta and V) are of interest. Information about PEO of them is limited, although there have been reports of successful processing for both Nb [113-118] and Ta [119, 120]. From a thermodynamic point of view, growth of the oxides of these metals should be possible, perhaps depending on their concentration, and that of hydrogen, in the plasma. This is certainly true for Ti, despite the perception that it is less suitable than Al and Mg for PEO treatment. It therefore seems clear that there must be other factors affecting the ease of PEO processing.

3.1.3 The oxide band gap

The oxides of most of the so-called “valve metals” have large band gaps. Broadly speaking, such band gaps (i.e. highly insulating oxides) might be expected to be associated with the oxide structure being highly stable thermodynamically, although there is not a clear mechanistic link. Nevertheless, there is a correlation, evident from the data [121] plotted in Figure 3.3, although it can be seen that it is not a close or well-defined one. For example, the thermodynamic driving force for oxidation of Ti is similar to those of Al and Mg, but its oxide has a band gap with less than half the magnitude of those oxides.

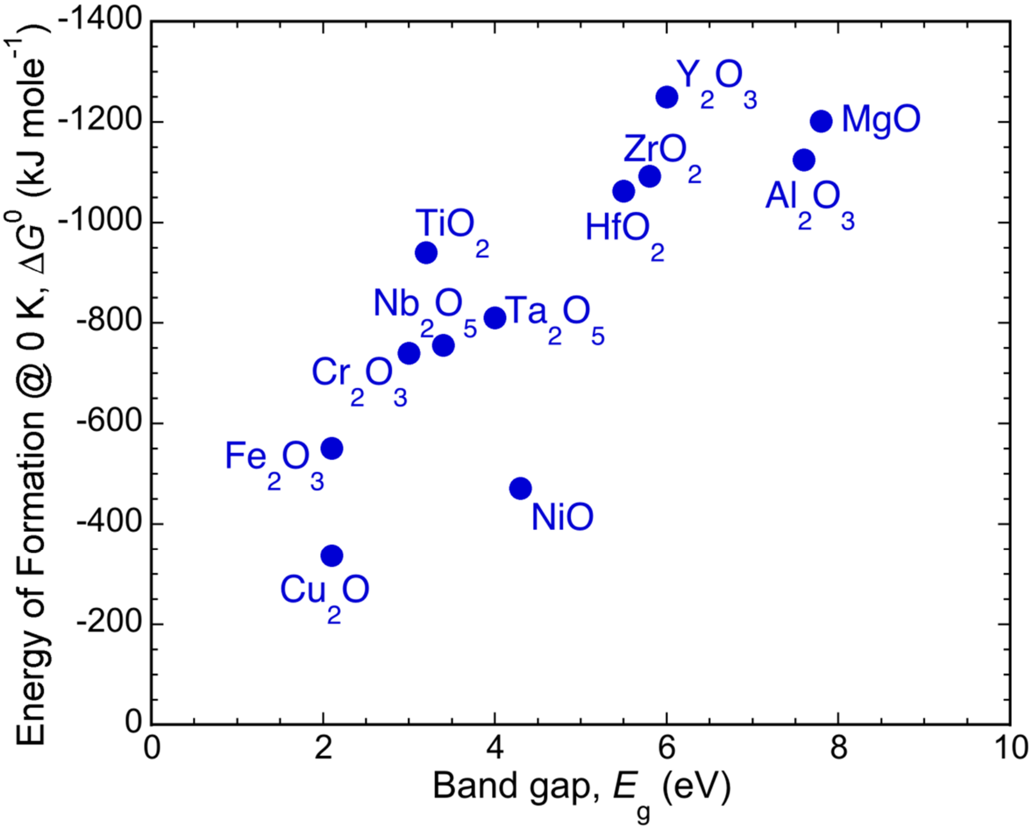

Figure 3.3 Plot of the free energy of formation of selected oxides against their band gap [121].

It is important to be clear about the relevance of the band gap to PEO processing. One issue is whether the oxide can acquire a relatively high electrical conductivity, either through doping or via thermal excitation of electrons across the band gap. The latter possibility can largely be ignored, since these layers remain at ambient temperature up to the point of dielectric breakdown and their band gaps are all very high compared with thermal energies. Extrinsic (doped) semiconducting behaviour can also be largely neglected, since any such doping would be accidental and variable.

However, the issue of whether and how electrons can move through the oxide, and the relationship between this and the onset of dielectric breakdown, clearly is important for PEO and the band gap is significant in this respect. One possible mode of passage is electron tunnelling [122]. This is essentially a quantum effect and it is usually taken to be possible only through very thin layers, perhaps a few nm. It allows electrical contact to be established readily between nominally bare metal wires, even though they do in fact have thin surface oxide layers in the vast majority of cases.

The oxide layer thickness is clearly important and, while PEO coatings are often very thick (tens or hundreds of μm), it is now well established that residual oxide layers on the substrate remain much thinner throughout the process. This happens because PEO coatings are quite highly porous, particularly in the vicinity of an active discharge site, with the pores almost certainly being full of electrolyte before a discharge occurs (see §2.3.4), this is depicted in Figure 3.1(b) and (c). This explains the lack of any strong dependence on coating thickness of the voltage needed for PEO processing. While unequivocal evidence for this is lacking, there is a general consensus that dielectric breakdown commonly occurs during PEO across a residual oxide layer on the substrate that has a thickness of the order of 1 μm. While this is "thin" for many purposes, it is too thick for electron tunnelling.

However, this does not mean that electrons cannot move through these oxides, and it is well established that electron mobility can be relatively high in some oxides, particularly those with variable stoichiometry and high levels of various defects. Considered in terms of a band gap, such defects may provide energy levels within the gap, which assist motion of electrons through the material. A general correlation is still expected between a high band gap and a low electron mobility and, on this basis, the metals for which PEO can be carried out most readily are likely to have relatively large band gaps. The key point here is that, if electrons do travel through the oxide layer, this will not lead to any oxidation of the substrate, and they may carry much of the imposed current. In such cases, the PEO process (i.e. plasma generation and oxide formation as the plasma collapses and cools) may be reduced or eliminated, even though there may be a strong thermodynamic driving force for metal oxidation. The voltage during the anodic half-cycle is expected to be lower than for cases in which most of the current is being carried by the discharges. Some support for this general idea is provided by the work of Munoz and Bessone [123]. They showed that, during anodization of Al, the introduction of small Ni and Co particles into the growing oxide layer, via cathodic deposition, raised the conductivity of the layer, and hence reduced the electric field across it and the rate of alumina growth.

3.1.4 Dielectric strengths and dielectric constants of oxides

The band gap gives at least an indication of probable electron conductivity, and hence influences the electric field that builds up across the oxide. A dielectric strength is normally expressed as a breakdown field (in V m^{-1}), which is measured experimentally. The outcomes of such experiments tend to be variable, depending on factors such as the purity and porosity levels. For "good" insulators, values which are above that of dry air (usually quoted as ~3 MV m^{-1}) are usually obtained. Values for alumina and magnesia, for example, are usually in the range 10–30 MV m^{-1}. Measurements have been made for other oxides, often giving values in a lower range for oxides with smaller band gaps, but it is difficult to regard these as highly accurate or reliable. Therefore, it is probably better to use band gap values as an indication of likely dielectric strength to avoid these inconsistencies.

There is, however, another electrical property that is potentially significant, which is the dielectric constant (relative permittivity). This is a dimensionless number that gives an indication of the capacity of the lattice to store electric charge. It depends on the nature of the bonding (how strongly ionic it is) and on the arrangement of the ions. For example, non-centrosymmetric structures can have very large dielectric constants. The exact significance of this for PEO is not clear, but the capacity of the oxide to store charge may affect the electric fields being created during the process (under AC conditions). There is no obvious reason why its value should correlate with either the band gap or the thermodynamic stability and indeed the plot shown in Figure 3.4 suggests that there is no clear correlation. It may be noteworthy that TiO_2 has a very high dielectric constant—note the log scale in this plot.

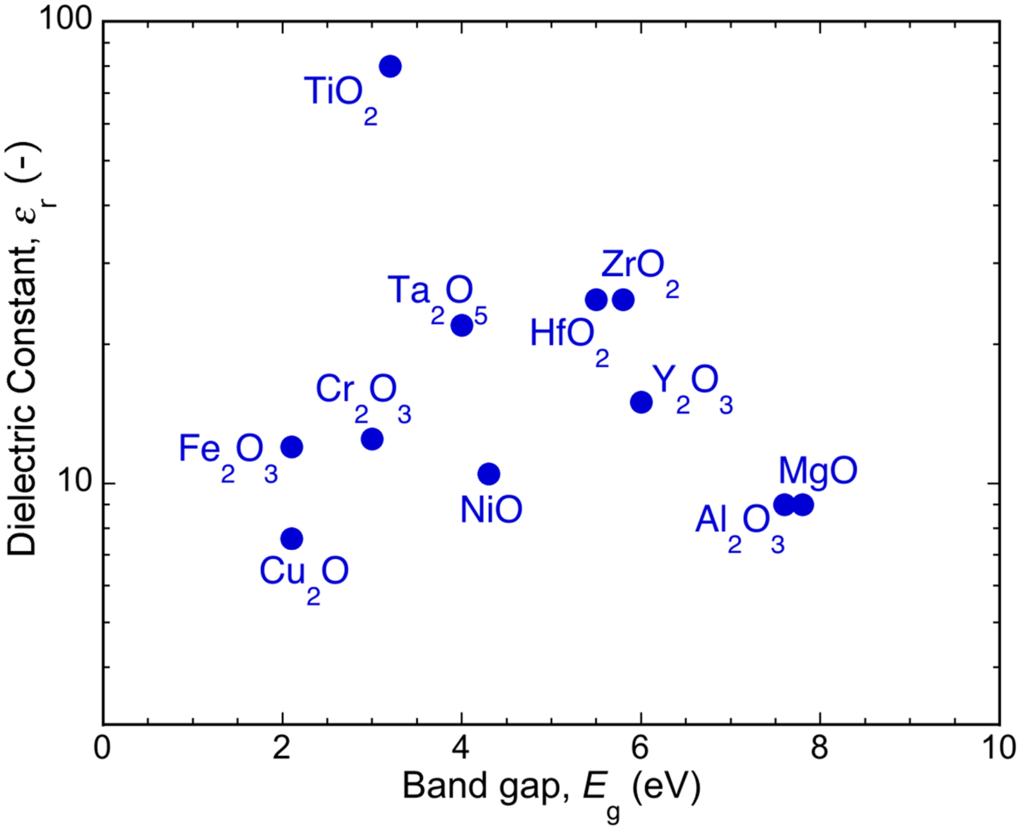

Figure 3.4 Plot of the dielectric constant of selected oxides against their band gap [124].

3.2 Individual discharge parameters

Through-thickness electrical discharges are fundamental to the PEO process. Discharges are thought to provide a mechanism for exposing the metallic substrate to a source of oxygen from the electrolyte. The nature of these discharges, and their distributions in time and position, are thus central to understanding of, and control over, the PEO process. Significant efforts have been made in this direction in recent years, with a number of techniques being used to assess individual discharge characteristics. These include electrical monitoring, optical imaging, and optical emission spectroscopy (OES).

Electrical monitoring, such as that shown previously in Figure 2.3, usually represents the aggregation of many hundreds, or thousands, of individual discharge events.

However, single discharge experiments can be performed by processing a small area sample, since this reduces the probability of having more than one discharge active at a given time. Parallel processing with a conventional bulk sample, where many discharges are taking place throughout, ensures that the PEO process is proceeding as normal. An oscilloscope can be used to measure the current flowing, giving information on the discharge lifetime and current profile, along with the applied voltage and bulk current. There may be some uncertainties about the exact similarity of conditions between small area and conventional conditions, for example, the electric field is probably more divergent for the small area sample, there may be an uncertainty about its exact surface area and in some cases more than one discharge (cascade) could be taking place on it at the same time. Nevertheless, the technique is clearly capable of revealing important information that is relevant to conditions during conventional processing of bulk samples.

Optical imaging of a specimen undergoing PEO is an obvious starting point for obtaining information on individual discharges. In principle, optical imaging can provide information on discharge duration, spatial distribution, size, and intensity. However, these all require sufficient resolution in time and space to obtain reliable information. Imaging has been employed by a number of authors to determine such characteristics, but systems often lack the required resolution to provide accurate data. Advances in camera technology have allowed improvements to be made in this area, and such systems have formed the basis of some more recent studies.

OES can provide information on the elements present and temperatures that exist within the electrolytic plasmas formed during PEO. There are many methods used to determine the electron density and temperature, which can give a very large range of values. The determination of species present is more straightforward, but still relies on sufficient resolution of the spectrometer and some peaks may overlap.

3.2.1 Discharge lifetimes

Typical discharges are now known [43, 47, 74, 77, 125-127] to occur in prolonged sequences (“cascades”) at particular locations, and to have lifetimes of the order of a few tens to a few hundreds of μs, with “incubation” periods between them of around a few hundred μs to a ms or two. The lifetime of a cascade can apparently be very long (perhaps of the order of a second or more [128]), although during AC processing the discharges normally form only during the anodic part of the cycle. This limits the duration of a continuous sequence to something less than the half-cycle period (i.e. to several ms for a 50 Hz supply), when the voltage is above the breakdown potential.

Optical imaging and electrical monitoring are commonly used to investigate the duration of such discharges during PEO. Electrical measurements of individual discharges were first made by Van et al. [129], using a needle head of 17.8 μm diameter. Kasalica et al. [130] recorded a similar event, relating to the end stages of anodizing aluminium in an acidic electrolyte. The exact monitoring set-up is poorly reported, but the duration of the discharge event is ~1 μs. This is significantly shorter than many other reported discharge durations, but may represent discharges in the initial stages of PEO.

Two methodologies of electrical monitoring were developed by Dunleavy et al. [47, 74, 77] to quantify discharge lifetimes, along with other parameters. The first technique used pre-processed “conventional” PEO coatings on aluminium, referred to as Low Power Direct Current Testing (LPDCT). A limited power supply only initiates one discharge at a time, allowing the current profiles of individual discharges to be resolved. The second technique involved monitoring the current through a small area sample (typically the end of a 500 μm–1 mm diameter wire), processed in an industrial power supply. This technique is referred to as Full Power Alternating Current testing (FPAC testing). The two methodologies showed good agreement with median discharge durations of ~52 μs and ~42 μs for LPDCT and FPAC testing respectively, see Figure 3.5. FPAC testing showed a larger proportion of short events, which was attributed to competition between discharges for the available current. There is a clear trend for discharge durations to increase over the course of 40 minutes of PEO processing. Figure 3.6 shows the distribution of event durations with processing time. The fraction of short events remains approximately constant over the entire period but the median and maximum event durations increase significantly.

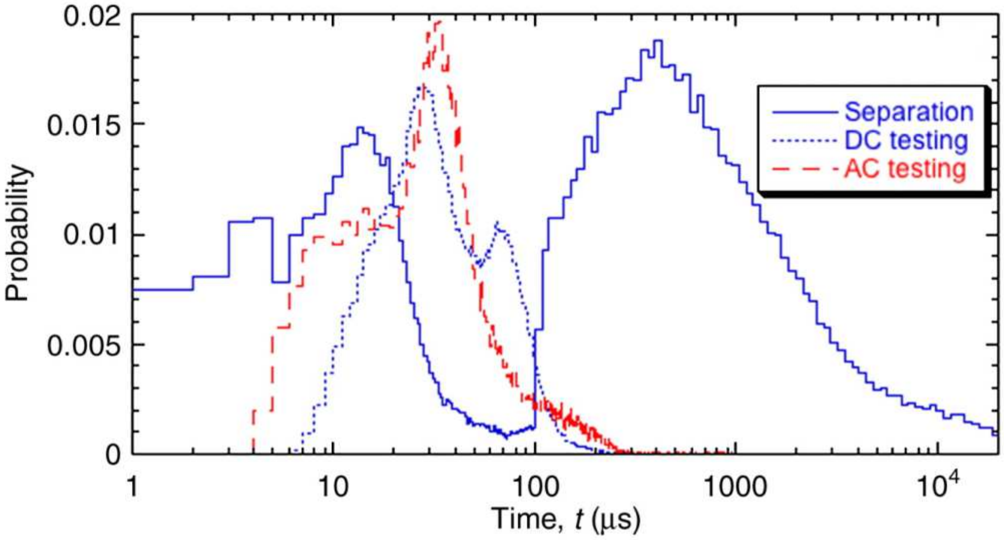

Figure 3.5 Histogram showing statistical characteristics of current pulses obtained during LPDCT, showing duration (and temporal separation) with FPAC data for comparison. Reproduced from [47].

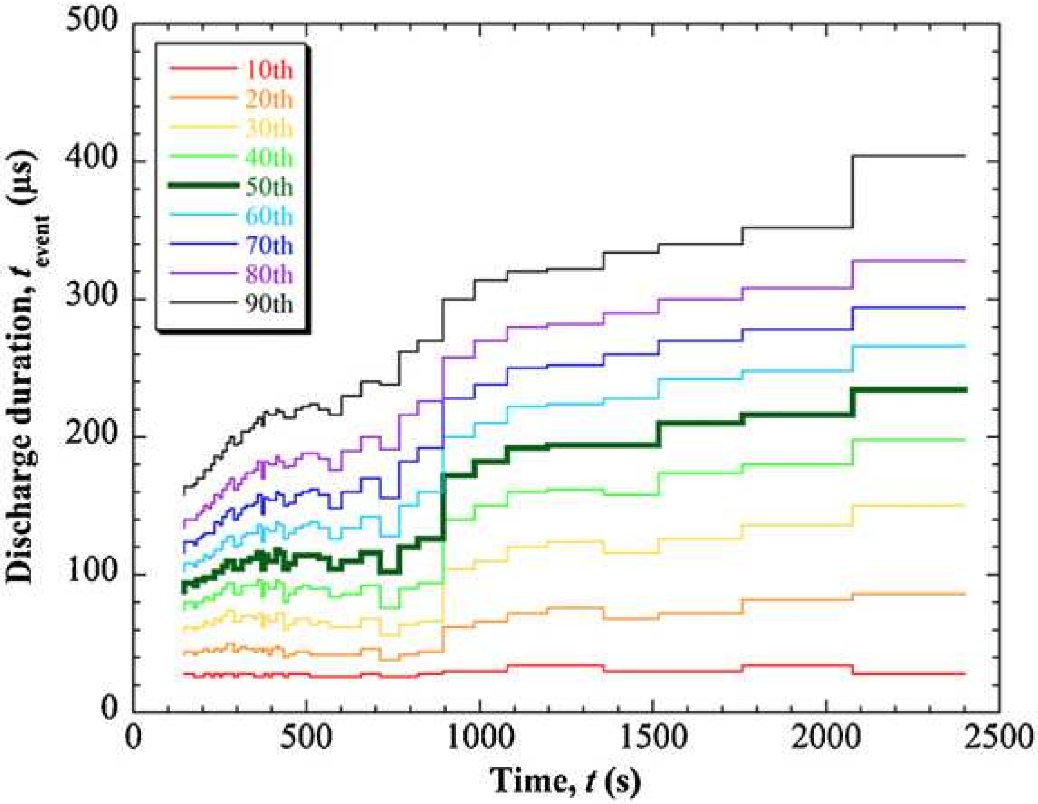

Figure 3.6 Plots of every tenth percentile of discharge parameter distributions as a function of processing duration for discharge duration. Reproduced from [74].

Optical imaging has also been employed extensively to obtain information on discharge durations. For discharge lifetimes from image sequences, the exposure time must be significantly shorter than the duration of a discharge, which is often not the case. It can be seen in Figure 3.7 [47] that electrical signals are very well correlated with light emission intensity (captured using a photomultiplier tube), confirming that optical characterisation is a suitable method for detecting discharges, provided suitable time resolution is used. The values reported from optical measurements tend to be significantly larger than for those obtained from electrical monitoring. This is due to the limitations of the imaging systems used. For example, Matykina et al. [131] studied DC processing of titanium using an exposure time of 10 ms, giving the apparent discharge lifetime of 100–800 ms. These results are unlikely to represent individual discharges, but rather a series of shorter discharges occurring at, or very near to, the same location on the sample surface.

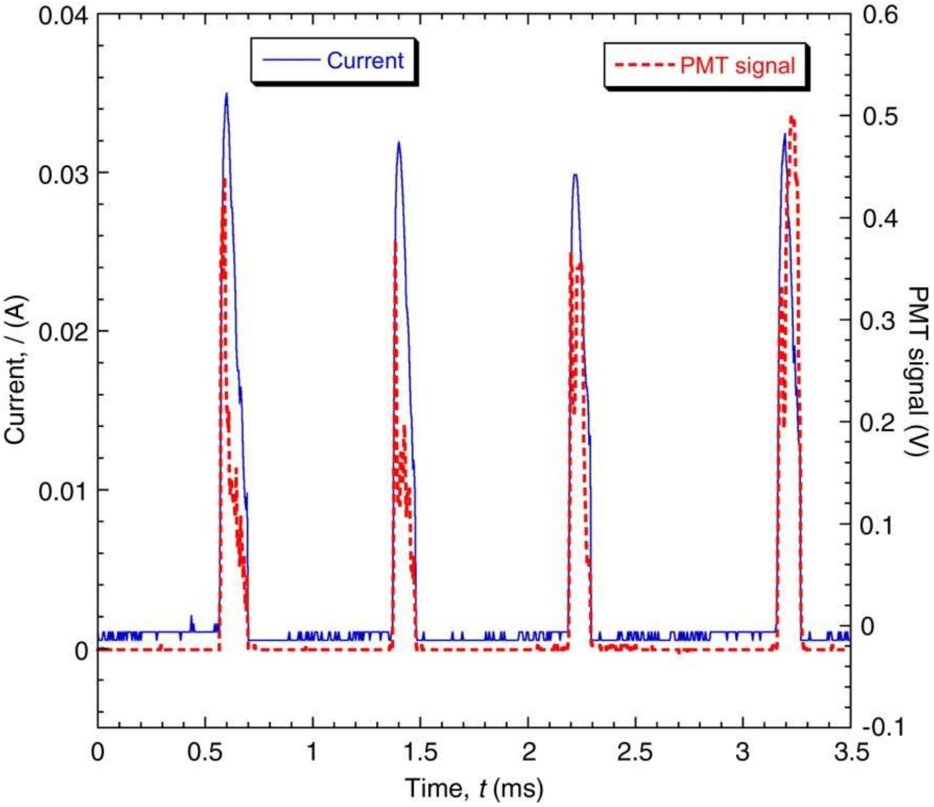

Figure 3.7 Typical data for a sequence of current pulses, and for the associated light emission, obtained from a photomultiplier tube. Reproduced from [47].

Yerokhin et al. [132] used imaging at 24 Hz, of 50 Hz AC PEO processing of aluminium, to obtain the spatial distribution of discharges and the apparent area undergoing discharge. Discharge current densities were inferred and discharge lifetimes estimated from the time required for local melting of the alumina coating. This method involves several crude approximations and does not consider the possibility of discharges reoccurring at the same location. Exposure times are not quoted. However, at such a low frame rate it is very likely that frames represent an aggregation of events, rather than the discharges active at a given moment in time.

More appropriate exposure times have been used by Arrabal et al. [80], who studied magnesium using an exposure time of 50 μs or 185 μs and found discharge lifetimes to range from 50 μs to 4 ms (although the lower bound of 50 μs is recognised as a limitation of the imaging system). Martin et al. [43] studied aluminium PEO using an exposure time of 8 μs, finding discharge durations ranged from 8 μs to around 400 μs. Increasing the applied current density caused discharge lifetimes to increase, and higher pulse frequencies caused the average discharge lifetime to decrease. These results are in much closer agreement with durations obtained from electrical monitoring, highlighting the importance of using appropriate imaging systems. Habazak et al. [133] performed high-speed video imaging of titanium PEO at 100 Hz and noted that discharges are extinguished during the cathodic half-cycle, but can re-ignite at the same location in the subsequent anodic half-cycle. However, the nature of discharges within a single anodic half-cycle was not examined. Table 1 gives a summary of reported discharge lifetimes.

Substrate	Measurement technique	Duration / μs	Reference
Stainless steel	Electrical monitoring	~ 170	Van et al. (1977) [129]
Aluminium	Electrical monitoring	~ 1	Kasalica et al. (2009) [130]
		10–100	Dunleavy et al. (2009) [47]
		10–160	Dunleavy et al. (2011) [77]
		10–400	Dunleavy et al. (2013) [74]
Aluminium	Inferred from optical imaging	250–3,500	Yerokhin et al. (2003) [132]
	Optical imaging	8–400	Martin et al. (2013) [43]
Titanium	Optical imaging	35,000–800,000	Matykina et al. (2007) [131]
		10–5,000	Habazak et al. (2012) [133]
Magnesium	Optical imaging	50–4,000	Arrabal et al. (2009) [80]

Table 1 Summary of reported discharge lifetimes.

3.2.2 *Discharge current*

It is of interest to understand how a single discharge is terminated. Some insights into this can be obtained by studying the details of how the current associated with a discharge changes with time. The discharge current profile can be monitored using the techniques described for electrical monitoring of discharge lifetimes in §3.2.1. These are typically several tens of mA, but it is important to appreciate that these characteristics are not uniform. They vary significantly with coating thickness, and with the details of the evolving microstructure at the location concerned. Nevertheless, allowing for stochastic variations, some clear features can be identified. Some such features are illustrated by the plots [77] in Figure 3.8(a) and (b), which shows data obtained by statistical analysis of a large number (millions) of individual discharges, relating in this case to two different coating thicknesses. Mean current profiles, *I(t)*, were calculated from events with the same initiation voltage, V_{init}, and discharge lifetime, t_{event}. Thicker coatings lead to discharges that require a slightly V_{init}, have longer lifetimes, and carry higher peak currents, I_{peak}. They are clearly more energetic, but more dispersed in time and location, assuming that the overall average current, and coating growth rate, remain much the same. This is usually the case, and it is a commonplace observation that discharges tend to evolve in this way as the coating thickens. *I(t)* can been seen to scale with V_{init}, with no appreciable difference in shape. This suggests that all PEO discharge events develop according to the same physical mechanism.

Figure 3.8(c) shows how t_{event} varies for a given I_{peak} value. The profiles are all very similar up to the point where the current is shut off. This suggests there is a process that pinches off the current flow over a short period and that there is a rapid rise in the resistance of the discharge site. Furthermore, a correlation is seen between I_{peak} and t_{event}, however, thinner coatings tended to have a slightly larger t_{event} for a given I_{peak}, as can be seen in Figure 3.8(d).

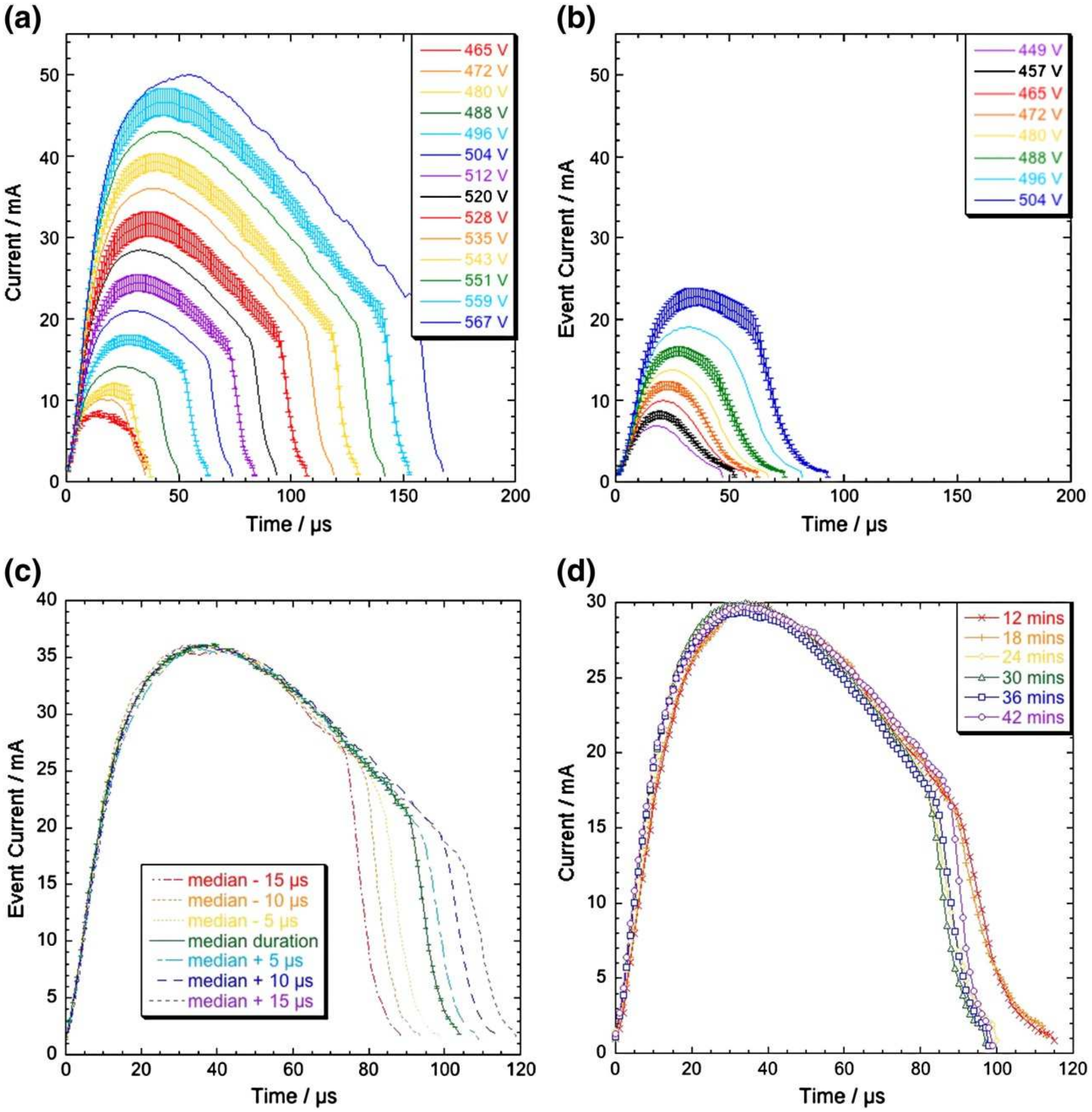

Figure 3.8 Plots of averaged current–time relationships for (a) a 42-minute and (b) a 6-minute coating, sorted by V_{init}, for events having the median lifetime t_{event}. Error bars have been omitted for half of the voltages concerned, to avoid crowding of the data. Also shown are (c) average *I(t)* profiles, sorted by I_{peak} value, with the central profile corresponding to the median t_{event} value and the others to events with lifetimes 5, 10 and 15 µs shorter and longer than this, and (d) mean *I(t)* profiles sorted by I_{peak}, for coatings between 12 and 42 min. All profiles correspond to the median t_{event} at the relevant I_{peak} value. Reproduced from [77].

3.2.3 Plasma temperature and composition

Optical emission spectroscopy (OES) is often used to estimate the electron temperature, and determine the composition of the plasmas created by electrical discharges during PEO. Generally, the relative intensity of atomic or ionic emission lines, or the broadening of certain lines, is used to determine the electron temperature of the plasma. This information is helpful when considering the mechanisms involved in formation of coating material during PEO. The application of OES in characterising PEO discharges is complicated by the stochastic nature of discharges, and spectra represent an integration of many thousands of events.

The first spectral analysis of plasmas relating to the PEO process was performed by Klapkiv et al. [134] on aluminium. Elements from both the electrolyte and the working electrode (i.e. the aluminium substrate) were found in the plasma, and electron temperatures were estimated to be in the range 3,660–12,950 K. These results are in broad agreement with Dunleavy et al. [47], who estimated electron temperatures of ~3,500 K and 16,000 ± 3,500 K, and observed strong emission lines relating to atomic O, Na and K (from the electrolyte) and Al (from the substrate), as well as hydrogen α and β Balmer lines. These authors attribute the difference in electron temperatures to a high density hot core, surrounded by a less dense, cooler, periphery extending into the electrolyte [47, 135]. In a later study, Klapkiv determined the discharge channel to be filled with an equilibrium non-degenerate, quasi-ideal plasma, with the electron and gas temperatures close to each other for the range of electron densities identified (i.e. the system was in Local Thermal Equilibrium, LTE) [136]. However, there is some debate regarding whether the PEO plasma can be considered to be in LTE or Partial LTE [137].

Hussein et al. [138] also found electron temperatures to be 4,500 ± 450–10,000 ± 1,000 K for aluminium processing, but attribute the difference to a very different effect. An alternative discharge model is proposed with three populations of discharges, “small” and “mild” discharges relating to the low temperature and “strong” discharges relating to the high temperature. Three electron densities for PEO on aluminium were found by Jovović et al. [137], who support the model proposed by Hussein et al., and electron temperatures of ~38,300 K and ~3,300 K were calculated from relative line intensities. Jovović et al. [139] found magnesium substrates show similar electron temperatures and three populations of electron densities. In this model, it is proposed that some discharges initiate at an intermediate height within the coating and extend into the electrolyte. However, no mechanism for charge conduction between the substrate and initiation site of the discharge is suggested. Therefore, this model seems unrealistic and does not correlate to other types of experimental evidence. As discussed in §3.2.2 the current profiles of individual events scales proportionally with the event initiation voltage over a continuous range. It therefore seems unlikely that there are distinct populations of discharges, as one would expect each "type" of discharge to have its own characteristic current profile. Another possibility for the different electron temperatures is a temporal variation. Since spectra are integrated over many hundreds or thousands of events, any variations within the lifetime of a discharge cannot be determined.

Spectral studies from substrates other than aluminium are less common. There is limited evidence that the plasmas produced during titanium and tantalum PEO do not contain substrate material (i.e. no emission lines relating to titanium or tantalum) when processed in 12-tungtosilicate acid [49, 140]. Stojadinović et al. propose the reason for this to be the higher melting temperature of titanium and tantalum, compared with aluminium. This seems unlikely due to the high electron temperatures and LTE conditions, and is likely to be the result of the experimental set-up. In both studies, two populations of electron densities are estimated by fitting two Lorentzian profiles to the H_β line profile. Again, this was attributed to different types of discharge, rather than different regions within the plasma. However, Hussein et al. [125] found the OES signal did contain emission lines from titanium during PEO processing of Ti-6Al-4V, as did Stojadinović et al. in a later study when processing in an alkaline silicate electrolyte [141].

3.2.4 Discharge plasma size

Discharge diameters may be estimated via optical imaging. Authors have reported apparent areas, radii, and diameters, so values summarised in Table 2 have been converted to radii, assuming circular cross section, for comparison. In most cases relatively long exposure times were used (ms rather than μs), so data probably represent the maximum size reached, but do not give information on the dynamics of the plasmas bubbles. It should be noted that the values obtained correspond to the area from which light is apparently emitted and will therefore be larger than the plasma itself. Studies do not have sufficient spatial resolution to determine whether any internal plasma structure exists. Reported values of discharge radii are in reasonable agreement (in the range of tens to hundreds of μm) and do not show much variation with substrate material, suggesting that the plasmas created on different materials probably have similar pressure and temperature ranges. Additionally, the size of discharges tends to increase with processing time (i.e. with coating thickness), and tend to increase in size with the applied potential, which is illustrated in Figure 3.9 [49, 140, 142, 143].

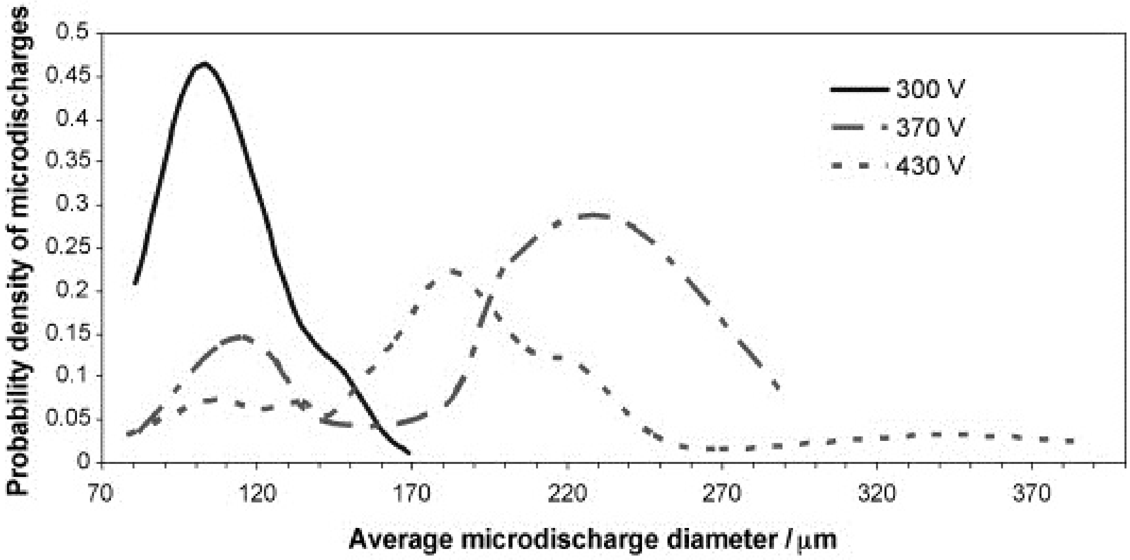

Figure 3.9 Microdischarge diameter distribution for PEO treatment of titanium [131].

A more recent study by Martin et al. [43] used more appropriate exposure times of 8 µs. However, linear spatial resolution was ~130 µm, which is of the order of the discharge sizes reported elsewhere. Some trends were observed with the applied electrical parameters. Discharge sizes were larger at lower applied frequency and higher current densities. These results must be treated with caution, given the limited spatial resolution.

Substrate	**Equivalent radius range / µm**	**Reference**
Aluminium	60–660	[132, 142]
	400–890	[43]
Titanium	35–190	[131]
	90–440	[49]
Zircaloy-2	35–500	[143]
Tantalum	90–300	[140]

Table 2 Summary of reported values for the size of plasma discharges during PEO of various substrate materials.

Dunleavy et al. [77] took a theoretical approach to estimate the discharge plasma radius based on electrical data. A highly simplified model was adopted, in which the plasma resistivity was zero, and the plasma geometry was a perfect hemisphere on a flat coating. This allowed the plasma radius to be estimated for various peak discharge currents (which have been obtained by varying the capacitance of the power supply system), using equation (1), with the results shown in Figure 3.10. These predictions are slightly lower than those estimated by optical techniques, and represent an underestimate since the plasma will not have zero resistivity. However, as mentioned previously, optical imaging is likely to overestimate the discharge plasma size.

$$R = \frac{\rho}{2\pi r_P} \tag{1}$$

Where ρ is the electrolyte resistivity and r_P is the plasma bubble radius.

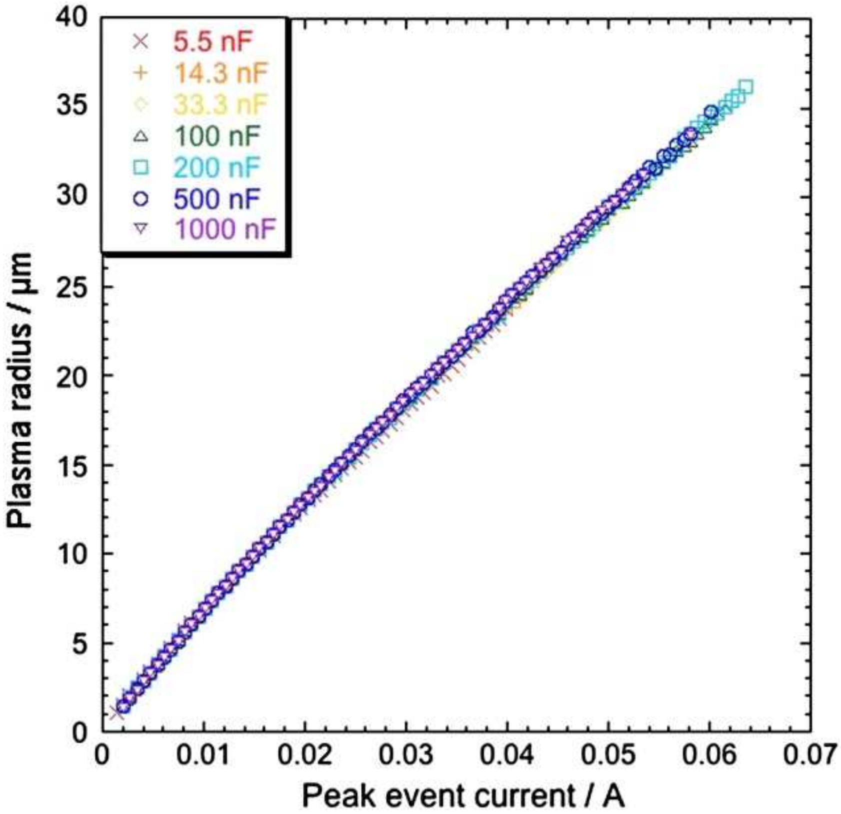

Figure 3.10 Predicted radius of the plasma bubble, r_P, at the point of peak current, as a function of the discharge peak current, I_{peak}. Different I_{peak} (and corresponding voltage values) are obtained by varying the capacitance of the power supply system. Reproduced from [77].

3.2.5 Energetics of individual discharges

As discussed in §3.1.2 oxidation of metals is a thermodynamically favourable process, so should release energy rather than consume it. However, PEO processing does in fact consume relatively large quantities of electrical energy. There have been a number of estimates of the macroscopic energy consumption rates [44, 144, 145], with values between 10 and 80 MJ m^{-2} μm^{-1} depending on the exact experimental set-up. Various phenomena taking place during PEO are causing energy to be consumed, such as, melting and vaporization of substrate, melting of existing oxide coating, initiation and sustaining of the plasma, vaporization of water, and electrical heating of the electrolyte. Further study of such phenomena is required if reductions in the energy consumption of PEO processing are to be made.

There have been a number of estimates of the energy dissipated by individual discharges during PEO processing [47, 126, 127, 129, 130]. Values range from a few μJ up to several mJ, although, a value of ~1 mJ is a sensible estimate from typical discharge parameters (500 V × 40 mA × 50 μs).

3.3 Gas evolution

PEO is normally carried out using an AC supply, with the electrical circuitry often set such that the current is fixed and is the same in both anodic and cathodic parts of the cycle. For metals that are well suited to PEO processing, at least most of the current flowing in the anodic part of the cycle is carried in the form of discharges (that stimulate oxidation of the substrate). These discharges are initiated by flow of electrons from the electrolyte to the substrate, through the residual oxide layer, in an electron avalanche process that leads to plasma formation. Hydroxyl anions could lose electrons to form oxygen gas (as in conventional electrolysis of water), but during successful PEO processing this is likely to be interrupted by the plasma formation. It seems likely that these ions, and possibly oxygen molecules that have just been formed, will become incorporated into the plasma. Of course, they will not be the only source of oxygen in the plasma, since water molecules will also enter and become ionized. Some of this oxygen is then likely to combine with metal cations in the plasma as it cools down during its collapse, particularly if the thermodynamic driving force for this is greater than for the re-formation of water.

If PEO is proceeding successfully, with most of the current flowing via plasma discharges, then there should be little or no evolution of oxygen gas during the anodic half-cycle. It is perhaps worth mentioning in this context that there has been relatively little direct experimental investigation of the rates or types of gas evolution during PEO, with some of the published results appearing contradictory. Nevertheless, there has been some systematic work and a consistent finding is gas evolution rates are considerably above the Faraday yield [146-150], corresponding to conventional electrolysis of water. This has also been reported for contact glow discharge electrolysis [151, 152].

Figure 3.11 shows an example plot [147] of the voltage and the quantity of gas evolved (at the anode) during a typical DC PEO run, with it being reported in this case that virtually all of the gas was oxygen. However, another report [148] suggest that hydrogen can also be formed at the anode in significant quantities. This work, which is shown in Figure 3.12, related to several modes of operation (DC anodic, Unipolar anodic, and Bipolar), with different current densities and frequencies.

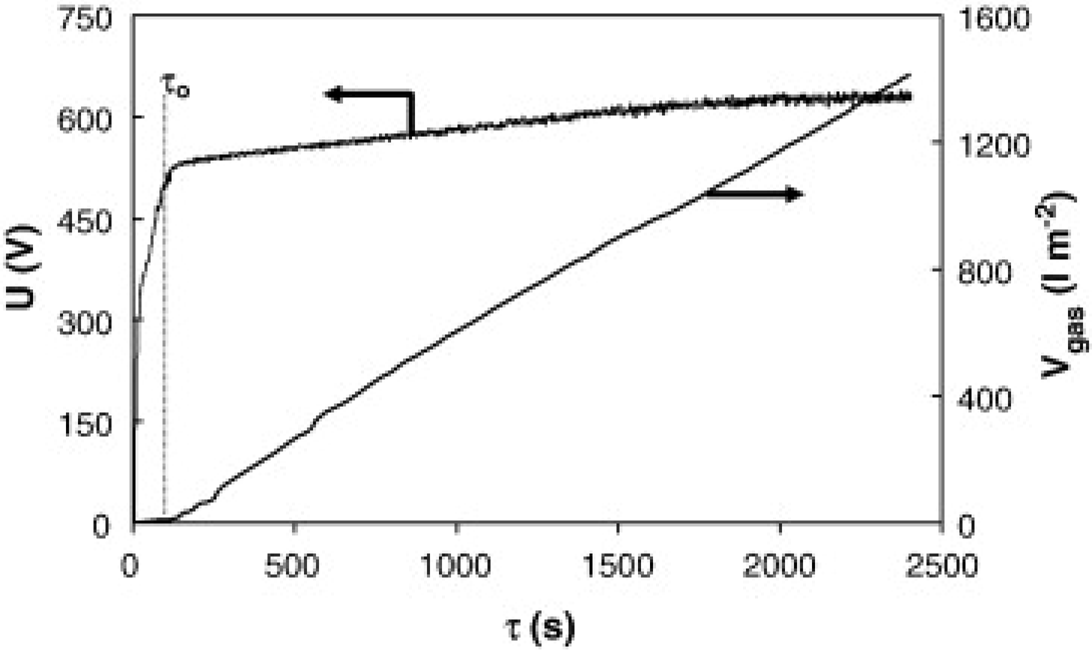

Figure 3.11 Experimental data for gas evolution and voltage development during DC PEO of Al-6082, with an electrolyte containing 1 g L^{-1} of KOH and a current density of 935 A m^{-2} [147].

Examining Figure 3.11, it can be seen that, once PEO discharges had become established (at ~500 V), gas evolution commenced and the rate of gas production remained approximately constant after this at ~0.6 L m-2 s-1. The current density was 935 A m-2, so the maximum rate of gas evolution, v̇, during conventional electrolysis (Faraday yield) would be given by

$$\dot{v} = \frac{i}{4F}\frac{RT}{P} \tag{2}$$

where i is the current density, F is the Faraday constant, R is the gas constant, T is temperature, and P is gas pressure. This gives a gas evolution rate of ~0.06 L m^{-2} s^{-1}, so the observed rate is an order of magnitude greater than the maximum expected value. It should be emphasized at this point that PEO is not a conventional electro-chemical process, but the source of this gas is nevertheless of interest.

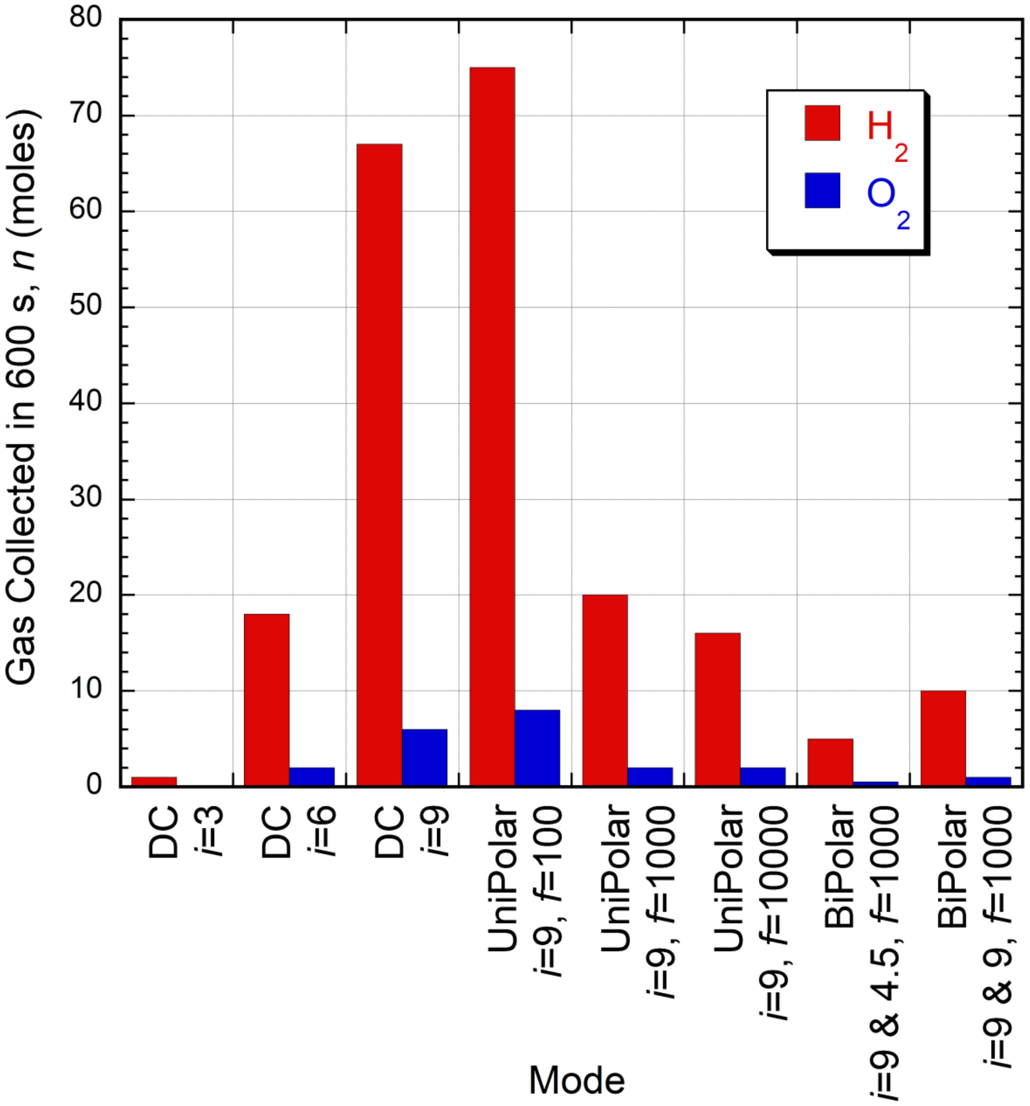

Figure 3.12 Experimental data for the rates of evolution of hydrogen and oxygen gases during PEO under various sets of conditions [148]. (The current densities, *i*, are in A dm^{-2} and the frequencies, *f*, are in Hz.)

The results shown in Figure 3.12 may seem a little strange, since the expectation is that only oxygen should be evolved at the anode, and even that might not occur if most of the oxygen produced (electrochemically) goes into converting the metal to oxide. This is a clear indication that hydrogen gas, or at least gas in excess of the Faraday yield, is being generated as a consequence of the plasma discharge process. This is plausible since substantial quantities of water will be thermally decomposed, creating various hydrogen- and oxygen-containing species in the plasma. It is thermodynamically favourable for the hydrogen and oxygen in the plasma to recombine as it cools to reform water. However, if there are species in the plasma with a strong affinity for oxygen (as there will be during successful PEO processing) then this may not be possible, and hydrogen gas could be released. Furthermore, the quenching is very rapid and it is certainly plausible that some residual gas could be left due to kinetic effects, and perhaps partly because an imbalance between hydrogen and oxygen had been created as the plasma cooled. This mechanism, which is not electro-chemical in nature, would therefore not be subject to Faraday yield limits. Instead, the amount of gas would only be limited by the total energy input, which is considerably more than is required to produce this quantity of gas.

Such effects, which could take place within both anodic and cathodic plasmas, are likely to confuse the interpretation of gas evolution rates. However, it does seem clear that, in the cathodic part of the cycle, there is a high likelihood of hydrogen ions being able to move rapidly through the electrolyte to the surface of the residual oxide layer. Once there, they may acquire electrons that have passed through the layer, so that hydrogen gas is evolved. This may depend on how effectively the surface concerned catalyses this hydrogen ion discharge, as indeed it does during conventional electrolysis of water [99]. Nevertheless, it is well known in practical terms that hydrogen gas does tend to be evolved at relatively high rates during PEO. The notion of the “valve metals” presumably arose from the idea that electrons could move though the oxide layer in this direction (without causing dielectric breakdown), but not in the other direction (from electrolyte to metal). However, as outlined in §3.1.1 above, there is no clear reason to expect this. An alternative explanation is that the high mobility of H^+ ions in the electrolyte allows them to reach the oxide surface at rates sufficient to carry much of the imposed current, reducing the field across the oxide layer and hence the likelihood of dielectric breakdown. If this is indeed largely a dynamic effect, then some dependence on supply frequency might be expected. This is explored in the next section.

3.4 Cathodic Discharges and the Effect of Supply Frequency

The cathodic part of the cycle has attracted increased attention in recent years. It has been clear for some time [40] that PEO coatings produced using AC are in general of superior quality (harder and denser, for example) than those produced under corresponding (anodic) DC conditions. It has also been shown that coating quality is improved if the cathodic voltage is raised [3] or if the ratio of cathodic current to anodic current is increased [153]. What actually happens during the cathodic half-cycle is less clear. In the vast majority of cases, at least under normal conditions, discharges predominantly occur during the anodic half-cycle, although current does flow in both half-cycles.

However, discharges have been observed in the cathodic half-cycle under some conditions, particularly when the electrolyte is strongly alkaline [98, 154-156] and for relatively thick coatings. It is also worth noting that PEO coatings have been produced under conditions in which cathodic discharges predominate. For example, Stojadinovic et al. [112] reported cathodic PEO of Mo. From a thermodynamic point of view, it seems likely that substrate material can become oxidised as readily within a cathodic discharge as within an anodic one. On the other hand, while there have been suggestions about this [157, 158], the mechanism of charge transfer during the cathodic part of the cycle, in the absence of cathodic discharges, is often rather unclear. The most likely one, however, is simply the discharge of hydrogen ions, leading to evolution of hydrogen gas (see §3.3 above). This is clearly unproductive in terms of coating growth, although it is possible that the associated charge redistribution could help promote the anodic discharges in the subsequent half-cycle. The fact that cathodic discharges appear to be favoured by strongly alkaline electrolytes (and by the coating already being relatively thick) may relate to inhibition of hydrogen gas formation (respectively via a shortage of protons and a greater difficulty in moving them through the coating).

In practice, PEO processing is usually carried out using AC, with most coatings, both in research work and in technological usage, often being produced at 50 or 60 Hz—although higher frequencies are becoming more popular. The cycle period is thus commonly about 20 ms, which is sufficiently long to allow extended cascades during each (anodic) half-cycle. There is considerable interest in how the process changes as the supply frequency is increased, such that the cycle period is no longer large compared with the inter-discharge period, or the discharge period itself. There are several reports [159-161] that an increase in the supply frequency (with maximum values usually around 1.0-1.5 kHz) leads to a reduction in coating growth rates, although it must be recognized that others have reported different effects [43, 44, 162]. As with many aspects of PEO, there is considerable complexity and scope for extraneous factors to exert an influence. There have also been reports that the coating microstructure becomes finer and denser as the frequency is increased, which might be regarded as beneficial.

There may be potential for increased energy efficiency by promoting discharges in the cathodic part of the cycle, since it seems likely that these will lead to coating growth, whereas hydrogen evolution will not do this (and is also potentially hazardous).

3.5 “Soft plasma” PEO conditions

Over recent years, a new area of research within PEO has emerged which is the so called “soft-sparking” or “soft” regime [2, 43, 45, 65, 80, 93, 150, 163-168]. Normally, as the thickness of a PEO coating increases, the through-thickness electrical discharges become more intense and longer-lived. This often places an upper limit on the thickness of PEO coatings, since intense discharges start to destroy the coating. However, under certain conditions, termed the soft regime, this can be avoided and coating microstructures can be improved (i.e. more homogenous and no large through-thickness discharge channels), with reduced energy consumption.

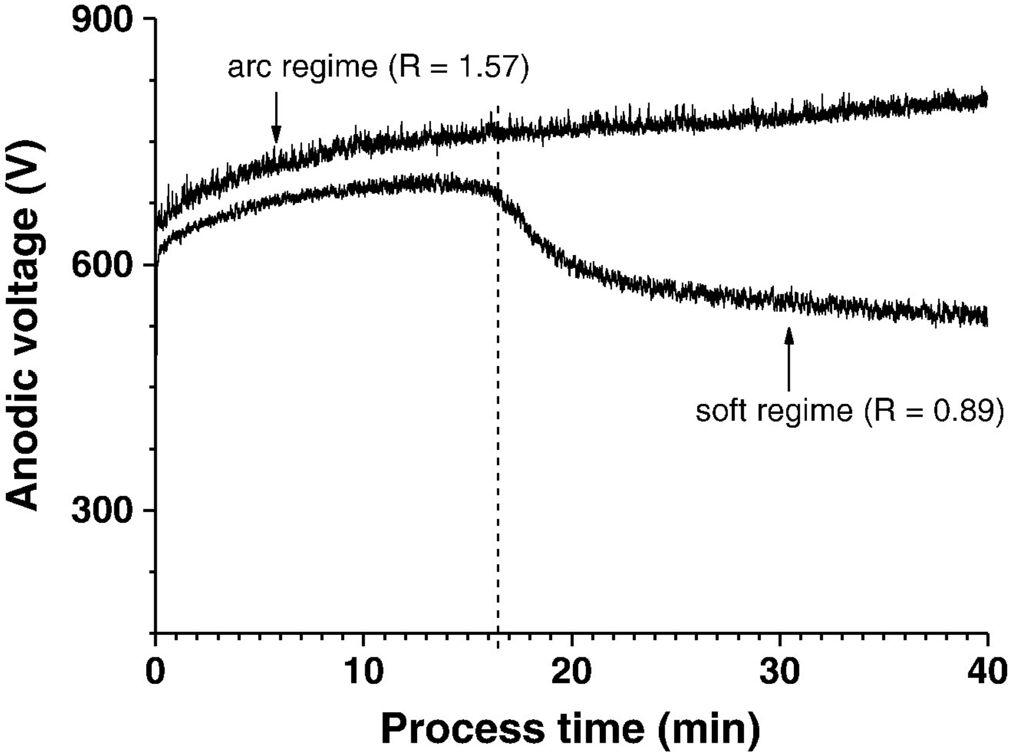

Figure 3.13 Evolution of the anodic voltage over the process duration under standard conditions (termed arc regime) and soft regime conditions, with the transition to soft regime indicated by the dashed line[164].

In such cases, the process starts conventionally, but, once a certain coating thickness or processing time has been reached, a reduction is observed in the applied anodic potential (under constant current conditions, see Figure 3.13) and the discharges become almost invisible, although coating growth continues and actually increases [45, 168]. This is illustrated in Figure 3.14—note that (d) has an integration time longer than (a)–(c) by a factor of 200. Clearly, the quantity of light being emitted is much less in this case, although it can be seen in Figure 3.14(d) that there are still preferred locations for its emission. The ratio of anodic to cathodic charge (termed the charge transfer ratio, *R*) must be less than unity for the transition to occur [45], although the mechanisms that require this are still unclear. The transition to the soft regime apparently occurs sooner for higher current densities and higher AC supply frequencies [43, 168]. The literature is largely focused on Al, but there are also reports for Mg [80], Zr [2] and pre-anodized Al [165, 166].

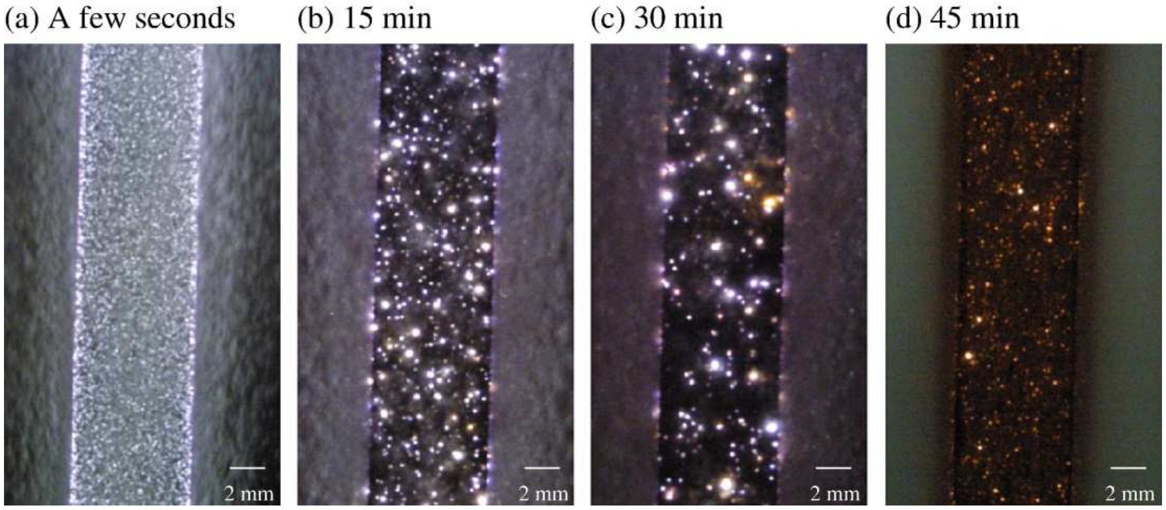

Figure 3.14 Side-view photographs [45] of aluminium alloy samples at different times during PEO processing ($R = 0.89$). The integration time was between 8 and 10 ms for photographs (a), (b) and (c), but 2000 ms for (d).

It is observed that the diameters of "melt-pools" formed around discharge channels remains approximately constant [45] after the soft regime has been established (whereas, under standard conditions, these diameters tends to increase linearly with processing time). In a tracer study [93], it was found that all new coating growth occurred at the substrate-coating interface after the transition to lower applied potential occurred, which would explain why the melt-pool diameters on the coating free surface remain constant.

Clearly, this transition could be of considerable industrial interest, since one of the major issues with PEO is the relatively high energy consumption. In fact, data have been published that give information about such a reduction in rates of energy consumption as the soft regime is entered. Figure 3.15 shows how the reduction in anodic potential that accompanies the onset of the soft regime occurs earlier when R is lower, and also plots the associated reduction in specific energy consumption rate [168]. It can be seen that there is a significant fall (of around 40%). None of these publications, however, has presented a mechanistic explanation of how or why the process is taking place differently in the soft regime.

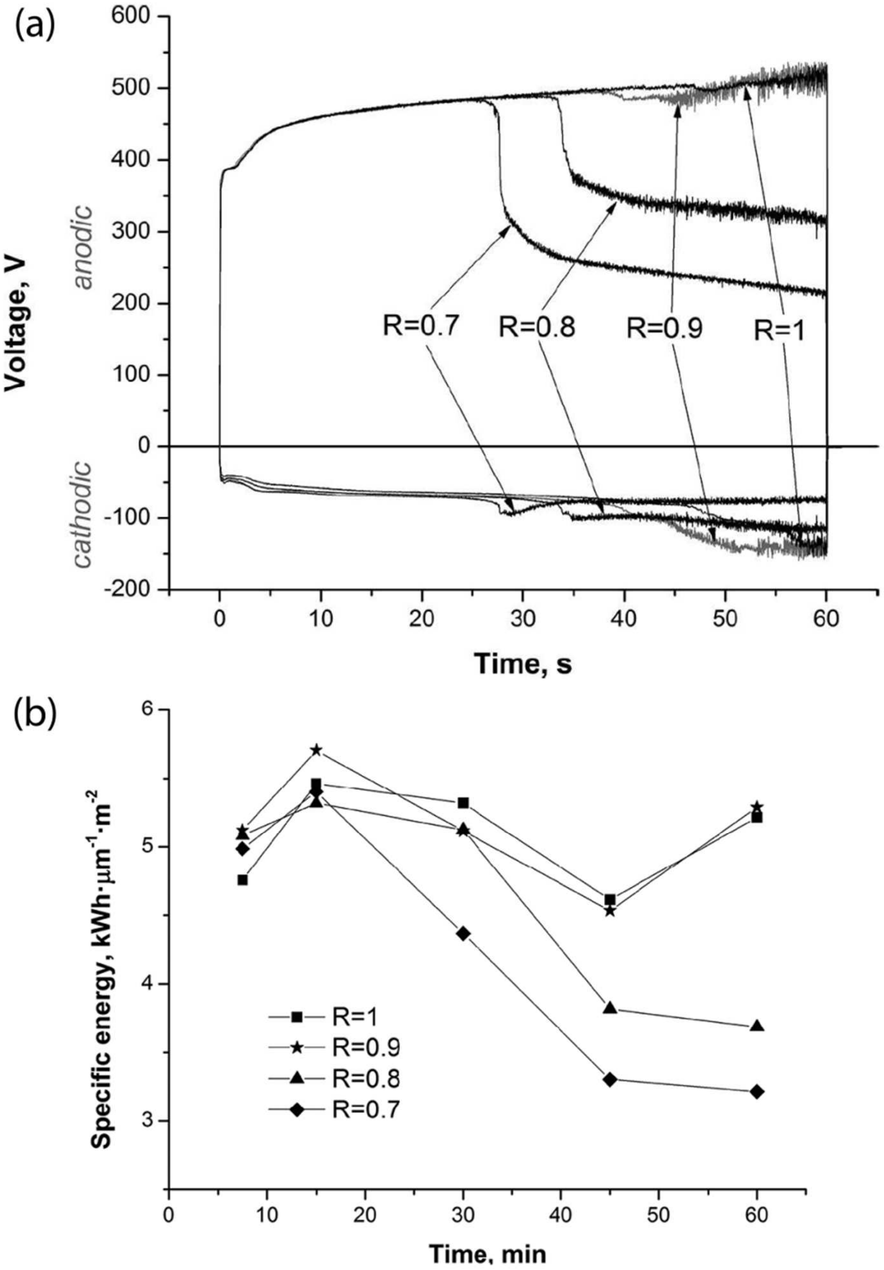

Figure 3.15 Plots of data [168] obtained during PEO processing of Al at 100 Hz, with a fixed anodic current density of 10 A dm^{-2} and four different values of R (ratio of anodic to cathodic current densities), showing (a) anodic and cathodic voltages needed to maintain these current densities and (b) corresponding rates of energy consumption, per unit volume of coating produced.

A possible explanation for the soft regime is that a large number of small discharges are taking place at the metal/oxide interface, but these are not developing in the way that they normally do, and so do not reach the free surface of the coating (such that there is little or no light emission). This is not entirely consistent with information such as that in Figure 3.14(d) and it is clear that further study is needed. At present, it is unclear whether such (small) individual discharges can be identified in some way (for example, using the small area monitoring technique) or even whether they are anodic and/or cathodic. In addition, there is no explanation so far of why raising the potential, or the charge flow, in the cathodic part of the cycle should stimulate this transition, or any indication of the effects of changing the electrolyte composition (e.g. the pH). Until the effect is better understood, its exploitation is likely to remain limited.

Chapter 4

Experimental Methods

4.1 PEO processing

4.1.1 Processing conditions

Two industrial processing machines were used in the present investigation, both supplied by Keronite International Ltd. The first is a 10 kW power supply unit, which applies a nominally sinusoidal 50 Hz AC waveform. A schematic of this system is shown in Figure 2.2, along with an example of the applied waveform and evolution of the peak current and voltage in Figure 2.3. The unit contains an array of capacitors in series with the process tank, which control the current delivered to the sample. Additionally, the charge delivered during anodic and cathodic polarisation of the sample is equal and opposite. The sample is electrically connected to the output of the power supply and suspended in the electrolyte. The process tank contains a stainless steel mesh, which acts as the counter-electrode. The volume of the tank is approximately 25 L, and the electrolyte is circulated through a heat exchanger to maintain the temperature ~20 °C. A constant capacitance condition was set giving an initial current density of approximately 15 A dm^{-2}. Coatings produced in this way have been well characterised, and have a growth rate of ~1 μm min^{-1} [42].

The second machine is a 100 kW power supply unit. The basic operating principle of this set-up is the same as above, but there is much greater control over the applied electrical conditions. A schematic of the applied waveform is shown in Figure 4.1. The maximum current or voltage is defined by the operator, within the limitations of 110 A or 900 V during anodic polarisation and 200 A or 300 V during cathodic polarisation. The time period ($\tau = 1/f$) is restricted to 400 μs $\leq \tau \leq$ 20 ms, giving a frequency range of 50 Hz to 2,500 Hz, and anodic and cathodic half-period (t_a and t_c) must be ≥ 50 μs. The tank itself is stainless steel and acts as the counter-electrode. The volume of the tank is approximately 25 L, and the electrolyte was circulated through a heat exchanger to maintain the temperature ~20 °C. Processing in the 100 kW Keronite™ rig has a much larger degree of freedom on the electrical parameters. To ensure comparisons could be made between samples, all samples were processed with $t_a = t_c$ and an equal anodic and cathodic current density of 31 A dm^{-2}.

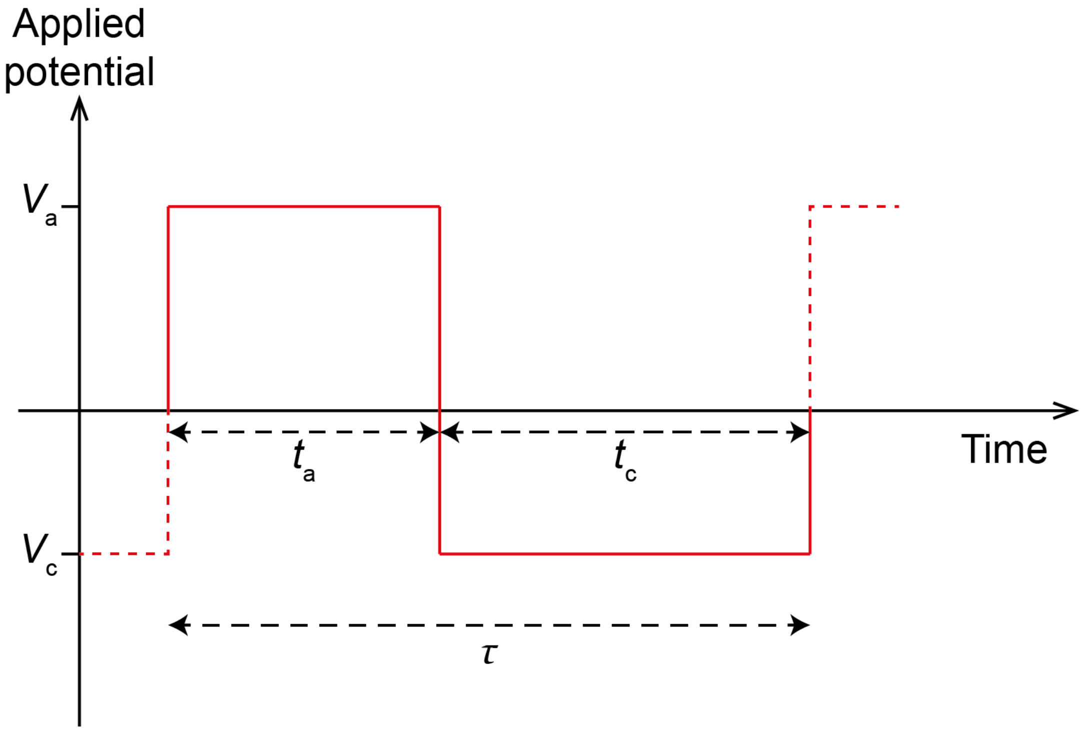

Figure 4.1 Schematic of the waveform produced by the 100 kW processing rig.

The electrolyte used was a standard commercially available aluminium electrolyte. The exact composition is commercially sensitive, but the approximate composition is 1–2 g L^{-1} potassium hydroxide (KOH), 3–5 g L^{-1} sodium silicate (Na_2SiO_3) and 3–5 g L^{-1} tetra-sodium pyrophosphate ($Na_4P_2O_7$).

Once samples had been processed, they were thoroughly rinsed several times in de-ionised water to remove any residual electrolyte, and dried in warm air.

4.1.2 Sample preparation

Several different sample alloys and geometries have been used in the present work. A summary of these samples is given in Table 3. Often it was necessary to mount large samples in an insulating resin, with just one face exposed. An epoxy resin (Struers Epofix) was used, which is a low shrinkage cold mounting resin. This was selected so that when large samples (>50 mm in all dimensions) were produced there were not large residual stresses or cavities formed.

Samples used for small area investigations typically have a small wire mounted in parallel with a bulk sample. These wires were produced by cutting a thin section from the bulk material and swaging a wire through successively smaller dies until the desired diameter was achieved. The wire and bulk sample were connected to a pair of PVC insulated twisted wires extending out of the tank where a resistor for current monitoring connected the ends of the wires.

Bulk samples in the form of bars had a tapped hole cut in them, with a threaded metal rod screwed into it. The metal rod was insulated from the electrolyte and screwed into a block, which was attached to the bus bar. Plate samples, which were mounted in resin, had six Al wires spot-welded to the back. These wires formed an electrical connection to a removable threaded rod, so that samples could be mounted in the SEM chamber.

Other plate samples had a clearance hole drilled, centred near the edge of one side. An Al block, with an M5 tapped hole, was insulted with wax (Suprawax) except one side. A nylon screw attached the plate to the Al block, which was connected to the bus bar through an insulated rod.

The cross-section of the bar (or plate) and wire were exposed and ground with 800 grade SiC paper. Plate samples were cleaned in acetone, and used without further surface treatment.

Substrate alloy and dimensions	Processing conditions	Experimental usage
Al-6082 Ø = 12.8 mm cylindrical bar, mounted in epoxy resin	10 kW Keronite™ rig 50 Hz i = 15 A dm^{-2}	High-speed video monitoring of discharge cascades on bulk samples.
Al-6082 25.4 mm square section bar, mounted in epoxy resin + Ø = 1.00 ± 0.01 mm wire	100 kW Keronite™ rig 50 Hz & 2,500 Hz i = 31 A dm^{-2}	Synchronised high-speed video monitoring and electrical measurements of discharges
Al-2014 2 × 25 × 25 mm plates mounted in epoxy resin + Ø = 0.88 ± 0.01 mm wire	100 kW Keronite™ rig 50 Hz & 2,500 Hz i = 31 A dm^{-2}	Effects of discharge cascades on the microstructure of PEO coatings, with synchronised high-speed video monitoring and electrical measurements
Al-1050 50 × 25 × 1.2 mm plates	100 kW Keronite™ rig 50 Hz & 2,500 Hz i = 30 A dm^{-2}	Mass gain of samples at different processing frequency, and monitoring of cathodic discharges
Al-1050 28 × 10 × 1.2 mm plates, coated with wax on the edges and one side	100 kW Keronite™ rig 50 Hz & 2,500 Hz i = 30 A dm^{-2}	Monitoring of gas evolution at different processing frequency

Table 3 Summary of the samples, and PEO processing conditions used in the present work.

4.2 High-speed video

High-speed video imaging was performed using a Photron Fastcam SA 1.1 or Phantom V12.1, these are effectively equivalent cameras from different manufactures. The sample surface was viewed through a glass window in the electrolyte tank. The distance between the camera and sample was approximately 300 mm. A schematic representation of the experimental set-up is shown in Figure 4.2. Both cameras have an internal memory of 16 GB, which limits the possible recording time. This memory can be partitioned such that multiple shorter sequences can be captured before the data has to be transferred out, which can take up to ~30 minutes. The full frame resolution in each case is 1 MB. However, this limits the acquisition rate to under 10,000 frames per second. Higher frame rates (temporal resolution) can be achieved by reducing the image frame size. Limiting the image size also allows longer sequences to be captured for the same amount of memory. The spatial resolution is determined by the optics of the system (i.e. the lens used and the distance between the sample and camera).

During the study of localised discharge cascades in §5.1, the Photron Fastcam SA 1.1 was used with the acquisition rate set at 180,000 frames per second (5.5 μs exposure time). The linear spatial resolution was determined to be 12 ± 1 μm (i.e. an area of 144 μm^2 per pixel). Images comprised 128 × 128 pixels, covering an area of 2.36 mm^2, located near the centre of the bulk sample. Image sequences were acquired after various PEO processing times, corresponding to coating thicknesses in the range of 5 μm to 60 μm. Image acquisition periods involved accumulating 17,500 frames over about 100 ms. For the small area investigation in §5.3 the camera employed was a Phantom V12.1, with the acquisition rate set at 180,064 frames per second (5.12 μs exposure time). The linear spatial resolution was 13 ± 1 μm per pixel. Images comprised 128 × 128 pixels, covering the entire small area sample (circle of diameter 0.88 mm).

In order to capture the bubble kinetics in Chapter 6 the Photron Fastcam SA 1.1 was used and synchronised with electrical measurements. A larger frame size was used with an improved linear spatial resolution. This limited the acquisition rate to 125,000 frames per second (8 μs exposure time). The linear spatial resolution was 9 ± 1 μm (i.e. an area of 81 μm^2 per pixel). Images comprised 192 × 144 pixels, covering an area of 2.24 mm^2, large enough to capture the small area sample (a 1 mm diameter wire). Image sequences were acquired after various PEO processing times, using different frequency waveforms.

Due to the very high frame rates involved it was necessary to illuminate the sample surface to be able to see the bubble kinetics. This was done using a very intense flash, which had a duration of approximately 10 ms. The maximum total record time of the camera (approximately two seconds) was employed since the flash could only be triggered manually. The illuminated period was identified and saved, typically this was around 1,500 frames covering 12 ms, which allowed further illuminations to be captured during the same PEO treatment.

Monitoring the number of anodic and cathodic discharges in Chapter 7 was done using the Phantom V12.1 camera, with the acquisition rate set at 100,000 frames per second. The linear spatial resolution was 34 μm per pixel. Typical images comprised 160 × 160 pixels, covering an area of 30 mm^2. This area was from the centre of bulk sample plates of Al-1050. Recordings were performed throughout processing in sequences which lasted 173 ms each.

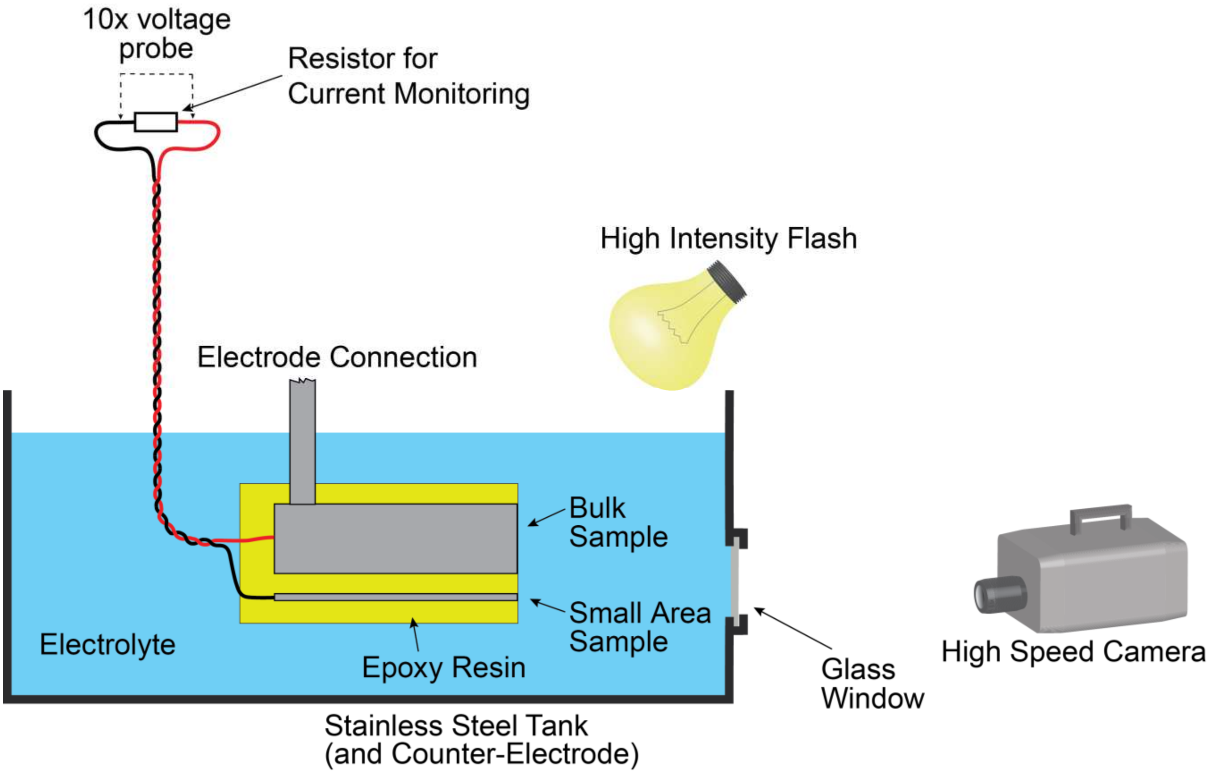

Figure 4.2 Schematic representation of the experimental set-up. The high-speed camera is focused on the small area sample. The high intensity flash was only used during certain experiments.

4.3 Small area electrical monitoring

The small area electrical monitoring technique was developed by Dunleavy et al. [47, 74, 77]. The principle behind the technique is that discharge events on a small area occur in much the same way as on larger areas. However, on a small area, the probability of having more than one discharge event occurring at a given time is low. Therefore, by measuring the current that flows through the small area, the current-time profile of individual discharges may be obtained.

Electrical data were collected using a four-channel, 8-bit resolution PC oscilloscope (Pico Technology, Picoscope 6403), with a sample interval of between 102.4 ns and 480 ns. The Picoscope was operated using a desktop PC with a USB opto-isolator, which converts an electrical signal to an optical signal, and then back to an electrical signal. This was necessary to avoid ground loops between the PC and floating ground of the power supply. The voltage across the electrolyte tank was measured using a 100× potential divider, or directly using an active differential probe (Pico Technology TA043) with 100× attenuation, as shown in Figure 4.3. The bulk current was determined by measuring the voltage drop across a 1 Ω resistor connected in series between the counter-electrode and the power supply. The end of a wire was used as the small area during the present work. The wire was connected to a bulk substrate through a resistor, as shown in Figure 4.2. The connecting wires were twisted together to reduce electrical noise in the current signal. The current was determined from the voltage drop across the resistor, measured using an active differential probe (Pico Technology TA043), with 10× attenuation.

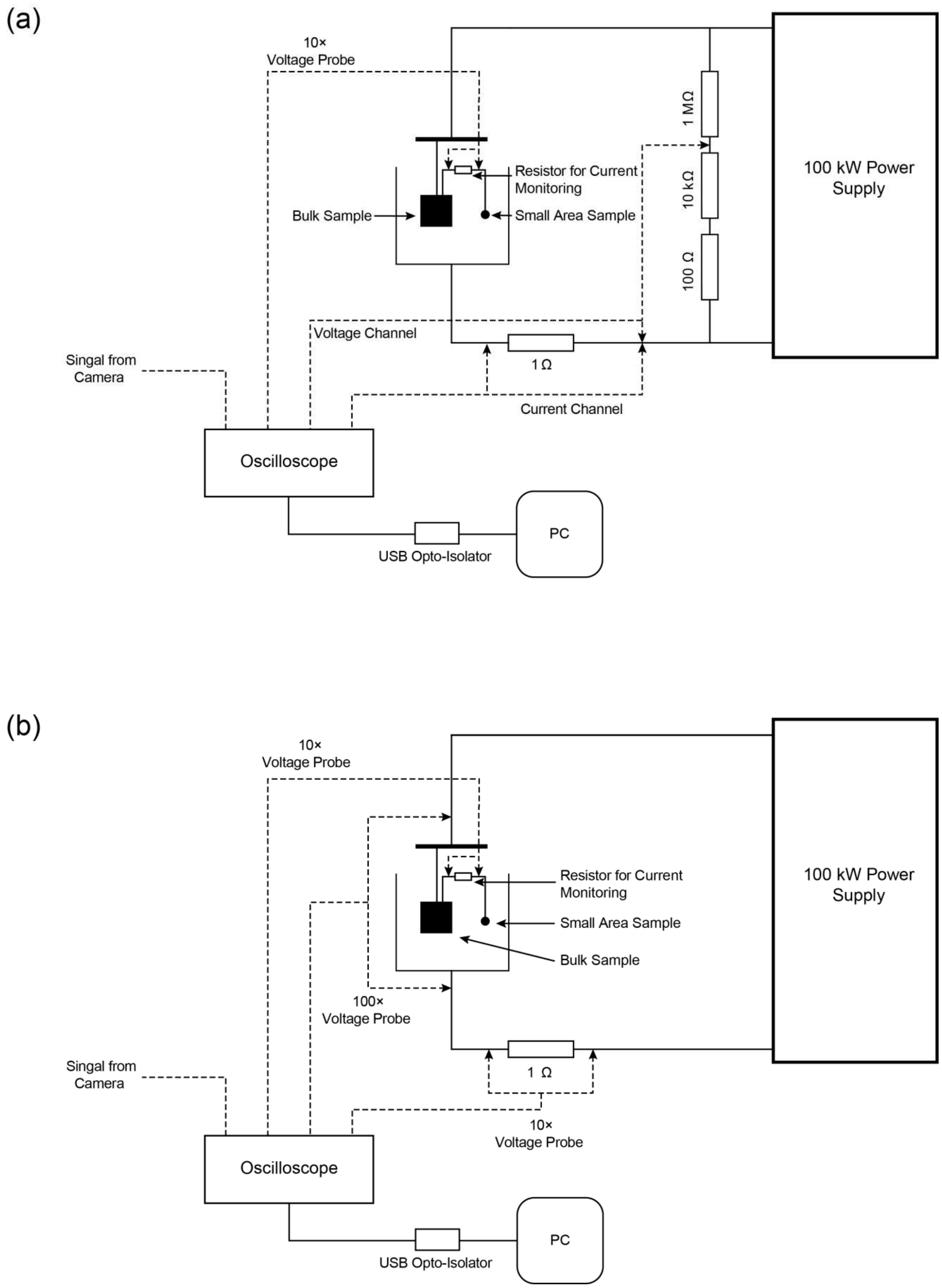

Figure 4.3 Schematic diagram of the electrical monitoring set-up using (a) a 100× potential divider, and (b) a 100× differential voltage probe.

The high-speed camera (Photron Fastcam SA 1.1) was able to output a TTL trigger signal (+5 V, 10 μs square wave) within 100 ns of the camera being started. Since each frame corresponds to several μs, the 100 ns delay is considered negligible. Similarly, the Phantom V12.1 outputs a ready signal of +5 V when waiting for the capture signal (from the control software), that drops to 0 V as soon as the camera starts recording. The trigger signal was connected to one channel of the Picoscope in both cases and electrical data recording was triggered from this channel. During all experiments, data were collected without any breaks for the duration of the camera records.

The short PEO treatments studied in §5.3 required additional circuitry. This is set-up is shown schematically in Figure 4.4. An arbitrary function generator (TTi TG1010A Programmable 10 MHz Function Generator) was used to supply a single square wave pulse of +5 V of duration one second. This signal was used to trigger the recording of the oscilloscope and high-speed camera, as well as supplying power to a coil around magnetic contacts of the reed relay switch, causing the switch to close and complete the circuit between the small area and bulk samples. This ensured the camera, oscilloscope and short treatment were all initiated at same time, giving synchronised data.

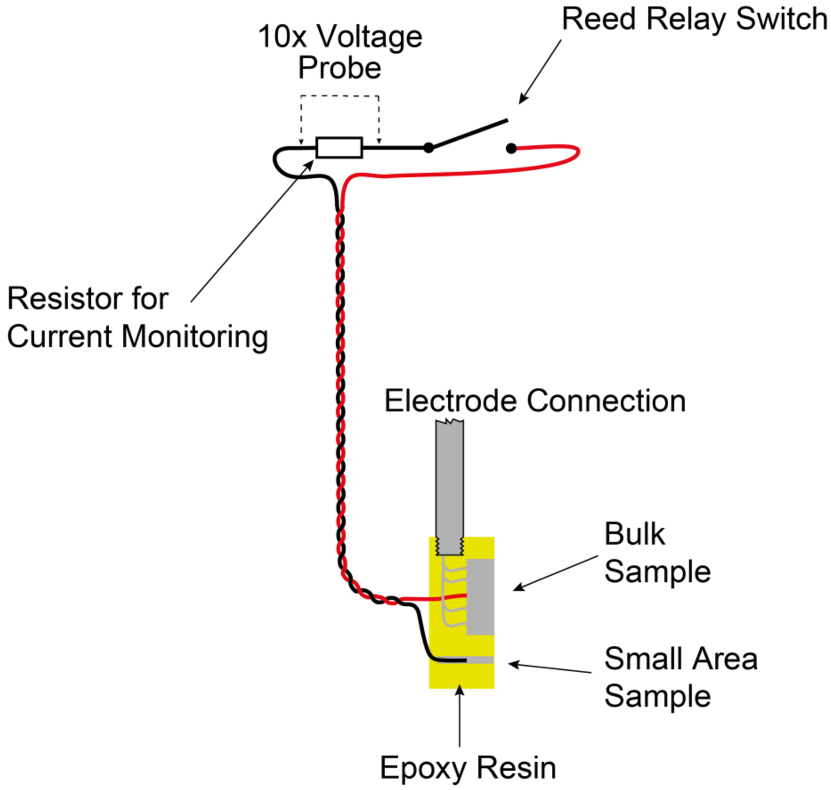

Figure 4.4 Schematic diagram of the sample and electrical set-up used for short PEO processing experiments.

4.4 Image processing

Individual frames were 8-bit or 12-bit greyscale images. These data were processed using the Photron FASTCAM viewer, Phantom Camera Control software, Matlab and the image processing software ImageJ. Superimpositions of a complete video sequence were produced by summing the pixel values of corresponding points in a sequence of images, which were then converted back into 8-bit greyscale images. In certain cases, superimpositions were created only from frames covering a particular half-cycle, rather than the whole duration of the sequence. Total intensity profiles were calculated by summing all the pixel values for each frame in a sequence. Local maxima in light intensity of the summed images were found and circular regions of interest were defined, centred on these maxima. Intensity–time profiles from these circular regions were produced in a similar manner to the total intensity profiles. The volume viewer "Plugin" in ImageJ was used to create perspective views of frame sequences. For the perspective views, the contrast was reversed, with the transparency set so that low value pixels were transparent and high value pixels were opaque.

Video images from capturing bubble kinetics were treated with an unsharp mask, a common image processing technique, to enhance edge contrast. For a particular discharge, the synchronised video sequence shows the expansion and subsequent collapse of a bubble. A sequence is presented in §6.3 from a period when there were no other bubbles in the vicinity from previous discharges, which, if present, can perturb and interact with the growing bubble. Bubble radii were estimated by drawing an ellipse of best fit around a bubble and converting the corresponding area to an equivalent radius assuming a circular cross section.

Evaluating the number of discharges in a video sequence was performed using a script written in Matlab. Image sequences were imported, along with corresponding electrical data, which determined whether images were captured during an anodic or cathodic half-cycle. Peaks in light intensity were found after a Gaussian blur function was applied to smooth the image, which, along with a peak height threshold, eliminated noise being detected as a false peak. For each period of applied potential, peaks were sorted into cascade locations, which were defined by a maximum spatial separation. The number of discharges occurring in each location was then counted, and summed over the whole image sequence for anodic and cathodic discharges separately. An illustrative example is shown in Figure 4.5. It can be seen that there are three peaks detected (red dots) in Figure 4.5(a), two of which persist into the next image (Figure 4.5(b)), and are therefore not counted as new discharges. However, a new peak has appeared, so is added to the discharge count. Figure 4.5(c) has two peaks, both of which are present in the preceding image, so are not counted. Four discharges would be counted for this set of three images.

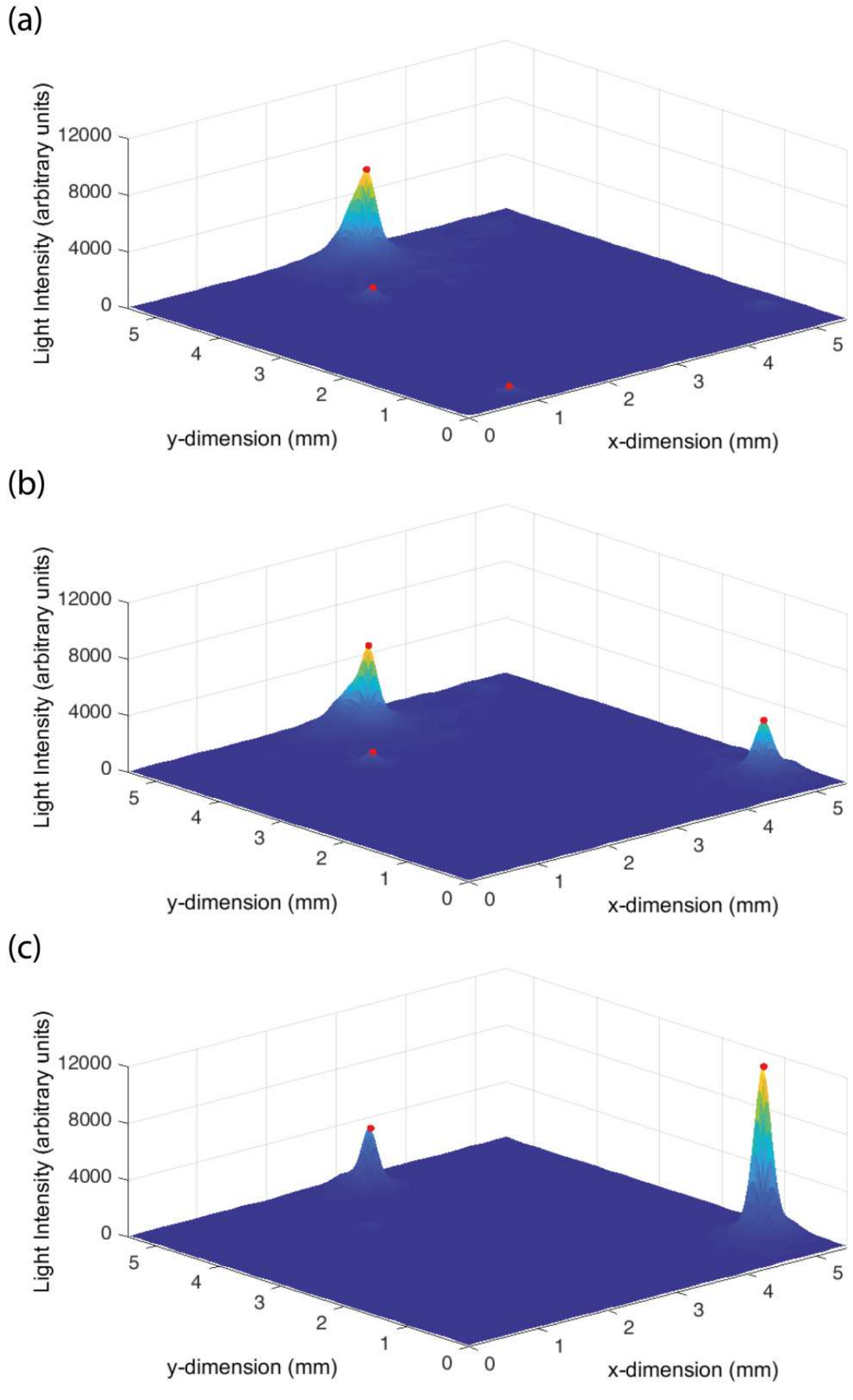

Figure 4.5 Three sequential high-speed video images plotted at a surface, with pixel values represented at height. Peaks detected by the Matlab script are superimposed with a red dot in each case.

4.5 Microstructural investigation

4.5.1 Metallographic preparation

When it was necessary to cut samples, a Struers Secotom-10 precision saw was used, with a SiC blade and water-based cutting fluid. For samples mounted in cross-section, the burr was removed using coarse SiC grinding paper before mounting in conductive Bakelite resin in a hot press. Samples were then ground on successive grades of SiC grinding paper, usually finishing with 4000 grit paper. Finally, samples were polished with 6 μm, and 1 μm diamond suspension.

4.5.2 SEM microscopy

The free surface of coatings were examined using scanning electron microscopy (SEM) in both secondary electron (SE) and back-scattered electron (BSE) mode. Prior to imaging, samples were sputtered (Emitech K550, 30 mA for 3 minutes) with a thin layer of gold to prevent surface charging.

SEM observations were carried out on several instruments: a JEOL JSM 5500LV for standard SE imaging of the coating free surface, CamScan MX2600 for large samples and BSE imaging of the free surface, and Phenom Pro X desktop SEM for BSE imaging of cross-sections.

For short PEO processing experiments in §5.3, an initial PEO coating was created by processing for 30 minutes. Samples were removed from the electrolyte, washed in deionised water, and dried in a stream of warm air. A thin layer of gold was sputtered onto the surface for SEM observation. The entire small area sample (end of the 0.88 mm diameter wire) was imaged in BSE mode, in a CamScan microscope, using an accelerating voltage of 10 kV and a working distance of 33 mm. A complete map of the sample surface was created by stitching ~16 images together in Photoshop. After a short (1 s) PEO treatment had been applied to the small area sample, SEM imaging was carried out again, including addition gold sputter coating. This was done twice in sequence on the same sample with a 50 Hz supply and once (on a different sample) at 2,500 Hz.

4.5.3 Thickness measurements

Coating thickness measurements were made form SEM cross-section images. ImageJ was used to define both edges of the coating, by thresholding the images and tracing a line along the boundaries. The mean separation of the two lines was taken as the coating thickness, and the standard deviation calculated for the error. The length over which the measurements were made was in excess of 15 times the coating thickness in all cases.

4.5.4 X-ray computed micro-tomography[†]

A small area sample was scanned using a Skyscan 1172 X-ray micro-tomograph. The resolution was ~1.2 µm. Serial sections, in the form of a stacked set of radiographs, were imported into ScanIP (software for 3D imaging, visualisation and analysis). Prior to reconstruction of the 3D geometry, the radiographs were thresholded, using in-built segmentation algorithms, and surfaces were smoothed using a recursive Gaussian filter.

4.6 Gas collection

The gas produced in PEO processing is typically a mixture of H_2 and O_2, so storing large quantities is potentially hazardous. In order to monitor the gas evolution rate over extended processing times it was necessary to use a small sample with a low current (but the same current density as standard samples). However, the 100 kW processing rig cannot deliver such small currents reliably. Therefore, two samples were processed in parallel, one large shunt sample, and another smaller monitoring sample. The gas was only collected from the smaller monitoring sample.

[†] X-ray computed micro-tomography was performed by Dr J. Dean.

A funnel was placed over the monitoring sample, with a hole in the side to allow the rod making the electrical connection to pass through. The funnel was sealed to the rod to prevent gas escape, using a silicone gasket, which was attached to the rod and pushed up against the funnel. A measuring cylinder filled with electrolyte was placed over the funnel, so that gas evolved by the monitoring sample would be collected in the cylinder. The counter-electrode was a stainless steel ring lowered into the tank, but kept above the bottom of the funnel to avoid gas being collected from the counter-electrode. The shunt sample was also positioned above the bottom of the measuring cylinder to prevent unwanted gas collection. This arrangement is depicted in Figure 4.6. Photographs were taken of the measuring cylinder every 30 s, and the volume of gas could easily be recorded from these images after processing.

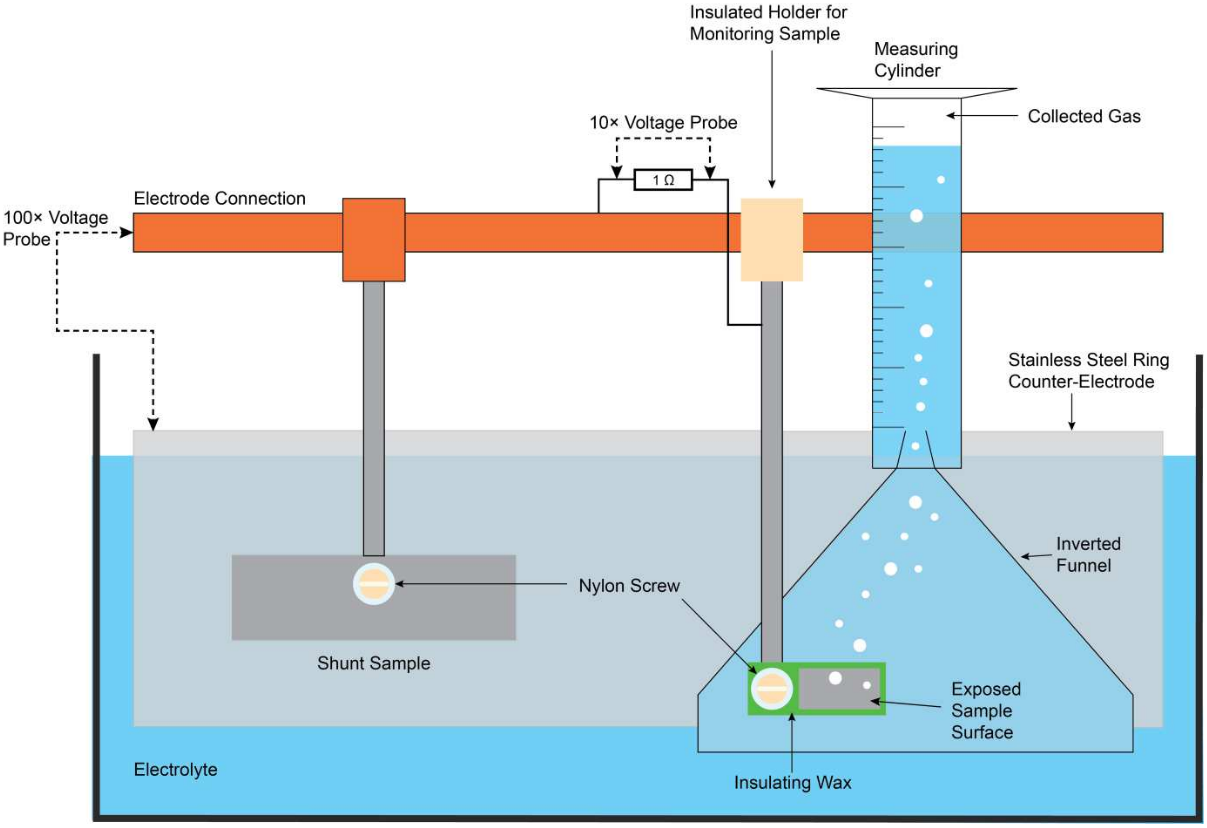

Figure 4.6 Schematic side profile view of the gas collection set-up. Two samples are processed in parallel, with the gas only collected from the smaller monitoring sample. Current flowing through the monitoring sample was measured using the voltage drop across a 1 Ω resistor, and applied potential was measured between the bus bar and counter-electrode.

The monitoring samples were Al-1050 with dimensions of 28 × 10 × 1.2 mm. A wax coating (Suprawax) was applied on one side and around the edges of each sample, leaving an exposed area for processing of 20 × 10 mm. Shunt samples were also Al-1050 and had an exposed area of 2,500 mm^2. Samples were processed such that the current flowing through the monitoring sample was ~0.6 A, to achieve a current density of around 30 A dm^{-2}. Current flowing to the monitoring sample was measured by making the electrical connection to the bus bar through a 1 Ω resistor. The voltage drop across this resistor was measured using an active differential probe (Pico Technology TA043) with 10× attenuation. The shunt sample used for 50 Hz processing was the same as the samples used for mass gain (50 × 25 × 1.2 mm), however, when processing at 2,500 Hz a different geometry shunt sample was required to keep the current flowing to the monitoring sample approximately constant. These were 120 × 10 × 1.2 mm, so that they had the same width as the monitoring sample. This was required so that the high local electrical field at the sample edges would be similar in both samples, keeping the current at a more consistent value.

The total current and the current flowing to the monitoring sample were recorded, and the data are shown in Figure 4.7. The total current was set at a higher value (8.1 A) for the 2,500 Hz case, than the 50 Hz case (5.0 A). This was done so that the current flowing through the monitoring samples was approximately the same in both cases at ~0.6 A, and the correct current density (30 A dm^{-2}) was achieved. The current is less uniform for the high frequency case, and the power supply did not hold the current at the set value as consistently as at the lower frequency.

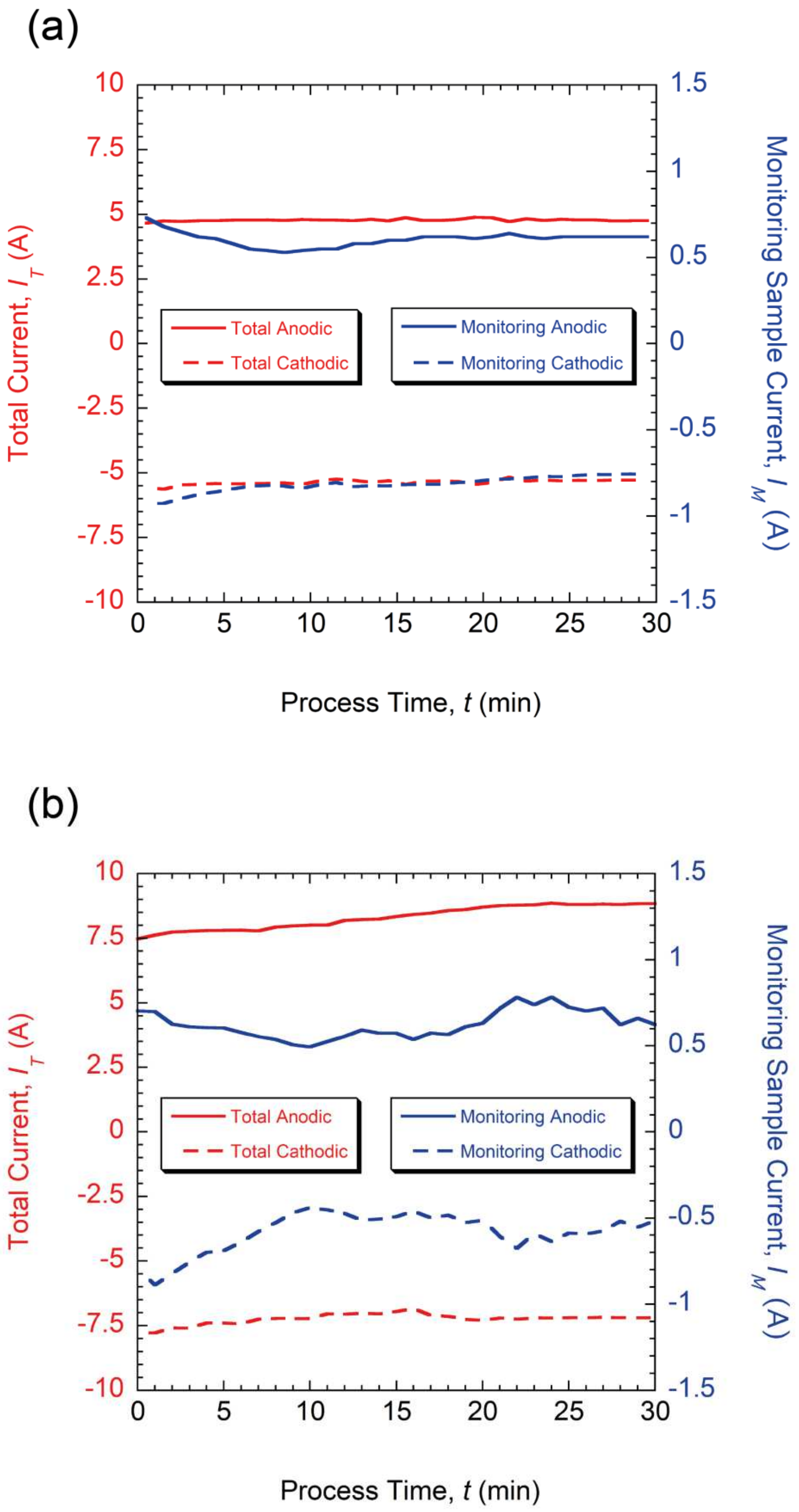

Figure 4.7 Total current and current flowing through the monitoring sample at (a) 50 Hz, and (b) 2,500 Hz. The total current at 50 Hz was set at a lower value than at 2,500 Hz to give similar currents through the monitoring sample.

In order to check whether the conditions experienced by the monitoring sample were similar to standard processing conditions, the applied voltage was compared. The data are shown in Figure 4.8, where it can be seen that the voltage follows a similar trend for standard samples and gas collection experiments. However, the voltage during gas collection experiments was systematically lower than under standard conditions by approximately 40 V at 50 Hz and slightly less at 2,500 Hz. The reasons for this are not completely clear, but it is likely to be due to the differences in sample geometry, or slight variations in electrolyte conductivity due to processing over several days. The mass gain of the monitoring sample was also compared to the standard plate samples. After 30 minutes of processing, the mass gain of standard samples, normalised for area, were 0.66 g dm^{-2} and 0.55 g dm^{-2} for 50 Hz and 2,500 Hz respectively. The monitoring samples had mass gains, normalised for area, of 0.63 g dm^{-2} and 0.68 g dm^{-2} for 50 Hz and 2,500 Hz respectively. There is relatively good agreement for the 50 Hz case (within 5 %), but the discrepancy is slightly larger at 2,500 Hz (around 20 %).

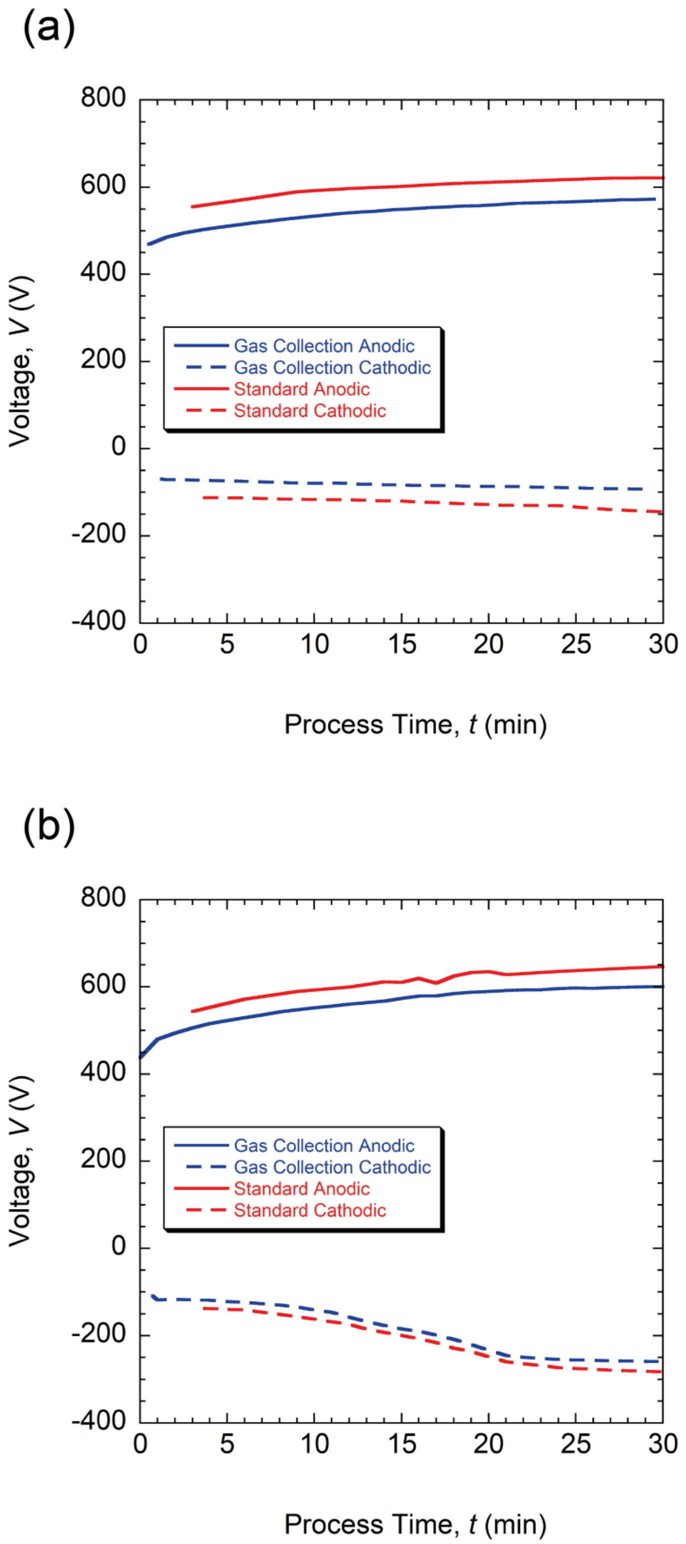

Figure 4.8 Comparison of the voltage during processing of standard plate samples, used for mass gain experiments, and the voltage during gas collection experiments for (a) 50 Hz, and (b) 2,500 Hz. The voltage follows a similar profile in both cases, although the gas collection experiments have a systematically lower voltage by ~40 V.

Chapter 5

Localised Discharge Cascades

The key to understanding the PEO process more fully lies in the detailed study of individual discharges. There has been significant progress in recent years from such studies, however, the picture is far from complete. Further improvements in the understanding of the mechanisms and processes occurring during an individual discharge, or sequence of discharges, has the potential for making informed improvements to PEO coating production process.

This work focuses on the study of individual discharges using high-speed photography of bulk samples, and high-speed photography, coupled with electrical monitoring, of small area samples. A study of the effects of discharges on the coating microstructure is made, and the sequence of events occurring during a discharge sequence is proposed.

5.1 Experimental details

In §5.2 coatings were grown on bulk samples of Al-6082, in the form of cylindrical bar, with diameter of 12.8 mm, mounted in resin. The 10 kW Keronite™ processing rig, with standard aluminium electrolyte was used to produce coatings. A constant capacitance condition was set to achieve a current density of 15 A dm^{-2} after the initial transitory regime.

Video sequences were captured at regular intervals during formation of PEO coatings, up to a thickness of around 60 μm. Each video sequence covered an interval of approximately 100 ms, and was captured at 180,000 frames per second, giving a time resolution of ~5.5 μs. The frame size was 128 × 128 pixels, with a linear spatial resolution of 12 μm per pixel, such that images covered an area of around 2.4 mm^2.

In §5.3 the small area electrical monitoring technique was employed to conduct further studies of discharge cascades. Coatings were grown on bulk samples of Al-2014, in the form 2 × 25 × 25 mm plates mounted in resin, connected in parallel with the exposed end of a small (0.88 mm diameter) wire of the same material. The 100 kW Keronite™ rig, with standard aluminium electrolyte, was used for processing samples. A frequency of either 50 Hz or 2,500 Hz was set, to investigate the effects of changing the AC supply frequency. A constant current condition was used, corresponding to a current density of 31 A dm^{-2}, for both anodic and cathodic polarities. Samples were processed for 30 minutes before experiments were started, generating an initial coating ~100 μm thick. Microstructural changes were assessed by SEM imaging of the small area sample before and after short PEO treatments.

The camera employed was a Phantom V12.1, with the acquisition rate set at 180,064 frames per second (5.12 μs exposure time). The linear spatial resolution was 13 μm per pixel. Typical images comprised 128 × 128 pixels, covering the entire small area sample (circle of diameter 0.88 mm).

Electrical data were collected with a sample interval of 480 ns, using the set-up shown in Figure 4.3(b). The wire was connected to a bulk substrate through a 50 Ω resistor and a reed relay switch, with the current determined from the voltage drop across the resistor, as shown in Figure 4.4. This created a current scale range of ±400 mA, which covered all of the profiles except for a few peaks during cathodic discharges.

5.2 Bulk sample characteristics

5.2.1 General characteristics

During examination of typical video footage, it became apparent that there is a strong tendency for discharge events (pulses of light emission) to occur in bursts, termed “cascades”. Cascades consisted of a sequence of light emission events, with an “incubation” period between them where no light emission can be seen. Importantly, these cascades were occurring in highly localised regions. Several authors have shown that discharge events only occur during anodic polarity in this set-up and that electrical discharge events are very well correlated to light emission events (see Figure 3.7). This is, however, the first set of experiments in which it has been confirmed that successive emissions occurred from the same location.

The location of a cascade can persist over several periods of the applied waveform. These observations are illustrated in Figure 5.1, showing information obtained from a PEO coating ~50 μm in thickness. Light intensity data in Figure 5.1 are obtained by summing all the pixel values, either for the entire frame (128 × 128 pixels), or just from the region indicated by the white circle in Figure 5.1(b), with successive frames corresponding to time data. Figure 5.1(b) shows the superimposition of the complete video sequence (~17,500 images), which was produced by summing the pixel values of each image in the sequence. Clearly, during the period concerned (~100 ms), a series of discharges occurred at a particular location and, at least in this case, nowhere else in the field of view—this is confirmed by comparing Figure 5.1(a) and (c), which shows all the light intensity peaks came from the localised region indicated in Figure 5.1(b).

Camera recording were made periodically as the coating thickness increased, each ~100 ms long, but often did not show any discharges, highlighting the stochastic nature of discharge events. The discharges apparently occurred only when the (anodic) applied potential was sufficiently high. This is illustrated by Figure 5.1(d), which shows a higher resolution plot of the light intensity and a typical voltage profile for the anodic half cycle superimposed. Discharge durations were between 100 and 300 µs, separated by incubation periods of about 500–1,000 µs. This is broadly consistent with previous observations, see §3.2.1. It certainly seems likely in view of these observations that "cascades" of this type, with these characteristic features, commonly occur at discrete locations.

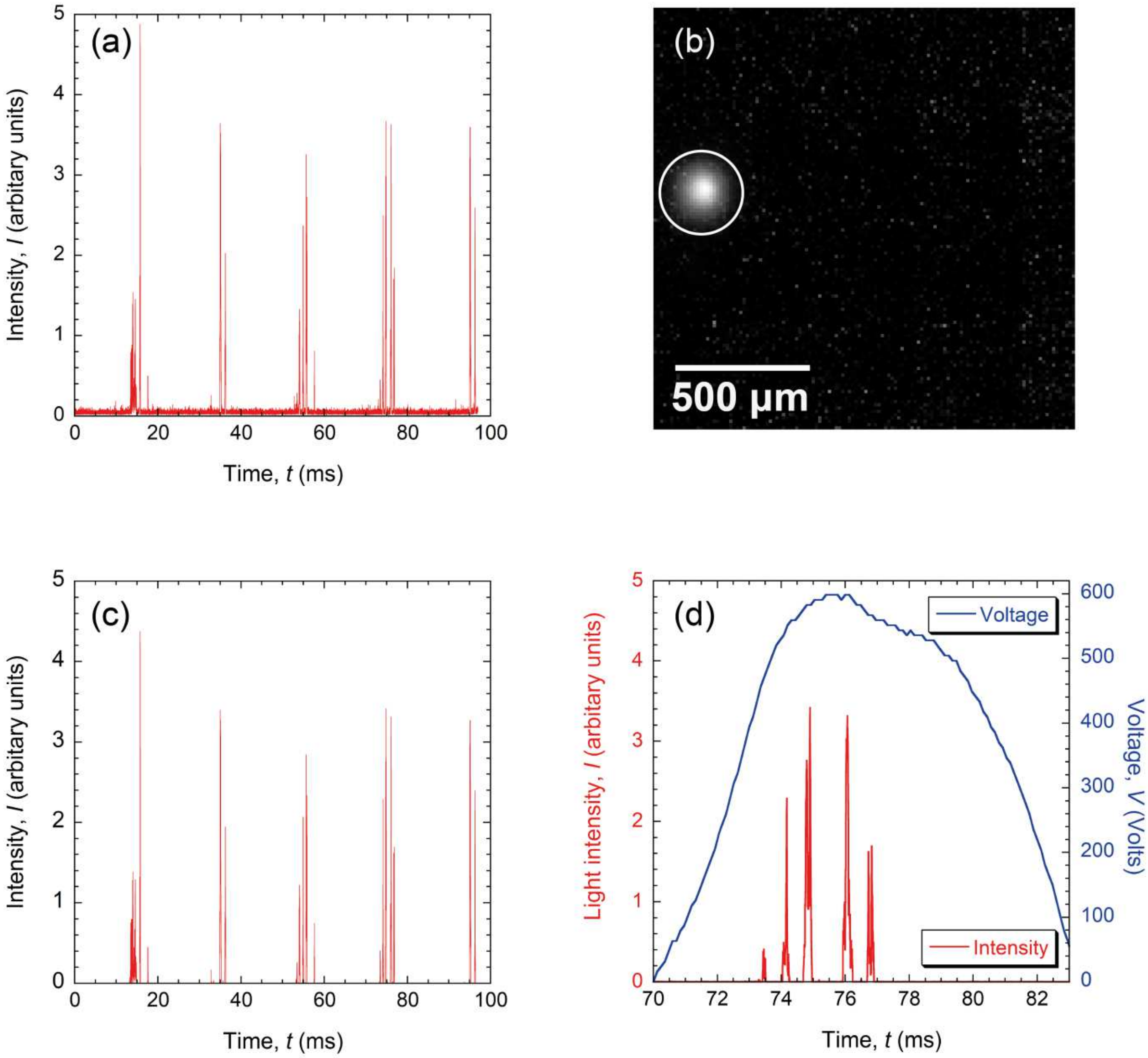

Figure 5.1. Information relating to a sequence of 17,500 images (exposure time ~5.5 µs, pixel side length 12 µm) from a PEO coating ~50 µm in thickness, showing, (a) total summed light intensity for each frame, as a function of time, (b) a superimposition of the complete sequence of images, (c) as for (a) but taken only from the bright area (circle of 288 µm diameter) in (b),and (d) higher resolution plot of part of (c), approximately covering an anodic half-cycle, with a typical measured voltage profile [47] during such a period superimposed.

5.2.2 Effect of coating thickness

The cascade behaviour described above was observed throughout the experiment, although there were certain systematic differences between thin (~5 μm) and thick (~50 μm) coatings. Figure 5.2 illustrates these differences, which shows information obtained from a thin (~5 μm) coating, corresponding to the information shown in Figure 5.1 for a thick (~50 μm) coating. It can be seen that, with such a thin coating, discharges occurred in several, in this case four, locations within the viewed area, during the period concerned (~100 ms). As with the thicker coating, they were confined to the periods during which the applied anodic potential was sufficiently high. It seems that discharges can take place simultaneously in different nearby locations (Figure 5.2(d)) although it might be inferred that this becomes unlikely if they are very close. For example, discharges in location 4 appear to have been largely suppressed by being close to the well-established cascade taking place in location 1. This may be related to the charge distribution and equi-potential contours in the vicinity of a discharge. It is perhaps worth noting that the three well-established cascades in Figure 5.2(b) are all about 1 mm apart. Of course, this cannot be regarded as statistically significant, and in any event the area from which charge may be flowing into a discharge probably becomes larger as the coating becomes thicker, but it may nevertheless be potentially of interest.

It is also clear that the individual discharges are more frequent and less intense when the coating is thinner. This is a feature that is well established for PEO and, indeed, is often apparent to the naked eye, although evidently it is not in fact discrete discharge events that are being observed in that case. A further impression of the differences between discharge sequences taking place through thin and thick coatings can be obtained from Figure 5.3. These two plots show perspective visualisations (with the contrast reversed and the transparency set so that low value pixels were transparent and high value pixel were opaque), for thin and thick coatings, of a portion of the complete stack of frames, covering a time period of about 8 ms (i.e. 1,500 frames). In both cases, this captures part of a cascade (two for the thinner coating) occurring during an anodic half-cycle. This confirms the strong tendency towards spatial localisation of individual cascades and also conveys an impression of the partially stochastic nature of these events.

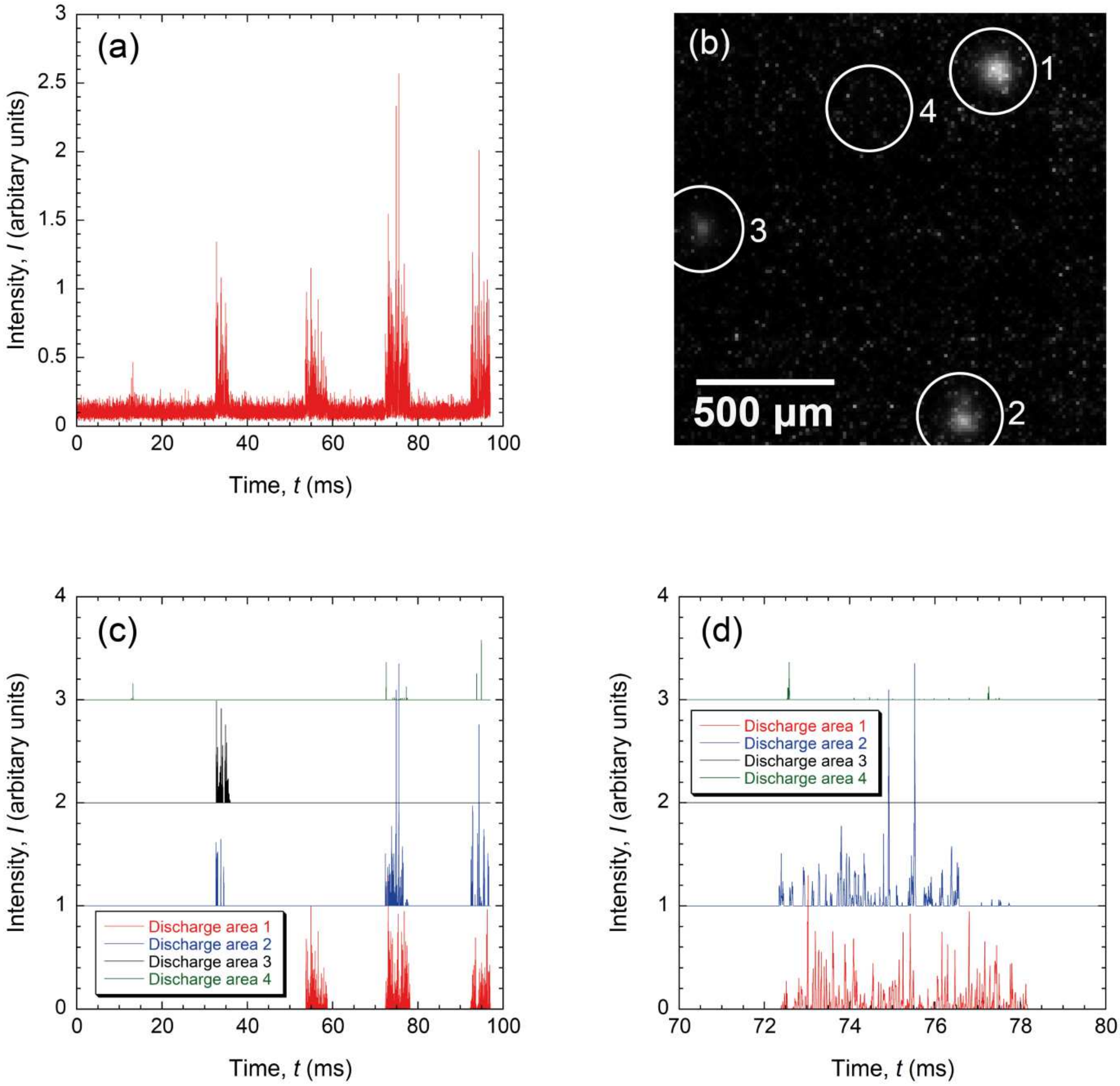

Figure 5.2 Corresponding information to that of Figure 5.1 from a PEO coating ~5 µm in thickness, showing (a) total summed light intensity for each frame, as a function of time, (b) a superimposition of the complete sequence of images, (c) plots of summed intensity against time for light from the 4 circles (288 µm in diameter) shown in (b), and (d) higher resolution plot of part of (b).

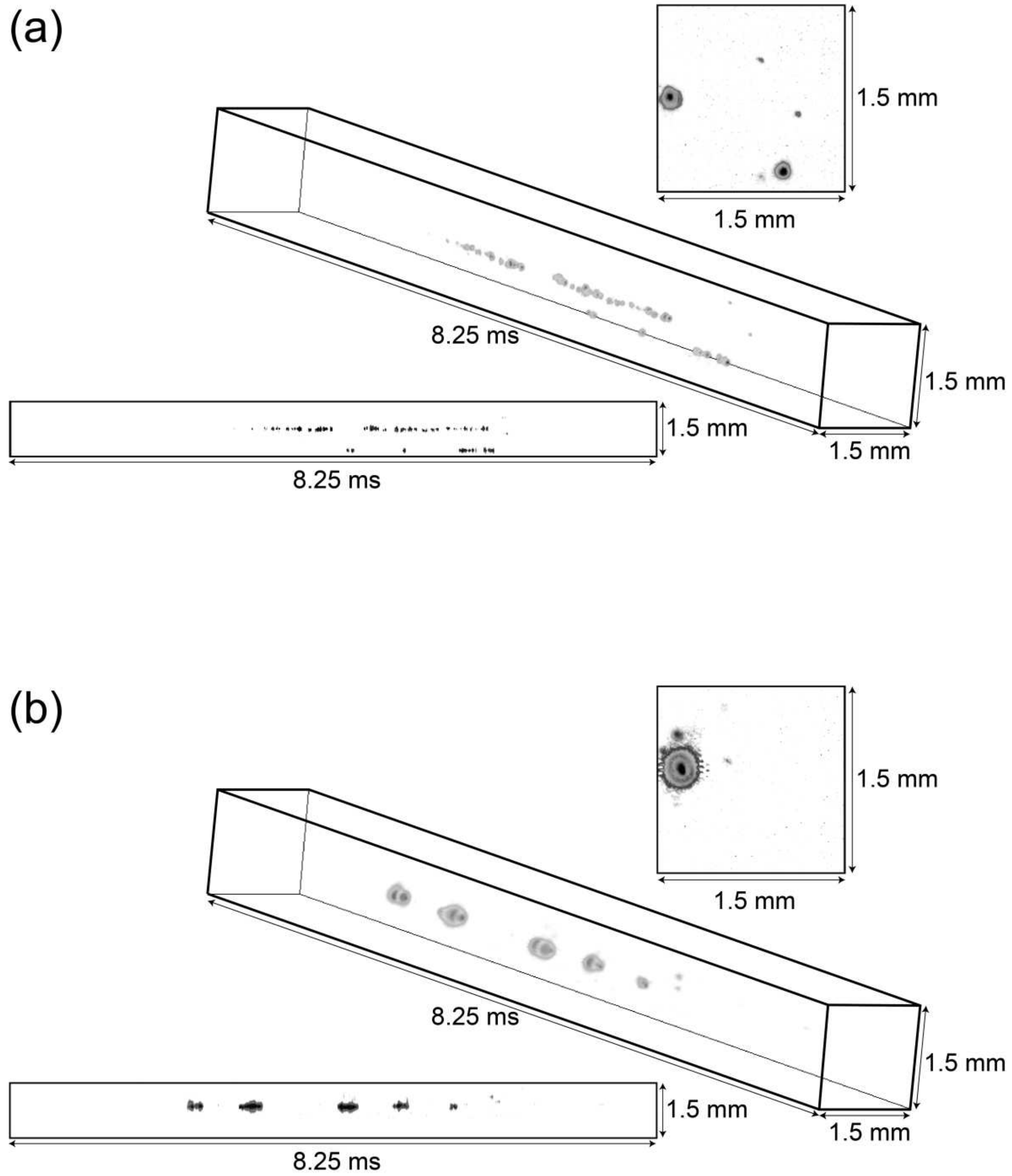

Figure 5.3 3-D perspective and 2-D projection views of a stack of images (with reversed contrast), representing periods of 8.25 ms duration, for coatings with approximate thicknesses of (a) 5 μm and (b) 50 μm.

The experimental outcomes described above do provide clear confirmation that discharges exhibit a strong tendency to occur in cascades, which take place in localised regions. The spatial resolution of these videos is not very high, but it is sufficient to be confident that successive discharges initiate and develop in locations that are favourable (constitute low electrical resistance paths) because of microstructural changes that arose there during previous discharges.

The apparent size of discharges can be estimated from the video images. However, this does not give an accurate measurement of the discharge plasma size due to light scattering, and the sensitivity of the camera CCD array, but does provide a semi-quantitative comparison. The region from which light is emitted during a cascade appears to be of the order of several tens of μm in diameter, although there is evidence that it is smaller for thinner coatings than for thicker ones, see Figure 5.3. This appears to be a consequence of the discharges themselves being larger (more energetic and longer-lived) with a thicker coating, rather than the location drifting around more in that case. These images suggest that each discharge in a cascade occurs at exactly the same location as previous ones in the sequence, at least within the available resolution. It is not surprising that the thickness of the coating has an effect on the details of how these discharges and cascades take place, but it seems likely that the sequence of events is similar across a wide range of thickness.

5.3 Small area sample investigation

5.3.1 Electrical characteristics at low and high frequency

Typical variations of voltage and small area current are shown in Figure 5.4 for (a) 50 Hz and (b) 2,500 Hz. It can be seen in Figure 5.4(a) that 7 discharges occurred during this anodic half-cycle (10 ms period) at 50 Hz. The anodic voltage developed was about 600 V. The average current during this cycle was about 20 mA. During the 1 s treatment period, discharges occurred only during the latter part, such that the average anodic current over the whole period was about half this value. The average current during the cathodic half-cycles tended to be more homogeneous and was also ~10 mA, although the voltage needed to create this was only ~150 V. Converted to a current density, using the nominal surface area of the wire, a current of 10 mA corresponds to about 200 A dm^{-2}, which is larger by a factor of about 6 than the pre-set value, which flows through the main part of the sample. This difference is partly attributed to the convergent nature of the electric field in the vicinity of the small area sample (analogous to the "corner effect" often observed with bulk samples) and also to some coating production on the cylindrical surface of the wire exposed by the small interfacial gap between it and the surrounding resin. It should also be noted that the period of 1 s is rather short for the discharge characteristics on the small area sample to be expected to conform to overall average behaviour. Typical peak discharge currents were ~100 mA and discharge lifetimes were ~300 μs. These values are consistent with previous reports [47, 74, 77].

With the higher frequency supply (Figure 5.4(b)), the average current was similar to that at 50 Hz (~10 mA), in both anodic and cathodic half-cycles, but there was sufficient time for only a single discharge in an individual anodic half cycle and these occurred in only a relatively small proportion of them. The voltage created during the anodic half cycles was similar to that with the lower frequency (~600 V), but in the cathodic half-cycles it was larger (~300 V, compared with 150 V), suggesting that a larger driving force is required to maintain the set current density when the frequency is high. Typical periods between (anodic) discharges were about 5 ms, corresponding to about 12 cycles. The peak current in a discharge (~100 mA) was similar to the low frequency case. Discharge lifetimes commonly covered the whole half-cycle period (200 μs), suggesting that they were being cut slightly short as the voltage switched to cathodic.

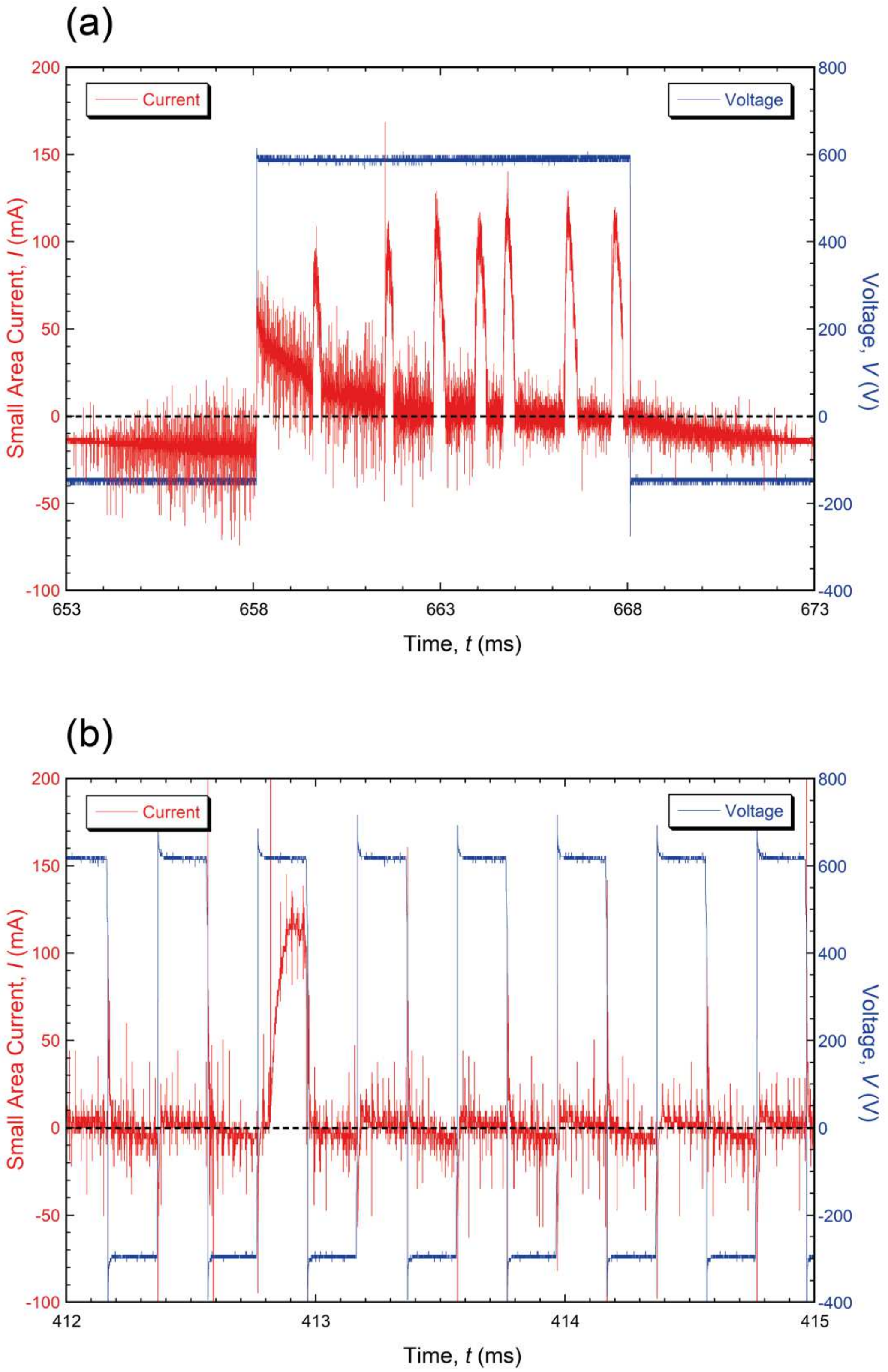

Figure 5.4 Synchronised plots of (small area) current and voltage during representative periods for supply frequencies of (a) 50 Hz and (b) 2,500 Hz.

It was also noticeable that, with the high frequency supply, discharges sometimes occurred during the cathodic part of the cycle. This is illustrated in Figure 5.5, where it can be seen that they commonly, but not invariably, followed an anodic half-cycle in which a discharge had occurred. It can also be seen that, while the discharge lifetime was usually the half-cycle period (200 μs), the peak current (~300-400 mA) was significantly larger than that during anodic discharges (~100 mA). They do take place with a lower voltage (~300 V, as opposed to 600 V for anodic discharges), but the levels of energy, as well as the amount of charge transferred, do therefore appear to be somewhat greater for cathodic discharges. The cathodic discharges were less common than the anodic ones, but, as can be seen in Figure 5.5, they tended to occur in clusters. It seems possible that oxidation could take place during cathodic discharges in a similar way to that in anodic ones, since both presumably allow exposure of metal from the substrate to oxidizing agents in the plasma channel.

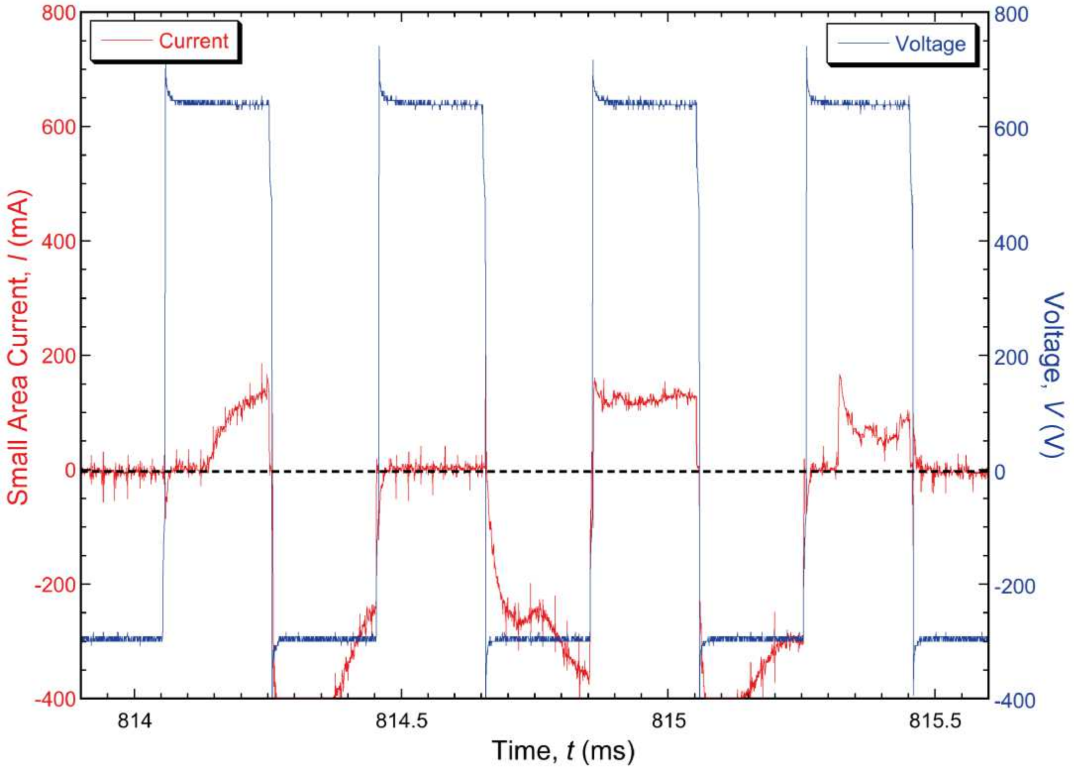

Figure 5.5 Synchronised plots of (small area) current and voltage during PEO processing at 2,500 Hz, showing a set of cathodic discharges.

5.3.2 Microstructural evolution during a cascade

On comparing SEM micrographs before and after the short duration (1 s) PEO treatments, it was immediately apparent that changes had occurred in one region only, despite the fact that many discharges had been generated during this period. This is further strong evidence for the localization of cascades, and suggests that they can persist in a given location for considerably extended periods (during which hundreds of discharges occur). An example can be seen in Figure 5.6, which shows micrographs taken before and after a PEO treatment at 50 Hz, lasting for 1 s. Discharges occurred only during the last 0.6 s of this period (through about 30 cycles), with a total of about 250 discharges (about 8 in each anodic half-cycle) during this treatment. These discharges all occurred in the upper central region of the sample, as oriented in Figure 5.6. Evidence for this is presented in Figure 5.7, which shows a single video frame (from an anodic half-cycle) and the complete set of superimposed frames (180,000 frames, each with ~5 μs exposure time) over the 1 s period. It can be seen that significant light emission occurred only in the two adjacent locations in Figure 5.6(d) where the microstructure had changed. It should be appreciated that relatively large gas bubbles normally form at the top of plasma channels in such coatings, blurring the sharpness of the light emission in images of this type, which is investigated in §6.3.

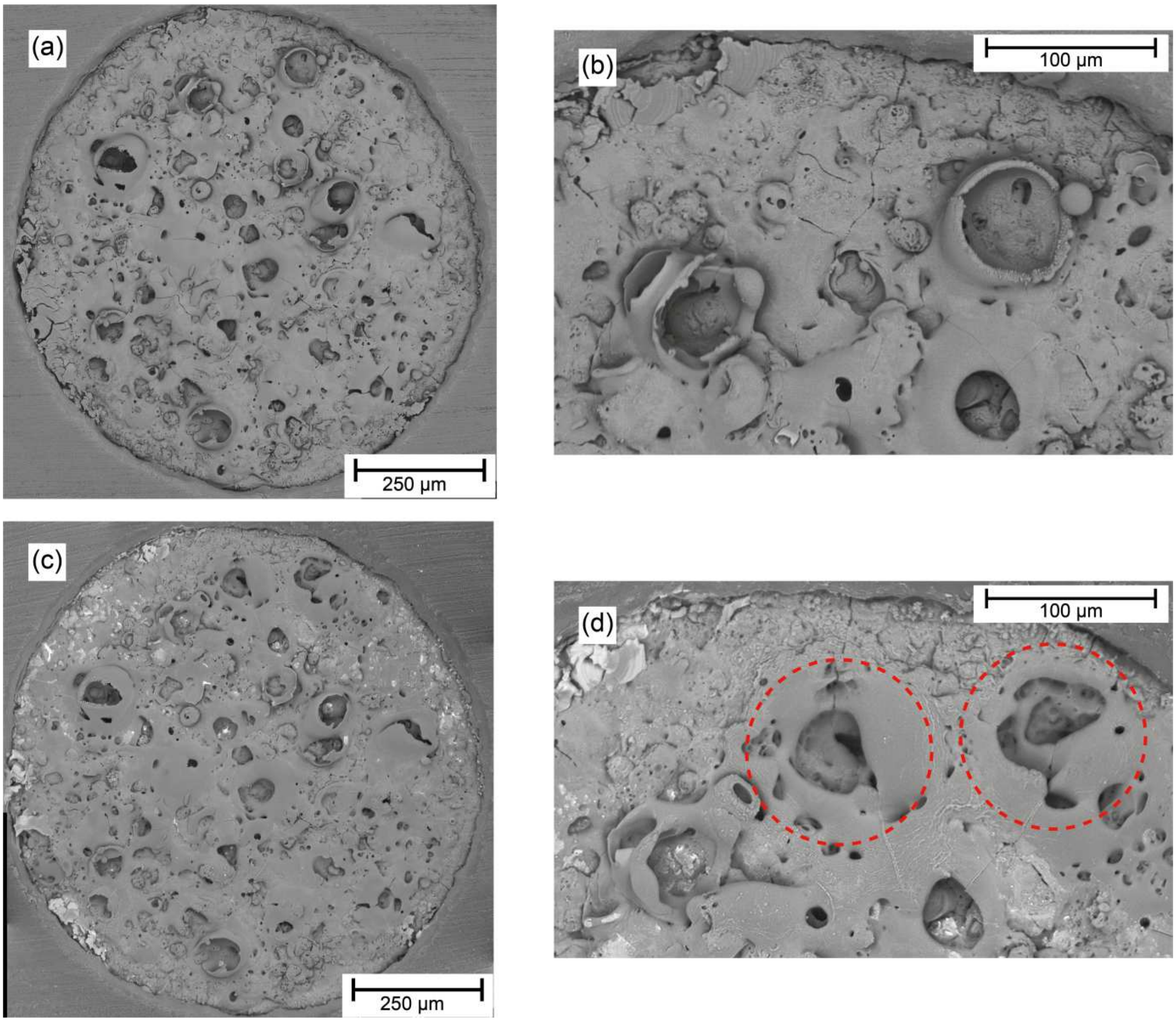

Figure 5.6 SEM micrographs of a small area sample, with 100 µm PEO coating, showing (a) complete surface in initial state, (b) magnified top central region, (c) complete surface after further PEO processing at 50 Hz for 1 s and (d) magnified top central region after the 1 s treatment (with the regions in which the discharges were localised indicated by circles).

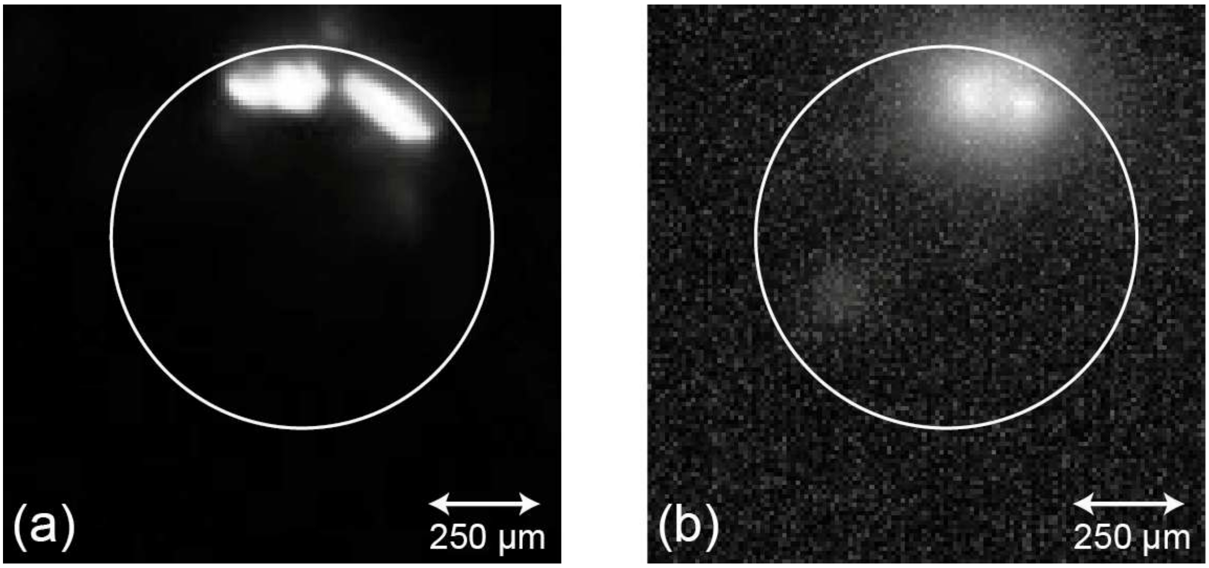

Figure 5.7 Video images of the small area sample taken during the 1 s PEO treatment at 50 Hz (in the same orientation as Figure 5.6), showing (a) a typical single frame and (b) the complete set of (~180,000) superimposed frames. The white circles show the approximate location of the sample boundary.

Comparing the whole small area sample before and after the 1s PEO treatment (Figure 5.6(a) and Figure 5.6(c)) it can be seen that the only location in which the microstructure differed significantly was the upper central area shown at higher magnification in Figure 5.6(b) and Figure 5.6(d). As can be seen in these two micrographs, changes were induced by the repeated discharges in the central part of this field of view, particularly in the two regions indicated by the dotted circles. It does appear in this case that microstructural changes at the surface, and associated emission of light, were centred on two locations about 200 μm apart, and the affected regions were approximately circular, with diameters of the order of 100–150 μm. Emissions often occurred simultaneously from both locations (see Figure 5.7(a)), although there were also instances in which one or the other dominated. It seems likely that they were both associated with the same discharge events, probably with the same point of origin at the interface between coating and substrate, but different paths to the surface. As suggested in §5.2.2, independent simultaneous discharge cascades are unlikely to be located much closer than about 1 mm apart and this is in line with broad expectations concerning the nature of associated electric fields and charge redistribution effects. It may be that such a bifurcation of discharge paths to the surface is relatively rare, although these observations confirm that it can happen.

It has been estimated (see §6.5) that a typical discharge energy is ~1 mJ under the conditions used in the present work and that the conversion rate between discharge energy and resultant volume of coating is typically ~10^{13} J m^{-3} (10^{-5} J μm^{-3}). These are highly approximate figures, but it follows that, during the 1 s PEO treatment, with ~300 localised discharges occurring on the small area sample, about 0.3 J of energy was absorbed there, creating ($0.3/10^{-5}$) ~3×10^4 μm^3 of oxide. This corresponds to a cube of side ~30 µm, or, on a cylinder of diameter 100 µm, an increase in length of about 4 µm. Of course, much of this oxide was probably created near the interface with the substrate and a relatively small proportion ejected through the discharge channel onto the free surface. It is also possible that molten oxide is injected under the pressure of the discharge into neighbouring inter-connected pores, see §5.3.5 below. In any event, what is being observed in Figure 5.6(b) and (d) appears to be at least broadly consistent with these expectations about the quantities of oxide involved.

5.3.3 *Effect of interruption of a discharge cascade*

Presented in Figure 5.8 is the outcome of the experiment in which the sample was subjected to a second PEO treatment of duration 1 s (at 50 Hz), after having been removed once and examined in the SEM. This is an analogous set of micrographs to that in Figure 5.6 and it can be seen that similar effects were observed, with a change in the surface appearance again having been created only in the upper central part of the section. (Figure 5.8(a) and (b) are thus the same images as Figure 5.6(c) and (d), and are reproduced here for ease of comparison.) The associated video information was also similar to that shown in Figure 5.7. It is clear from these observations that it is the residual microstructure, probably primarily the presence of pore channels, that predisposes a cascade of discharges to persist in the same location, rather than anything connected with residual thermal or electrical fields. It may also be noted that the total number of discharges in the cascade that extended through these two 1 s treatments was about 700. The maximum number of discharges in a cascade cannot really be estimated from the information here, although it seems likely that the figure might be of the order of at least 1,000, since the cascade had not terminated when the treatment was stopped. The most likely feature responsible for this behaviour is clearly a large, deep pore, or pore network, which, when re-filled with electrolyte, provides a path of low electrical resistance.

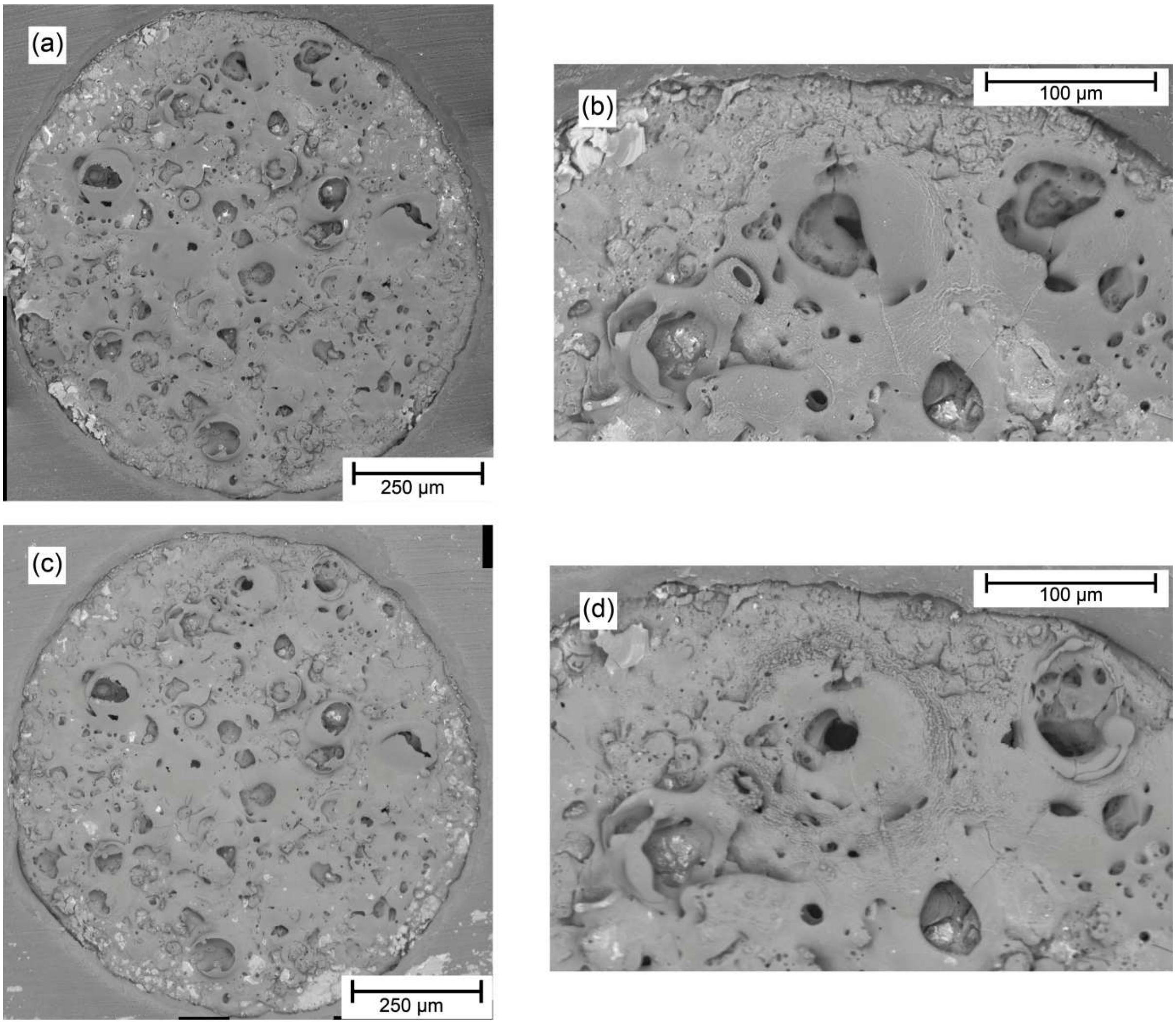

Figure 5.8 SEM micrographs of a small area sample, with 100 µm PEO coating, showing (a) complete surface in the initial state (after one 1 s treatment), (b) magnified region where the cascade occurred, (c) complete surface after a second 1 s PEO treatment at 50 Hz and (d) the same region after PEO processing at 50 Hz for a further period of 1 s.

5.3.4 Microstructural evolution with high frequency supply

The same operations were carried out (on a different sample), with a frequency of 2,500 Hz. The outcomes are shown in Figure 5.9. In this case also, a discharge cascade occurred, localised in one place and extending over the treatment period of 1 s. The discharges were fairly uniformly distributed in time, with the total number during the period being about 150 (so that they occurred approximately once every 15 cycles, at intervals of about 6 ms). In this case, there was just one channel reaching the surface, and indeed it may well be relatively unusual for two nearby channels to be created as part of a single discharge cascade, as was observed in the 50 Hz case.

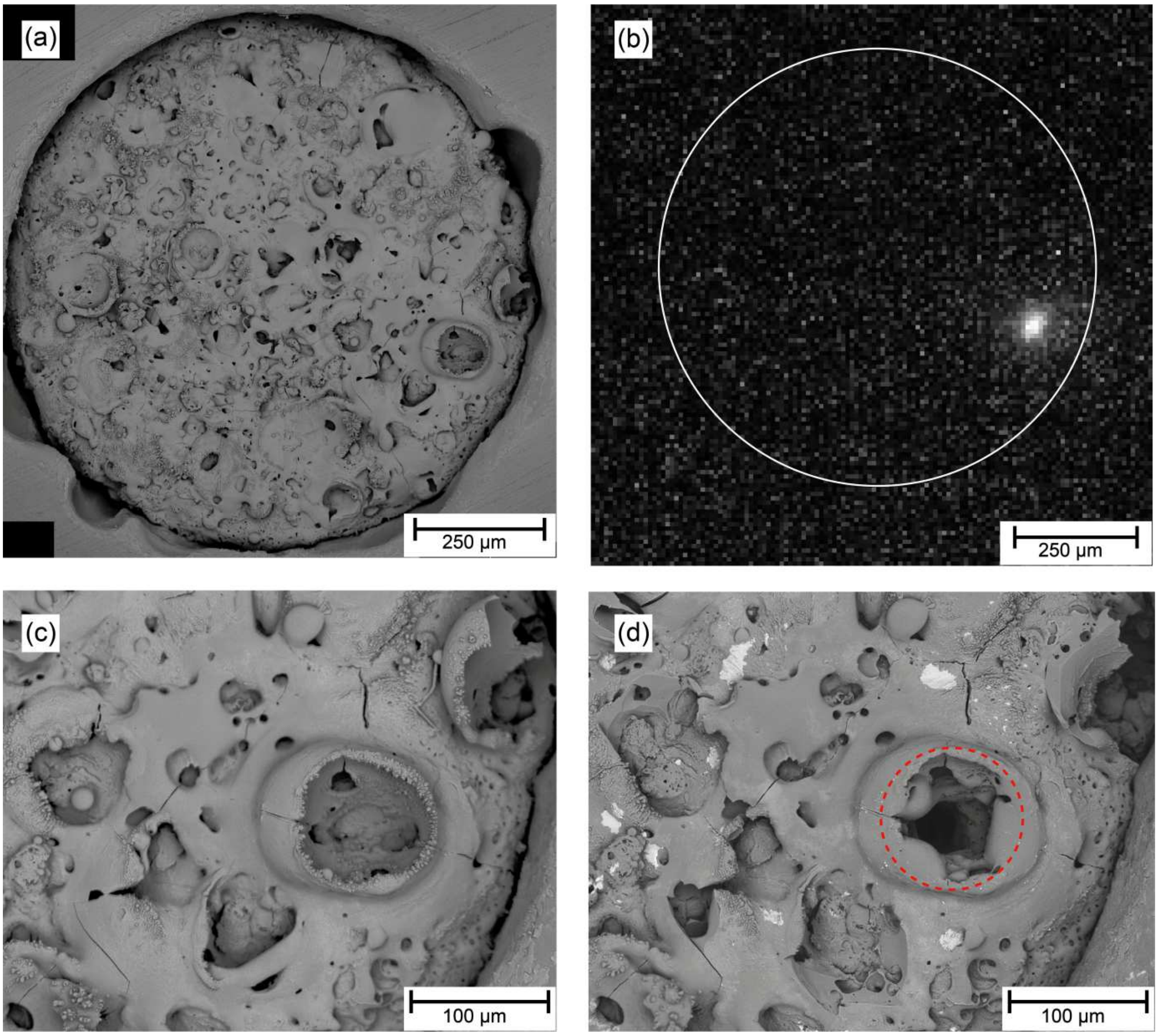

Figure 5.9 Microstructural effects of a discharge cascade on a small area sample (with 100 μm PEO coating) at 2,500 Hz for 1 s, showing (a) SEM micrograph of the surface in the initial state, (b) superimposed set of (~200,000) video images taken during the process, (c) magnified SEM of the region indicated in (b) as the cascade location and (d) the same area after PEO processing (with the region in which the discharges were localised indicated by circles).

A significant difference, however, between outcomes with the low and high frequency supplies was the occurrence in the latter case of discharges during cathodic half-cycles, although they formed only sporadically. Figure 5.10 shows a set of 6 images, each created by superimposing the 36 video frames that cover a half-cycle (200 μs) in the set for which the electrical data are shown in Figure 5.5. Alternate images in this sequence thus cover anodic and cathodic half-cycles, starting with an anodic one. It can be seen that the half-cycles for which significant current flow took place (i.e. discharges occurred) correspond to ones in which there was light emission (i.e. all except the third one in this series). It is also clear that all of the discharges took place in the same location—the one shown in Figure 5.9. Also apparent is that the cathodic discharges (second, fourth and sixth in this series) involved stronger light emission than the anodic ones. This is consistent with the associated currents (in Figure 5.5) being significantly greater for the cathodic discharges.

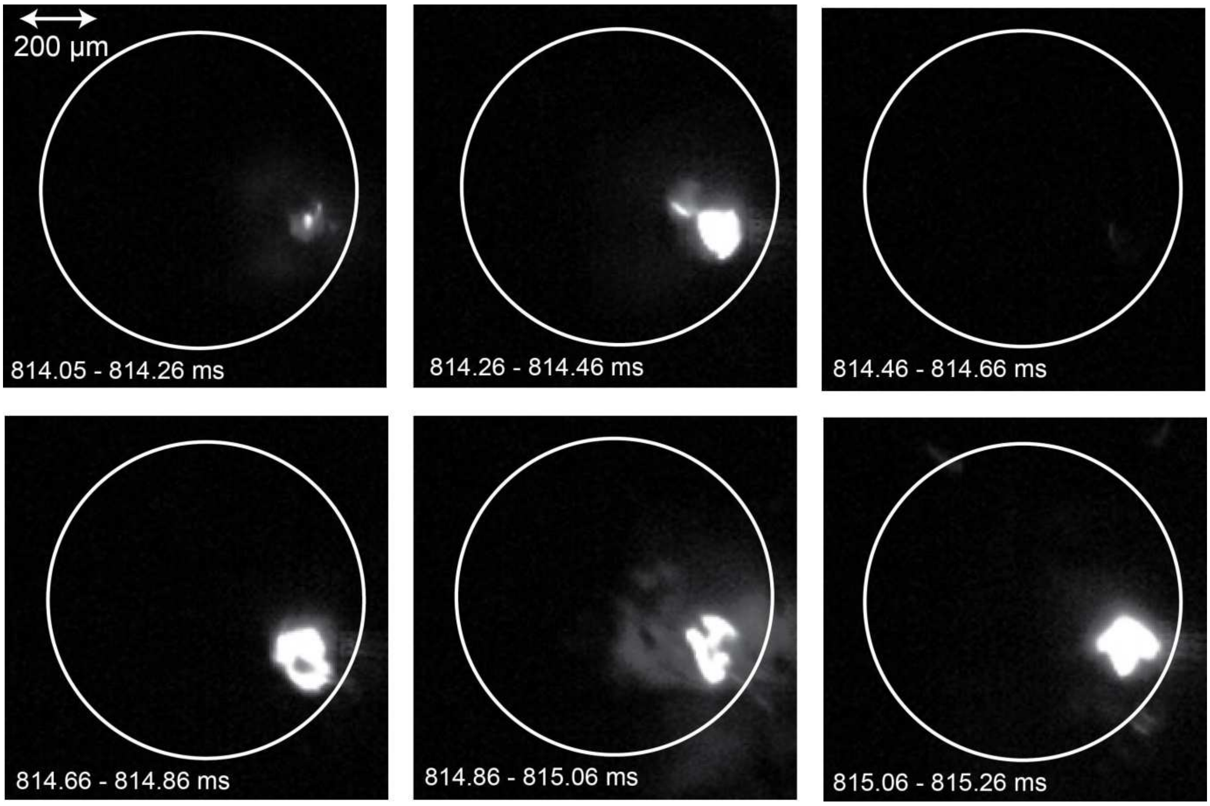

Figure 5.10 Sequence of superimposed sets of video images (each made up of 36 separate images, covering one of the 6 half-cycle periods shown in Figure 5.5), during PEO processing at 2.5 kHz.

Of course, since there were relatively few cathodic discharges during the experiments carried out here, and they occurred in the same locations as anodic ones in the cascade concerned, it is not possible to draw any firm conclusions about the microstructural changes they induced. It seems likely, however, that they could also promote at least some oxidation of the substrate.

5.3.5 Discharge channel architecture

An impression of the 3-D pore architecture of a discharge channel, formed during the experiment in §5.3.4, can be obtained from Figure 5.11. A perspective view down into the channel is shown, followed by a series of transverse sections. The appearance is broadly consistent with recent work [79, 84] showing tomographic data from PEO coatings. It can be seen that, while the architecture is naturally rather irregular, the main pore does penetrate down close (a few μm) to the substrate, although it does taper slightly in diameter with increasing depth. It is a few tens of microns in diameter near the bottom, while the region of the "volcanic crater" at the top has a diameter of ~100 μm. The surrounding region at the top of the channel may be largely formed of oxide ejected from it during the cascade. It is possible that the "incubation period" between the individual discharges in a cascade (usually of the order of several hundred μs) represents the time needed for electrolyte to fill the (evacuated) channel left after the plasma in it has collapsed.

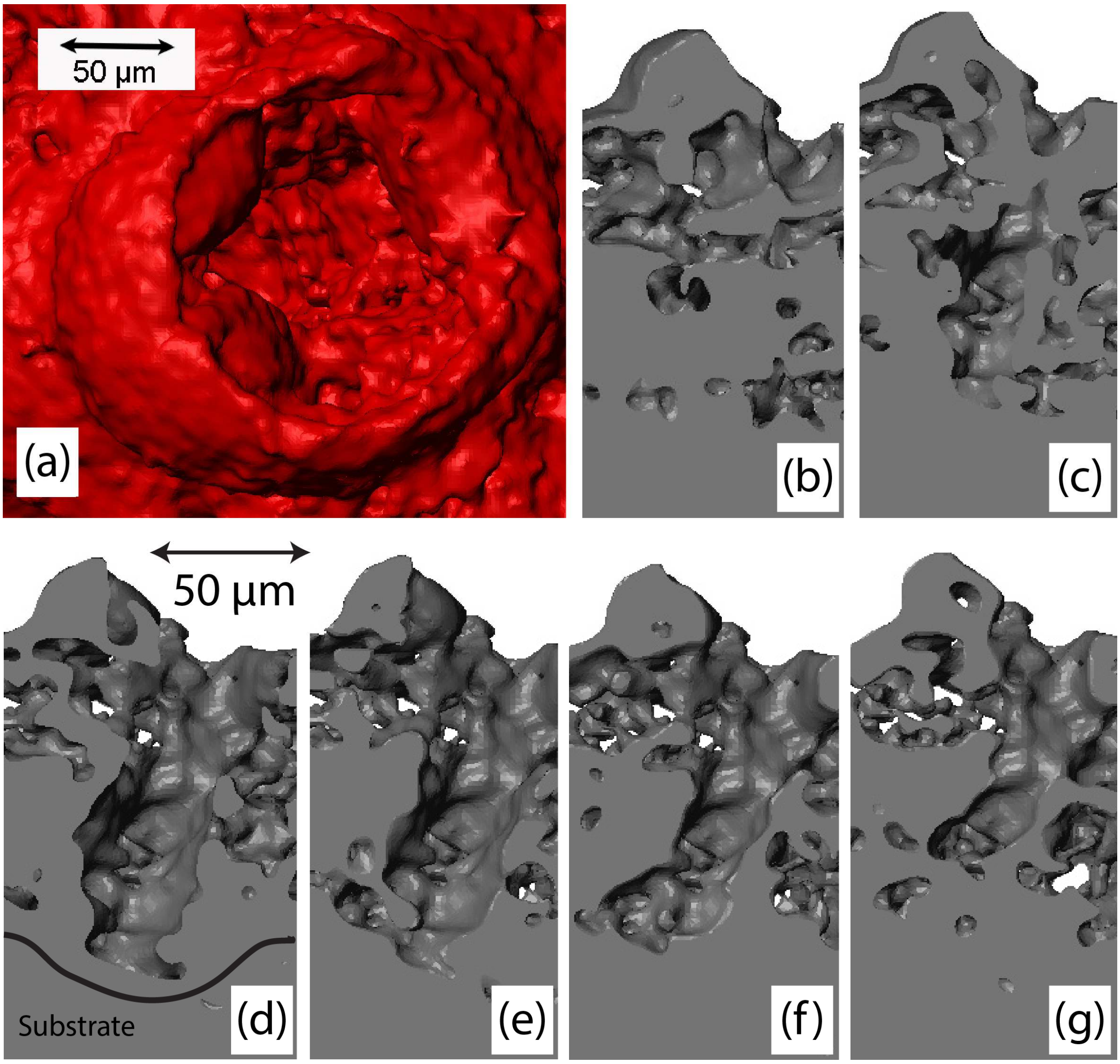

Figure 5.11 Tomographic data from the region of the small area sample in Figure 5.9 (d), showing (a) a perspective view into the pore channel and (b)–(g) progressive parallel sections (11 µm apart), containing the through-thickness direction, with sections (d) and (e) located near to the approximate axis of the pore.

Porosity in PEO coatings does tend to be inter-connected and while they are certainly quite porous (typically ~15–20% [83]), they do not normally contain many very large diameter pores of the type seen here (at least in Al-based samples). The reason for this is presumably that they tend to become filled, or to collapse, when new discharges occur in the vicinity. It seems likely that molten oxide can be expelled from an active discharge channel, not only to the free surface (creating "volcanic craters"), but also into nearby residual pores from earlier cascades. In this way, the only large diameter through-thickness pores present in a PEO coating (of the type shown in Figure 5.11) are likely to be those created by the most recent discharge cascades.

5.4 Summary

It is confirmed that the discharges occurring during PEO tend to occur in sequences ("cascades"), with lifetimes from a few microseconds to several tens of microseconds and "incubation" periods between them from tens to hundreds of microseconds. Cascades can extend over several cycles of the applied potential, and only occur during the anodic half-cycle under standard conditions. These have been observed to comprise at least several hundred individual discharges and it seems likely that this number could commonly run into thousands (especially for thick coatings). A particular cascade occurs in a well-defined physical location, with successive light emission events having similar radii and being centred on the same point (within the linear resolution of the images used here). As the coating thickness increases, most of these characteristics remain qualitatively unaltered, but there is a tendency for the light emission to have a larger radius and greater intensity with thicker coatings. Discharge lifetimes, and incubation periods, also tend to increase as the thickness is raised.

From microstructural observations of the changes induced by individual cascades on the free surface, the affected regions are approximately circular. With an initial PEO coating (~100 μm thick), the diameters of the affected regions are of the order of 100 μm. Using estimates of the aggregate discharge energy involved in a cascade of, say, 1,000 discharges, and the relationship between this and the volume of oxide created, the associated increase in the average thickness of this circular area is ~5 μm. Discharges within a cascade continue at the same location, even if the PEO process is interrupted, the sample removed, dried, and replaced in the electrolyte and the process restarted. This strongly suggests that it is residual microstructural features, particularly the pore channels, that are ensuring that the cascade persists in the same location, rather than short term effects such as residual thermal or electrical fields. A picture now emerges of the complete cycle of events during a discharge within a cascade sequence. This is illustrated in Figure 5.12, which shows a series of schematic sections (based on the pore architecture in one of the tomographic sections in Figure 5.11). The factors that control the timing of the sequence can be identified in these schematics. For example, the incubation period probably represents the time required for the electrolyte to flow back into the pore. This will tend to become longer as the coating thickness increases. The substrate is progressively consumed at the site of the discharge (by evaporation into the plasma) and oxide is progressively formed in the vicinity. The region of consumption of the substrate at the bottom of the pore channel extends down several microns, relative to the surrounding area. Since the oxide normally occupies a larger volume than the metal from which it formed (partly due to porosity in the oxide), the interface moves downward relative to the original position of the metal surface, while the free surface moves upwards. The lifetime of a cascade is presumably terminated when enough oxide has been formed in the location concerned to raise its resistance above that of alternative nearby sites.

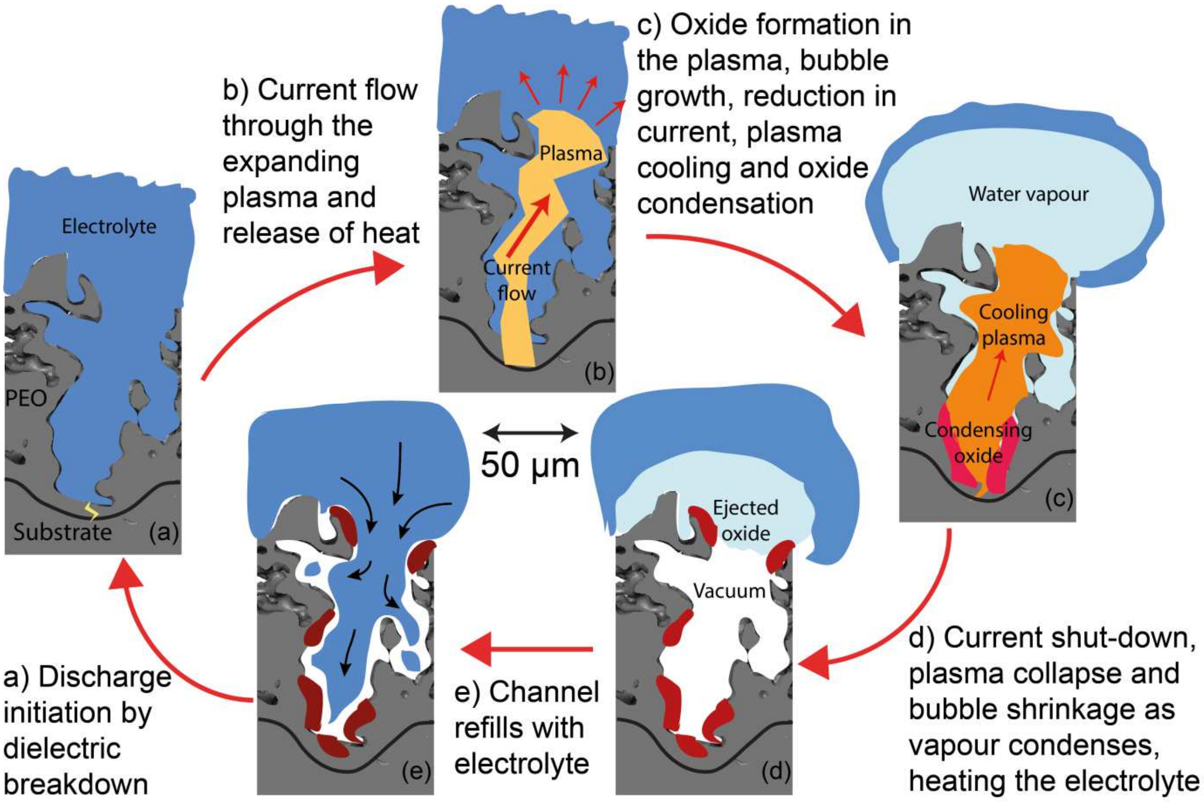

Figure 5.12 Sequence of schematic sections through a pore during the cycle of a single discharge event in a PEO cascade.

A high frequency supply, with the half-cycle period approaching typical discharge lifetimes, creates discharges at similar overall intervals to the low frequency case, also in spatially-localised cascades and inducing similar microstructural changes. It has also been observed that high frequency leads to discharges occurring during the cathodic half-cycle, as well as the anodic one. Furthermore, these cathodic discharges are more energetic than the anodic ones, and can occur in the same locations as the anodic ones.

Chapter 6

Energetics of Individual Discharges

One of the factors limiting more widespread use of PEO coatings is the high energy consumption associated with the process. In principle, oxidation of the metal substrate is thermodynamically favourable so should release energy rather than consume it. Therefore, a detailed study of the processes involved during PEO, and particularly during individual discharges, is needed to understand where and why large quantities of (electrical) energy are consumed during PEO processing.

The present work applies techniques, previously discussed, to study individual discharges using synchronised high-speed video and electrical monitoring, with external illumination. The results of this allow a semi-quantitative energy audit to be carried out to establish the main sources of energy consumption.

6.1 Experimental details

Coatings were grown on bulk samples of Al-6082, in the form 25.4 mm square section bars mounted in resin, with the exposed end of a small (1 mm diameter) wire of the same material. The 100 kW machine was used with a frequency of 50 Hz and a current density of 31 A dm^{-2}, for both anodic and cathodic polarities. A coating of thickness ~5 μm was created (by running the process for about 3 minutes) before the measurements were started.

The camera employed was a Photron FastcamSA 1.1, with the acquisition rate set at 125,000 frames per second (8 μs exposure time). The linear spatial resolution was 9 μm. Typical images comprised 192 × 144 pixels, covering an area of 2.24 mm^2, which was large enough to view the entire cross section of the small area (1 mm diameter) wire. This was synchronised with electrical measurements using the set-up shown in Figure 4.3(a), and had a sampling interval of 102.4 ns.

6.2 Electrical characteristics of individual discharges

A typical current-time relationship after initiation is shown in Figure 6.1. It can be seen that, after an initial peak in current (on switching to the anodic half-cycle), current pulses start to form after around 200 μs, representing individual discharges. As was observed from light emissions in §5.1 under similar conditions (on a bulk sample), discharge durations were around 20–100 μs (depending on coating thickness and current density) and periods between them were of the order of tens to several hundred μs (all occurring in cascades at particular locations). The discharge indicated in the figure is the one selected for synchronous study of video images.

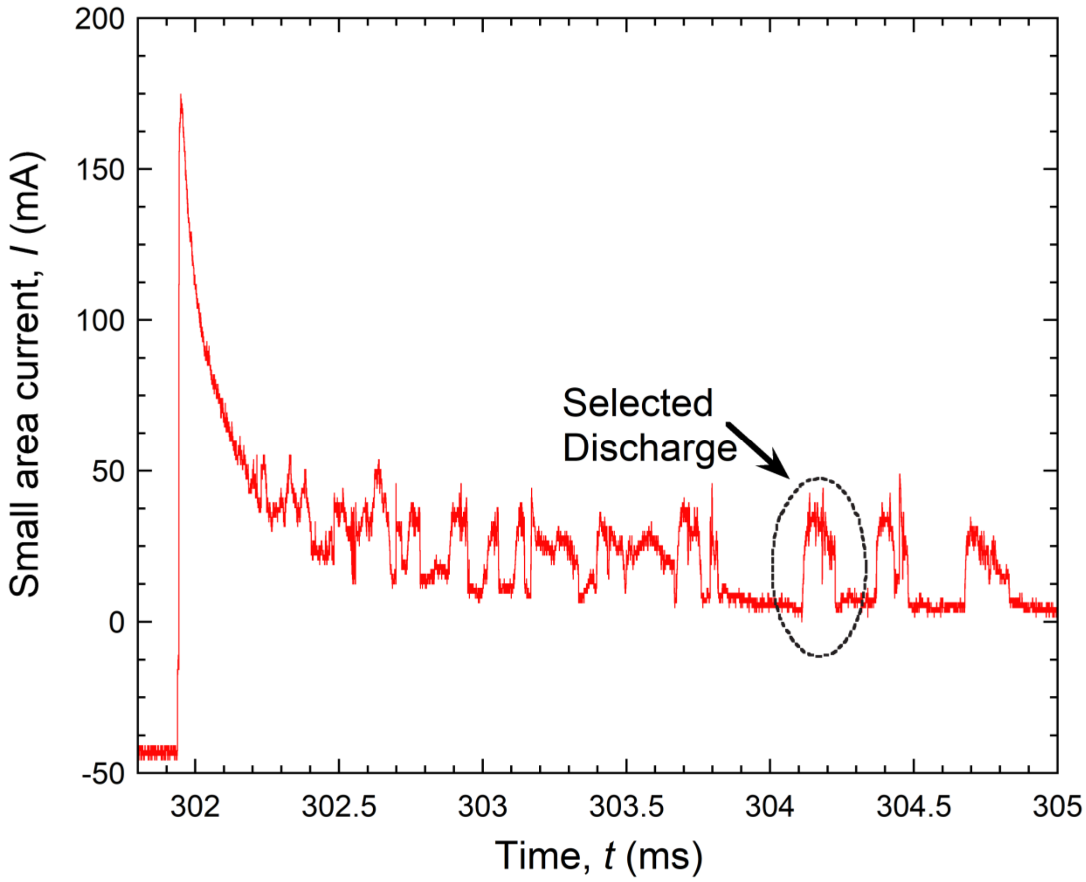

Figure 6.1 Section of the current–time relationship for the small area sample.

Figure 6.2 shows a higher resolution view of the current-time relationship for the selected discharge, together with the corresponding voltage-time relationship. In addition to allowing the duration of the pulse (~120 μs) to be accurately evaluated, this plot reveals that there are some spikes in the current profile. However, it is also clear from this figure that they arise from regular high frequency (~50 kHz) fluctuations in the applied voltage, which are present throughout and are unaffected by the presence or absence of current flow. They probably arise from some sort of source modulation or interference effect, and they are clearly unrelated to any phenomena associated with the individual discharges.

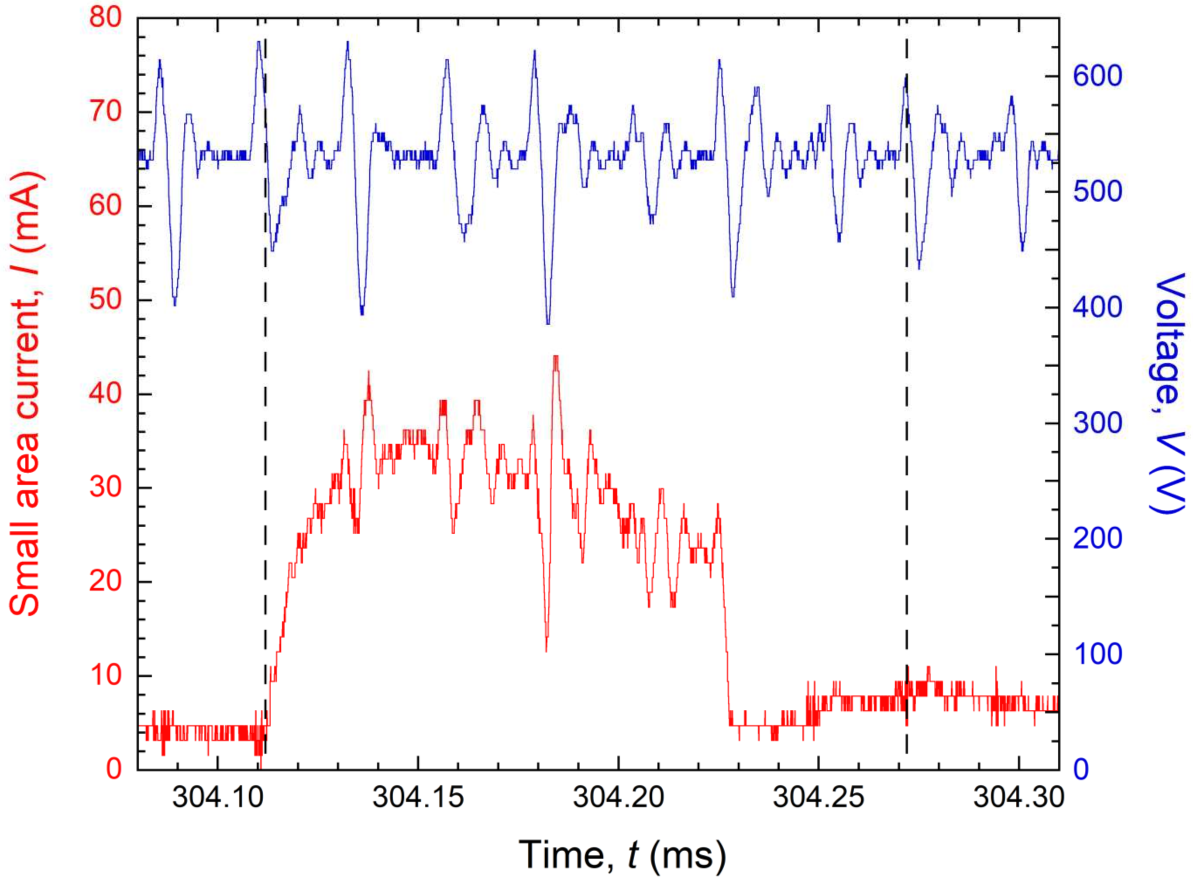

Figure 6.2 Synchronised current–time and voltage–time relationships for the small area sample, focussed on the period of the individual discharge indicated in Figure 6.1. The vertical dotted lines indicate the times at which the bubble associated with this discharge first appeared and finally disappeared.

6.3 Dynamics of bubble growth

Figure 6.3 shows a series of images from the video of the small area sample during the discharge indicated in Figure 6.1. These 12 images, each with an exposure period of 8 μs, cover the period indicated in Figure 6.2 as running from about 304.10 ms to 304.28 ms (i.e. about 180 μs). Every second image in the sequence is shown in this figure, so that the interval between them is 16 μs. It can be seen in this figure that the bubble expands more or less symmetrically from the bright spot representing the point where the discharge reaches the surface of the coating, and also contracts symmetrically. This bright spot remains visible up until the 304.216 ms image (arrowed), after which it disappears. There is still some light coming from the bubble area after that, although this appears to be due to reflections from the illuminating light source. This observation is consistent with the current-time plot in Figure 6.2, where it can be seen that the current is largely cut off at about 304.230 ms.

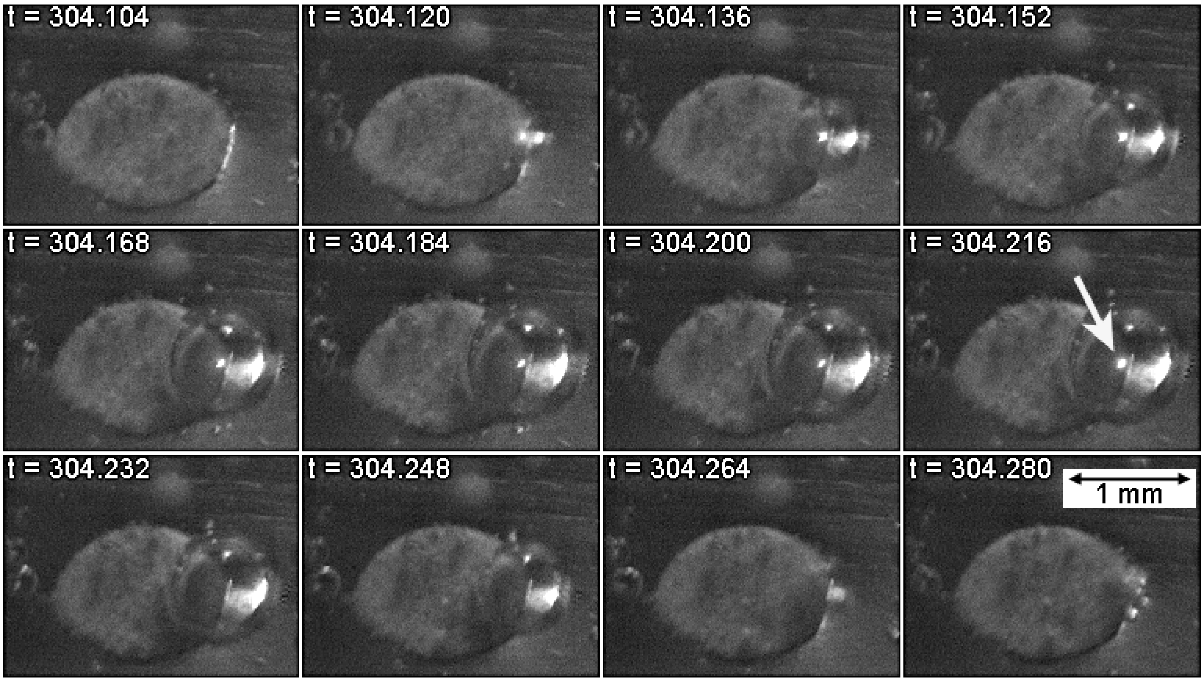

Figure 6.3 Sequence of video images covering the time period indicated in Figure 6.2.

It is certainly clear that electric current does continue to flow well after the bubble has started to form and grow. It is not so clear, however, what path this current is following during this phase. It may be going diffusely through the gaseous phase within the bubble, although there appears to be little or no (visible) plasma-like emission from this region—apart from the central bright spot, arrowed in one of the images, representing the discharge channel within the coating. There is also no evidence of a localised arc reaching the surface of the bubble. It should be noted that, while it would be unjustifiable to draw detailed general conclusions from study of a single discharge, data and images from many others in this investigation have been examined and the one under scrutiny here appears to be typical. Alternatively, the current may be reaching the bulk of the electrolyte at least partly via other routes, for example, through liquid flow or ionic diffusion within electrolyte contained in the pores within the coating surrounding the discharge channel. On the other hand, it seems very likely that it is an increase in the electrical resistance of the growing bubble that is responsible for cutting off the current. This issue needs further (experimental and theoretical) study.

It can also be seen that, once the current has stopped flowing, the bubble no longer contains a bright central spot. Furthermore, while the bright spot appears to have a radius of about 30 µm (broadly consistent with the apparent size of discharges monitored previously solely via light emission), the bubble grows to a maximum radius of about 500 µm. This is apparent in Figure 6.4, which shows measured values of the bubble radius from all 22 of the video images covering this period, together with the current-time plot. A further feature is also apparent in this plot. The bubble radius actually starts to reduce (at $t = 304.21$ ms) slightly before the current has stopped flowing (at $t = 304.23$ ms), although the shrinkage rate does accelerate considerably after the current has been cut off. It seems likely that there is an ongoing balance between (electrical) injection of energy and the various (energy-absorbing) phenomena associated with expansion of the bubble. It is certainly possible that this balance could lead to the bubble starting to shrink while some injection of energy is still taking place.

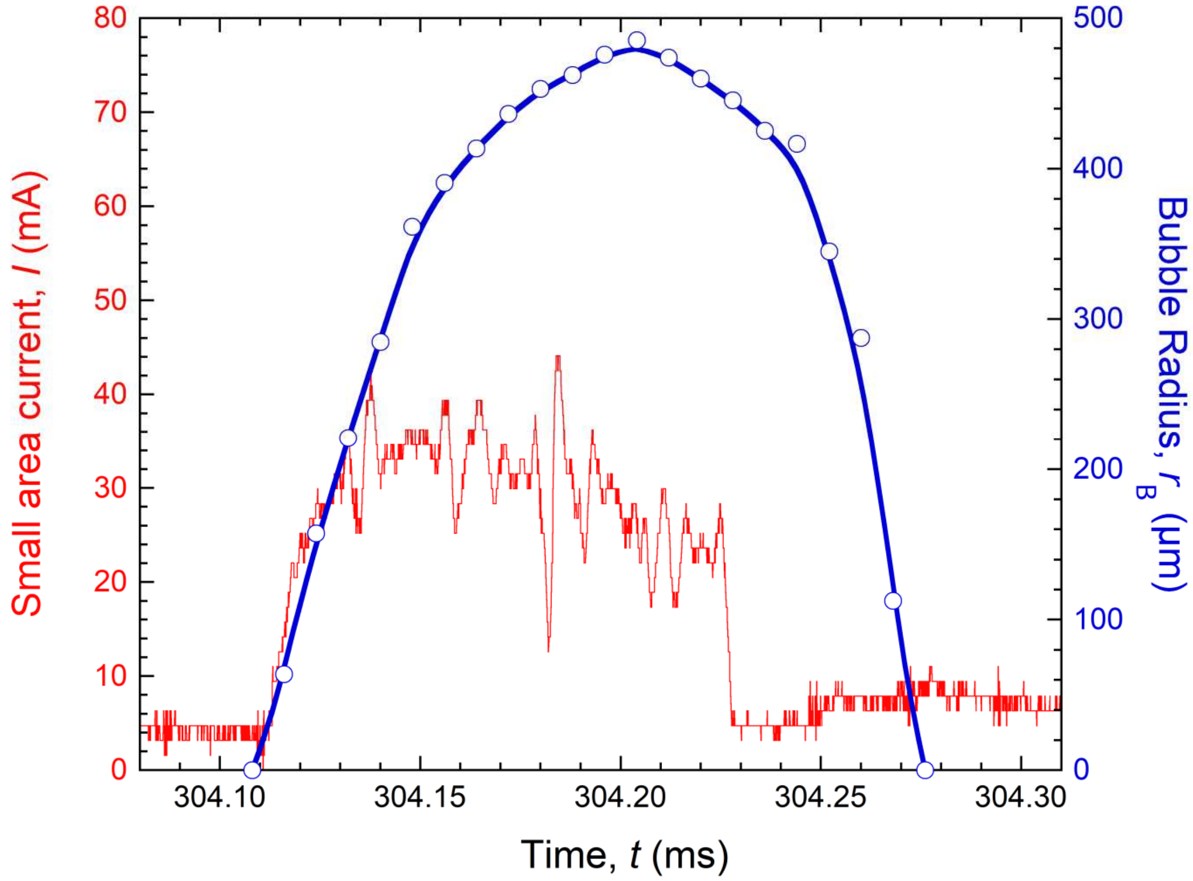

Figure 6.4 Synchronised current–time and bubble radius–time relationships for the small area sample, focussed on the period of the individual discharge indicated in Figure 6.1.

6.4 Pressure in a gas bubble

Expansion of a (hemi-)spherical gas bubble in a liquid, driven by an internal over-pressure, ΔP, is governed by the Rayleigh-Plesset equation, which may be written

$$\frac{\Delta P}{\rho_{\mathrm{L}}} = R\left(\frac{\mathrm{d}^2 r}{\mathrm{d}t^2}\right) + \frac{3}{2}\left(\frac{\mathrm{d}r}{\mathrm{d}t}\right)^2 + \frac{4\mu_{\mathrm{L}}}{r}\left(\frac{\mathrm{d}r}{\mathrm{d}t}\right) + \frac{2\gamma}{\rho_{\mathrm{L}} r} \tag{3}$$

where r is the bubble radius, ρ_L is the density of the liquid (~1,000 kg m^{-3}), μ_L is its kinematic viscosity (~10^{-6} m^2 s^{-1}) and γ is the energy of the gas-liquid interface (~0.05 J m^{-2}). For the present case, the right hand side is largely dominated by the second term. Applying the equation over the initial period of bubble growth, when the velocity of the interface is constant at about 10 m s^{-1} (see Figure 6.4), leads to a value for ΔP of about 1.5 bar. This pressure clearly drops off as the radius approaches its maximum, presumably because the rate of expansion of the bubble volume is no longer matched by the rate of vaporisation of water, but the main point to note is that the pressure never becomes large. This over-pressure value (~1 bar) is consistent with the fact that the rate of radius contraction after the water vapour has started to condense is similar to the rate of expansion (i.e. the plot in Figure 6.4 is approximately symmetrical), with the shrinkage presumably driven by an external over-pressure of about 1 bar.

It may, however, be noted that the pressure at the point when the bubble first starts to form could be appreciably higher than the regime indicated above. The work of Hamdan et al. [169] suggested that, immediately after ignition (within ~100 ns), the pressure may be tens or hundreds of atmospheres, but it falls off very quickly as the bubble expands. The temporal resolution of the present work is insufficient to draw any conclusions about effects occurring in these very early stages.

6.5 Energetic processes of individual discharges

It has long been clear that for PEO, unlike conventional electrochemical processes such as electroplating, it is not possible to associate a given amount of “deposition” or “conversion” with a certain quantity of charge. Indeed, the concept of the efficiency of a PEO process, in terms of comparing the energy consumed with the “minimum” energy required, is not a valid one since, in principle, oxidation of the metal should release energy, rather than consume it. Nevertheless, there is considerable interest in evaluating the energy consumption per unit volume of coating produced, understanding its origins and, if possible, minimising its value. The detailed information regarding individual discharges obtained in this work, and corresponding macroscopic observations, allows such an assessment to be made. The highlighted discharge presented in the previous sections of this chapter will be used as an example for analysis purposes.

6.5.1 Oxidation associated with individual discharges

Taking typical order of magnitude values, the rate of PEO growth is ~1 μm min^{-1}, or ~15 nm s^{-1}, over a wide range of coating thickness. Recognising that there is often an increase in volume as an oxide forms from its metal (the Pilling–Bedworth ratio for Al is about 1.28), that the oxide is quite porous, and that there is often some incorporation of species from the electrolyte, the rate of consumption of the substrate might thus be ~10 nm s^{-1}. A typical corresponding current density can be taken as ~10 A dm^{-2}, occurring in the form of discrete discharges—each of which carries, say, one μC of charge [47]. (It must be recognised that discharges vary considerably in intensity, even for a given coating thickness, and also tend to become more intense as the thickness increases.) This current density therefore corresponds to about 10^9 discharges per m^2 per second, or about 1 discharge within 1 mm^2 in 1 ms. Recognising the crude nature of the estimate, this is broadly consistent with the observations presented in §5.1.

The substrate consumption rate of 10 nm s^{-1} corresponds to 10 μm^3 mm^{-2} ms^{-1}, so one discharge consumes ~10 μm^3 of Al (creating ~15 μm^3 of coating). In terms of energy consumption, this represents ~10^{13}–10^{14} J m^{-3} of coating (since the energy of a discharge [47] is typically 100–1,000 μJ). This is broadly consistent with macroscopic electrical power consumption data. For example, Matykina et al. [145] reported very similar values (expressed as ~3 kW h m^{-2} μm^{-1}, equivalent to ~1.1×10^{13} J m^{-3}) obtained from external electrical measurements of current density and RMS voltage. They also showed that (relatively small) reductions in overall power consumption could be obtained by growing thicker "precursor" layers of porous alumina under conventional anodizing conditions with no discharge formation.

Taking the energy consumption rate of 10^{13} J m^{-3} of coating equates to ~200,000 kJ mole^{-1} of alumina produced. This is a high value, particularly when it is recognised that the thermodynamic change in energy associated with the oxidation is ~1,500 kJ mole^{-1} of alumina, which is negative rather than positive. There should thus be considerable scope for energy saving if the mechanism of exposing the substrate to oxygen can somehow be made more efficient. A potentially promising direction for this would be to reduce the energy of each discharge, possibly by limiting the voltage at which it is initiated.

6.5.2 Energy associated with coating production and heating

A volume of ~10 μm^3 oxidised per discharge corresponds to a mass of about 0.03 ng. This quantity of material must be melted and vaporised, and then raised to the temperature of the plasma. Estimates of the plasma temperature within a discharge vary considerably, but are no higher than about 10,000 K. The energy required, Q, to vaporise this mass, m, of material, and raise its temperature to 10,000 K, can be calculated from the following equation

$$Q = mC_{\mathrm{p}}\Delta T + m\Delta H_{\mathrm{melt}} + m\Delta H_{\mathrm{vap}} \tag{4}$$

where the specific heat, C_{p}, is taken to have a value of ~1 J g^{-1} K^{-1} for the substrate material and ΔH_{melt} and ΔH_{vap} (latent heats of melting and vaporisation) have values of 400 J g^{-1} and 10,500 J g^{-1} respectively. Vaporising this quantity of material requires just 0.6 μJ, which is an insignificant fraction of the total energy input (~1 mJ).

It is not really clear whether the plasma formed during PEO can be considered to be in local thermal equilibrium (i.e. whether the effective temperatures of electrons and other species are similar). Most spectroscopic measurements suggest that it is probably not, at least in the early stages, and some estimates of the true effective temperature of the bulk of the material present are considerably lower (below 5,000 K). However, it is clear that the outcome of this calculation (i.e. that the energy required to raise the quantity of material present in the plasma to a very high temperature is negligible compared to the electrical energy injected) would be the same for any plausible temperature that could be used.

Melting of existing coating material surrounding the discharge also turns out to require relatively little energy, even though the quantity of alumina involved in this is considerably larger than the amount actually formed during each discharge. Taking the region of (alumina) coating to be melted as a cylinder of radius 10 μm and thickness 5 μm, the mass concerned is ~6 ng. Assuming that the molten coating remains at the melting temperature of alumina (~2,300 K), and taking its latent heat of melting, ΔH_{melt}, to be 1,150 J g^{-1}, the energy required is obtained from

$$Q = mC_{\mathrm{p}}\Delta T + m\Delta H_{\mathrm{melt}} \tag{5}$$

giving a value of ~20 μJ. This is greater than that required to vaporise the metal being oxidised, but is still much less than the total electrical energy being injected. This is perhaps encouraging in terms of suggesting that the irreducible minimum amount of energy associated with a process of this type may be much smaller than the quantity that is typically consumed.

6.5.3 Plasma formation

The energy required to create and sustain the plasma is more difficult to calculate, and the following analysis contains some crude approximations. Creation of the plasma requires ionisation of atoms. The electron density within the plasma has been estimated experimentally (via spectroscopic measurements) to be between 10^{12} and 10^{14} mm^{-3}. The ionisation energy (H and O atoms) is of the order of 2×10^{-18} J atom^{-1}. An upper bound can be obtained by assuming that the entire gas bubble (r_B ~500 μm) has an electron density of 10^{14} mm^{-3}. It follows that the energy required to ionise sufficient atoms would be ~50 μJ. This is again relatively small, although perhaps not entirely insignificant, in the context of an injected energy of around 1 mJ. Of course, this takes no account of the energy needed to sustain the plasma, which is more difficult to estimate. The maximum contribution from this source is likely to be about twice that for ignition. In any event, even making upper limit assumptions, the value is still small compared with the total injected energy.

6.5.4 Vaporisation of water

The main reason why the above contributions to the energy audit are all rather insignificant is simply that the quantity of material involved in each case must be very small. However, this is not necessarily true for vaporisation of water (electrolyte). An estimate of interest is the mass, m, of water that could be vaporised by the total amount of energy injected by the discharge, E. The specific heat of water, C_p, is 4.2 J g^{-1} K^{-1} and its latent heat of vaporisation, ΔH_vap is 2,260 J g^{-1}. For water initially at 298 K to be heated to 373 K and then vaporised (and remain at this temperature), the mass, m, for which this can be done is obtainable from

$$E = mC_\mathrm{p}\Delta T + m\Delta H_\mathrm{vap} \tag{6}$$

Assuming ideal gas behaviour, with atmospheric pressure and a hemi-spherical geometry, the following relationships apply between gas volume, v, gas pressure, P, absolute temperature, T, gas constant, R, number of moles of gas, n, and bubble radius, r_B

$$v = \frac{nRT}{P} \tag{7}$$

$$r_B = \sqrt[3]{\frac{3v}{2\pi}} \tag{8}$$

A value for the discharge energy, E, of ~1.5 mJ (obtained by numerical integration of the product of voltage and current for the selected discharge) then leads to a mass, m, of 580 ng, corresponding to n ~3.2×10^{-8} mol. This mass of water, in the liquid state, would occupy a hemi-sphere of radius ~65 μm and would, as a gas at atmospheric pressure, generate a bubble of radius ~780 μm. Heat transfer to the coating, substrate and surrounding electrolyte have been neglected here, but would all reduce the energy available to vaporise the electrolyte. There may also be some electrolysis or thermal decomposition of water, which would absorb further energy.

It seems clear that the quantity of water that would need to be vaporised in order to absorb, at least most of, the injected energy is quite plausible in terms of the volume of the hemi-sphere of water vapour that would be created, assuming the pressure in it remains close to atmospheric—which the calculation in §6.4 suggests it will. Certainly, in the absence of water vaporisation, it is difficult to see how the dramatic expansion in bubble volume, relative to the volume of the discharge channel in the coating, could possibly occur without the pressure in it dropping well below atmospheric, in which case it would not be able to expand. It is easy to show that thermal expansion of this small quantity of material cannot account for the observed bubble growth—it would require heating to a completely unrealistic temperature, and it is already very hot when inside the discharge channel. It is unclear at this point whether there is significant ionisation of this large quantity of vaporised water, as was assumed in the calculation in §6.5.3 regarding the energy required for plasma formation. However, it does seem unlikely that the entire bubble is actually ionised to this extent, otherwise the resistance of the bubble would not increase significantly as the bubble expanded, meaning there would be no need for the current to shut-off.

6.5.5 *Joule heating of the electrolyte*

It is fairly clear that, whatever forms the injected energy may transiently take after injection, most of it will end up as a raised temperature of the electrolyte, which in turn will have to be carried away by some form of heat exchanger if the process is to continue for any length of time. For example, if much of it does indeed get transformed from electrical/plasma energy to being stored in the form of a relatively large quantity of water vapour, this will subsequently condense, releasing this heat into the bulk of the electrolyte. However, it is possible that some of the electrical energy could be transferred directly into the electrolyte. The resistance, R, of the electrolyte through which the current is passing can be estimated using [77]

$$R = \frac{\rho}{2\pi r_{\mathrm{B}}} \tag{9}$$

$$\Delta V = \frac{I\rho}{2\pi r_{\mathrm{B}}} \tag{10}$$

where ρ is the resistivity of the electrolyte. The conductivity of the electrolyte was 5.1 mS cm^{-1}, corresponding to a resistivity of around 2 Ω m (although stirring of the electrolyte may increase this). At the maximum bubble radius (~500 μm), the current, I, flowing through the discharge was ~30 mA, giving a voltage drop across the electrolyte, ΔV, of ~20 V. Since the total voltage drop was of the order of 500 V, the assumption that all the electrical energy is dissipated in the discharge site, or at least in very close proximity to it, appears to be valid.

6.5.6 Chemical energy of oxidation

Of course, the underlying chemical reaction is simply that of aluminium being oxidised to alumina. This contribution to the energy audit differs from all of the others, in that it is negative in sign (i.e. this energy will be released, rather than absorbed). Its magnitude is straightforward to estimate. The quantity of Al being transformed per discharge is about 0.03 ng (see §6.5.1), leading to the formation of about 0.057 ng of Al_2O_3. The free energy of the reaction is about 1,500 kJ mole^{-1} of alumina formed. The energy released per discharge is thus about 1 μJ. This is much smaller than all of the other contributions, reflecting the very low efficiency of the PEO process from an energetic point of view.

6.6 Summary of energy audit conclusions

The information presented from synchronised current monitoring and high-speed video imaging of individual discharges formed during PEO processing at 50 Hz AC has provided insight into a number of things. The ignition of a discharge, and creation of a plasma channel through the thickness of the coating, is quickly followed by formation and growth of a (hemi-spherical) gas bubble, centred on the plasma channel (which probably has a radius ranging up to a few tens of μm, depending on coating thickness). This bubble grows rapidly, typically reaching a radius of about 500 μm during the lifetime of the discharge. It seems likely that this bubble growth is responsible for a sharp increase in the electrical resistance of the current path, leading to the current shutting off. From the observed rate of growth of the bubble, it is concluded that the peak over-pressure within it is relatively low (of the order of 1 atmosphere).

The above estimates of the quantities of energy, in different forms, associated with a single discharge are, of course, relatively crude, although they are certainly informed by the newly acquired experimental information that is reported here. A semi-quantitative attempt to present this information graphically is shown in Figure 6.5 (omitting the chemical oxidation energy, which is negligible compared to the other contributions). This depicts the relative significance of the heating and phase changes experienced by the different constituents present. Furthermore, in addition to omitting the chemical energy, there is no attempt to incorporate the contribution from electrolysis of water—the extent of this is not well-established, but its contribution is in any event expected to be small. Evidently, assuming that this summary is reasonably accurate, most of the injected energy is (transiently) absorbed in the form of vaporisation of water, after which it will inevitably end up as rather low grade, difficult to recover, energy in the form of a large mass of moderately heated electrolyte.

There does not appear to be any immediately obvious way of reducing this energy wastage, although improved understanding of details such as those presented here is certainly of potential value in considering various measures. The basic problem appears to be that exposing the substrate to oxidising agents via these highly energetic discharges is very inefficient, at least under the conditions conventionally employed. Suppressing bubble growth (for example, by pressurising the liquid) would not necessarily reduce the energy wastage, although measures such as this might be worth exploring. The most promising approach is probably to somehow reduce the energy associated with each discharge (while retaining a similar rate of transformation of substrate), or to promote more transformation per discharge, while retaining a similar discharge energy. Further study of the details of the energetics of the process is clearly likely to be helpful in pursuing such aims.

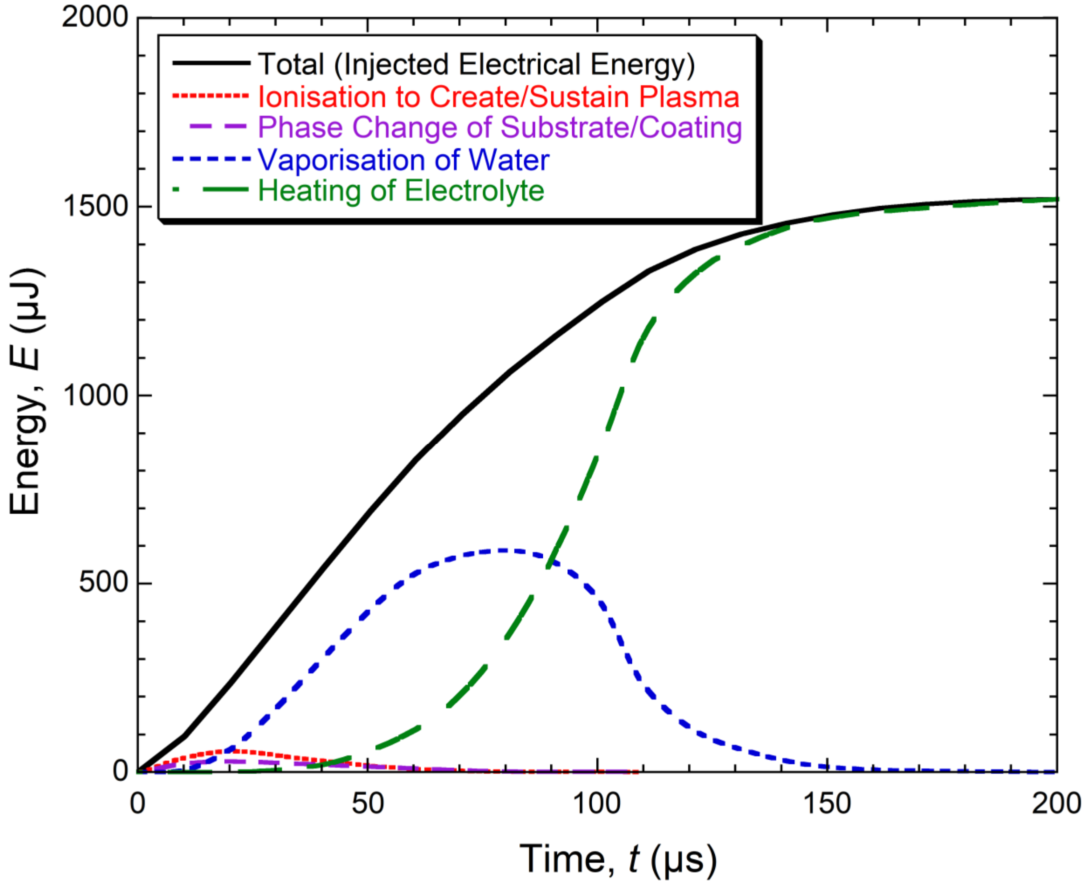

Figure 6.5 Semi-quantitative plot showing how the total electrically-injected energy changes during formation of the individual discharge under consideration here, and how it is converted between different forms during and immediately after the discharge period.

Chapter 7

Effect of Supply Frequency on the Appearance of Cathodic Discharges

Increasingly, PEO coatings are produced using higher (variable) frequency power supplies as opposed to the traditional mains frequency (50 Hz) machines. There are some limited studies of the effects of frequency, although mechanistic explanations are often lacking. Additionally, what actually happens during the cathodic half-cycle is often left rather unclear, although increasing attention is being paid to this—particularly in regards to the so-called “soft regime”, see §3.5. Usually, the cathodic process is smooth and continuous, however, discharges have been observed during the cathodic half-cycle (§3.4) under certain conditions.

The present work aims to investigates how the process changes as the supply frequency is increased, such that the cycle period is no longer large compared with the inter-discharge period, or the discharge period itself. The nature of the discharges is investigated using high-speed video and electrical monitoring of individual discharges and these are correlated with the effects on the coating microstructure. Additionally, the mass gain and volume of gas liberated during processing has been monitored to investigate the changing mechanisms as the process supply frequency is increased.

7.1 Experimental details

Small area sample investigations were carried out using the same conditions described in §6.1.

Another set of experiments were performed using Al-1050 plates with dimensions of 50 × 25 × 1.2 mm, which were attached to a small aluminium block using a nylon screw. These were used for mass gain monitoring, as well as determining the number of anodic and cathodic discharges. Camera recordings were made from the centre of the plate using the Phantom V12.1 camera, with the acquisition rate set at 100,000 frames per second. The linear spatial resolution was 34 μm per pixel. Typical images comprised 160 × 160 pixels, covering an area of 30 mm^2. Recordings were performed throughout processing in sequences which lasted 173 ms each.

7.2 Electrical characteristics at different supply frequencies

7.2.1 Bulk and small area current and voltage characteristics at 50 Hz

Figure 7.1(a) shows a typical voltage profile during a single 50 Hz cycle (a period of 20 ms), at a stage when the coating thickness was about 40 μm. This voltage acts across both the bulk and small area samples. It can be seen that the profile approximates to a square wave, with the anodic voltage being ~600 V, while the cathodic voltage is ~125 V. It should be noted that these voltages are not pre-selected, but are adjusted by the machine to maintain the set current values. Figure 7.1(b) shows corresponding currents, both the total and through the small area sample. Apart from short initial transients on switching polarity, the total current was just above 2 A throughout both anodic and cathodic half-cycles (approximately the pre-selected current density of 31 A dm^{-2}).

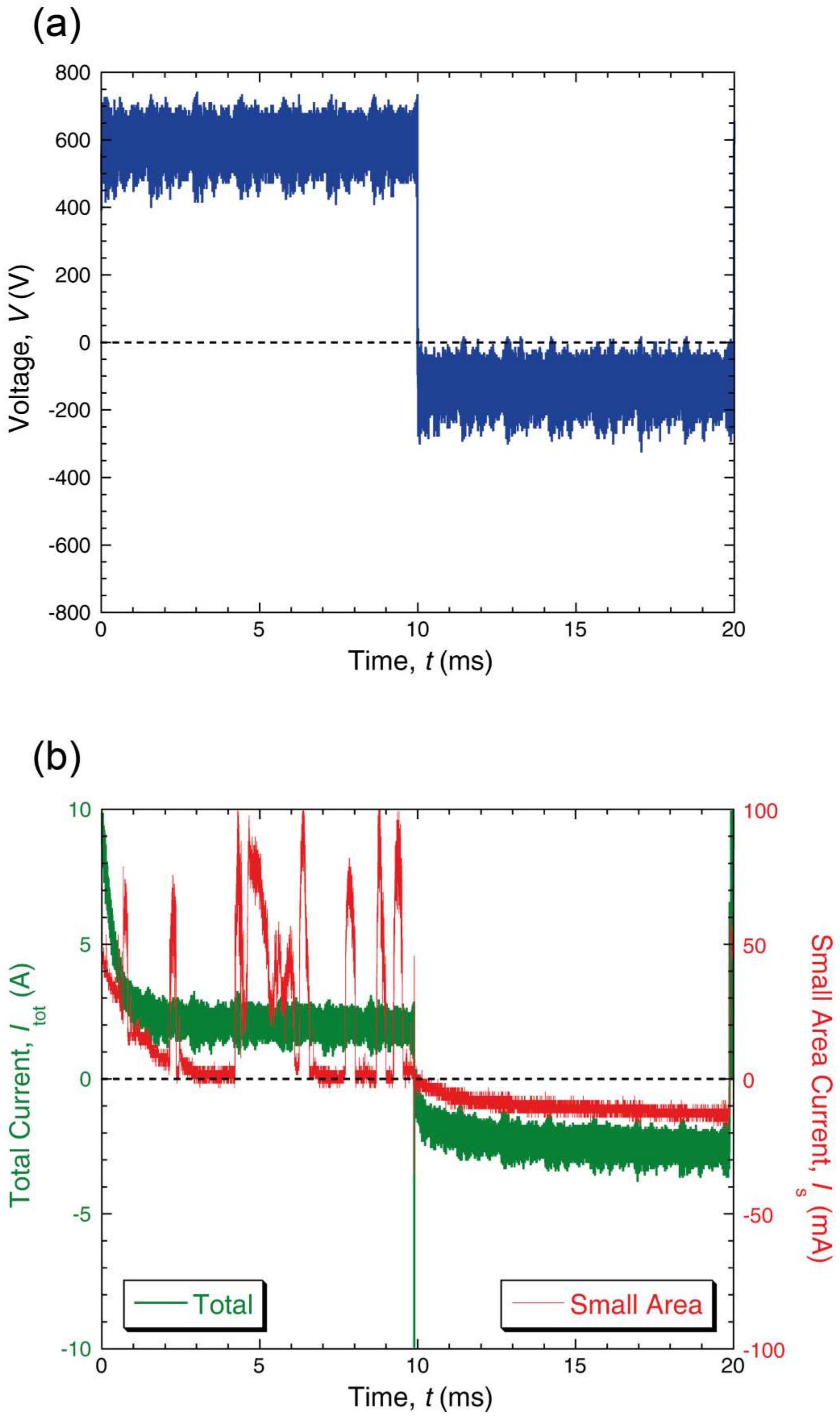

Figure 7.1 Profiles during a single cycle of PEO processing at 50 Hz, with the current set to ± 2 A and a coating thickness of ~40 μm, showing (a) voltage and (b) current, both the total and that flowing through the small area sample.

It can be seen that the cathodic current through the small area reflects the total current, taking account of the area ratio between small and large samples, the greater significance of edge effects for the small sample, and some coating on the cylindrical face between the wire and the resin. This suggests a cathodic process that is smooth and continuous, such as might be expected for conversion of protons to hydrogen gas. In contrast to this, the anodic current is made up of a series of current pulses corresponding to discharges. The integrated area of these pulses in a single half-cycle does not necessarily correspond to the area-normalised total current, since there are likely to be variations in the number of discharges in each cycle and, there may be periods of several cycles when there are no discharges on the small sample. Figure 7.2 shows nine images of the small area sample, taken at different times during the anodic part of the cycle shown in Figure 7.1. It can be seen that the periods during which there are current pulses correspond with images in which light is being emitted from two distinct points on the surface of the sample, corresponding to two active discharge cascades. Observations of this type, which were discussed in some detail in Chapter 5, confirm that the anodic current pulses arise from “cascades” of discharges, which tend to occur in particular locations.

These characteristics, including the absence of well-defined discharges in the cathodic half-cycle, are consistent with the majority of previous observations and reports.

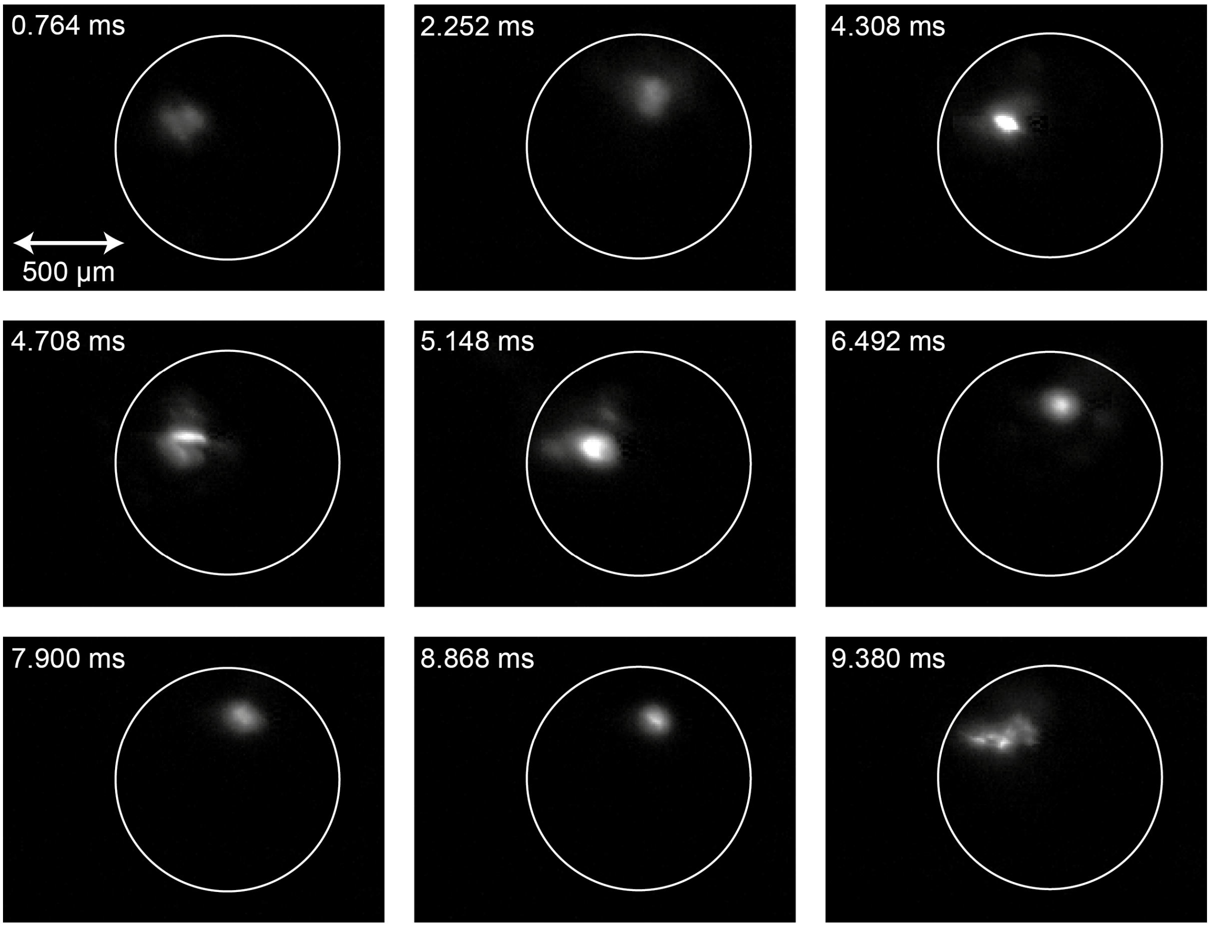

Figure 7.2 Individual high-speed video images of the small area sample, taken during the run that produced the data in Figure 7.1, with times indicated that correspond to those plots. There are two cascade locations undergoing discharging during this particular anodic half-cycle.

7.2.2 Effect of supply frequency on discharge characteristics

As the supply frequency was increased, and the half-cycle period started to approach typical lifetimes of the discharges, certain changes were observed in the nature of the voltage and current profiles, although, as with the behaviour at 50 Hz, there were some cycles in which no discharges occurred on the small sample. Figure 7.3, which shows profiles from experiments carried out at 2,500 Hz after 18 minutes of PEO processing (giving a coating thickness of ~40 µm), illustrates these changes. The voltage profiles (Figure 7.3(a)) are similar to those at 50 Hz (Figure 7.1(a)), except that the cathodic voltage has risen to about 250 V, compared to 125 V at 50 Hz, while the anodic voltage remained unchanged at about 600 V. This suggests a switch to a cathodic process that requires a larger driving force. It is also clear from the current profiles (Figure 7.3(b)) for the small area that changes have occurred in phenomena occurring during the cathodic part of the cycle. While the anodic discharges are still taking place with approximately unchanged lifetimes, of the order of 100–200 μs (now occupying most of the half-cycle), and similar current levels of ~50–100 mA, there are now clear current pulses in the cathodic part of the cycle as well. Moreover, some of these pulses rise to higher current levels than those of the anodic discharges, with peaks approaching 200 mA.

Experimental runs were carried out over a range of frequencies. Cathodic discharges were only detected above a supply frequency of 1,750 Hz.

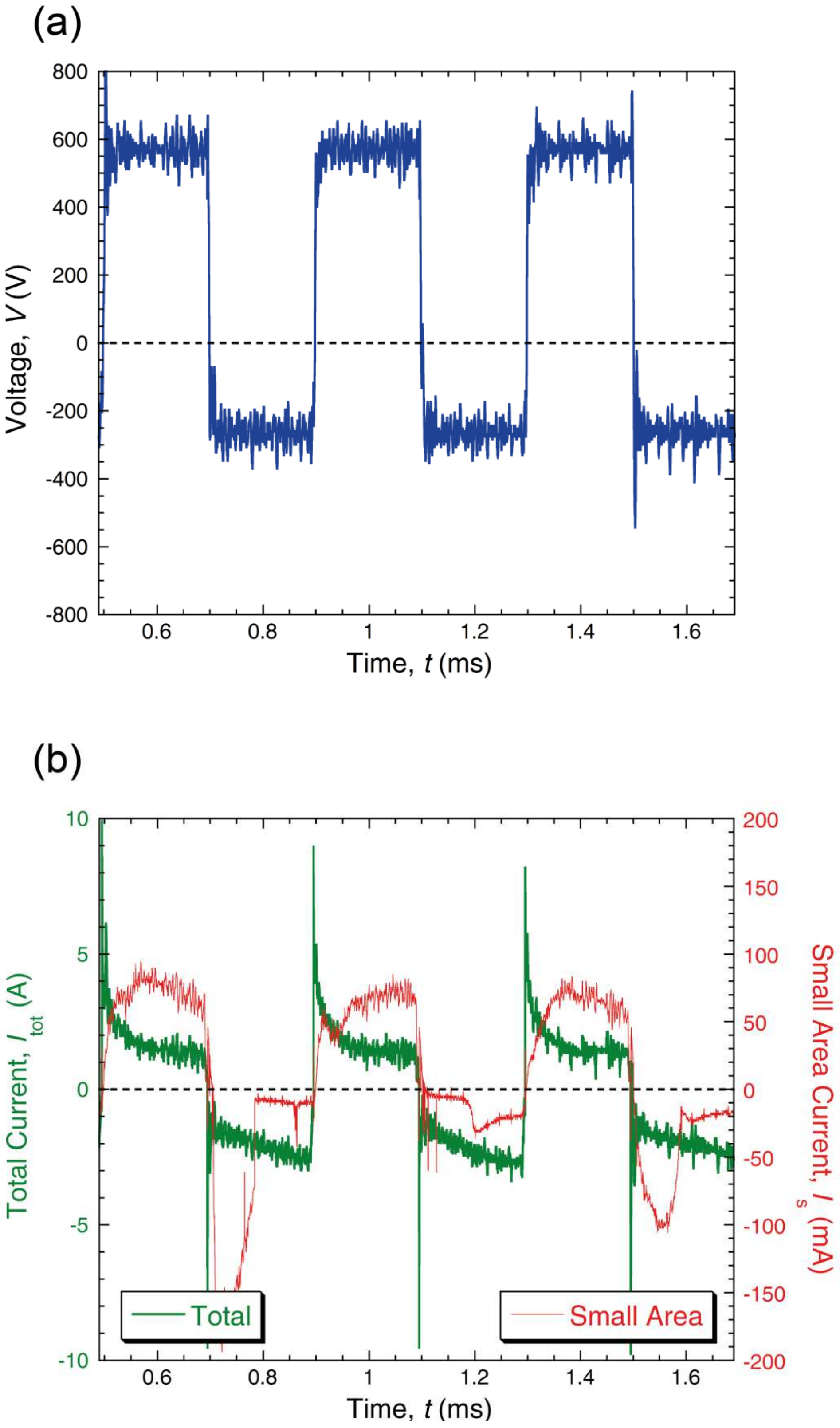

Figure 7.3 Profiles during PEO processing at 2,500 Hz, with a coating thickness of about 40 μm, showing (a) voltage and (b) current, both the total and that flowing through the small area sample.

Confirmation that these cathodic pulses correspond to discharges is provided by high-speed photography observations, with the images in Figure 7.4 showing superimpositions of the set of frames (25 images) covering each half-cycle, that light emission accompanies both anodic and cathodic pulses. It also appears that, as for the anodic discharges, those in the cathodic half-cycle also occur in spatially localised “cascades”. In the example shown in Figure 7.4, the two types of discharge occur in different locations, although this is not necessarily a general feature, since they occur in the same location for the example in §5.3.4. This suggests that the (microstructural or electrical) “priming” of a site by a discharge, making it a likely site for the next discharge, does not necessarily operate for discharges with the opposite polarity, or that there is insufficient time for the pore channel to refill with electrolyte when the polarity is switched.

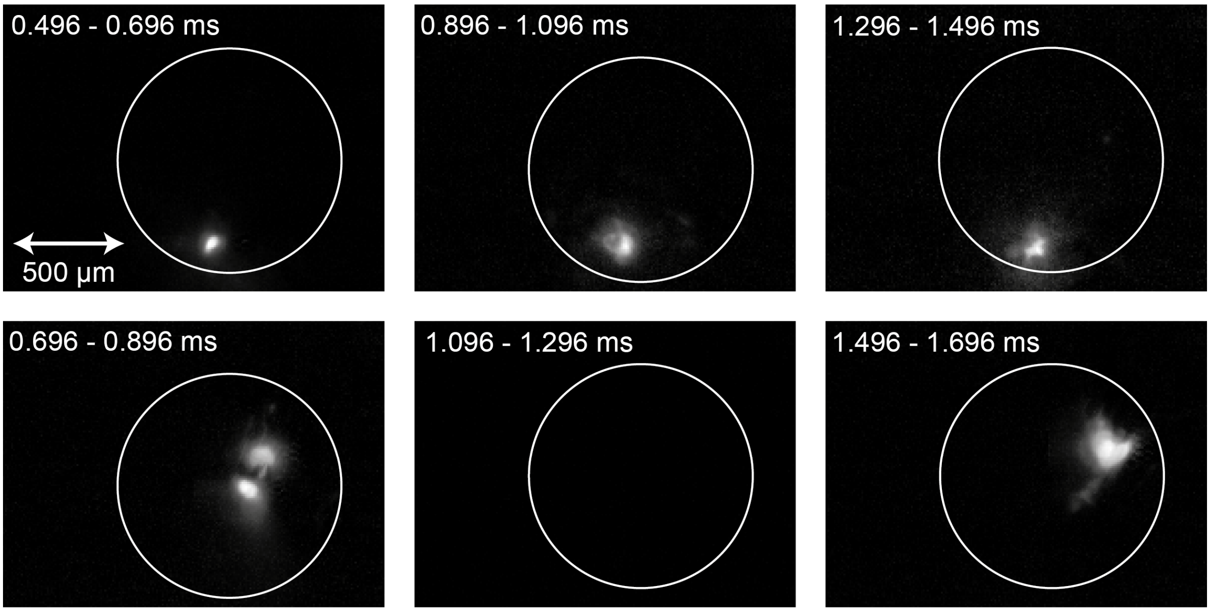

Figure 7.4 Sequence of superimposed sets of video images (each made up of 25 separate images, covering one of the 6 half-cycle periods shown in Figure 7.3), during PEO processing at 2,500 Hz, with times indicated that correspond to those plots. The first row of images is from the anodic half-cycles, with discharges occurring in one location. The second row of images is from the cathodic half-cycles, with discharges only occurring in two of the three cathodic periods, in a spatially localised region that is separate to the anodic cascade location.

7.3 Promotion of cathodic discharges

7.3.1 Effect of coating thickness

There were no cathodic discharges recorded during 50 Hz processing of Al in this work, as is commonly observed and reported. However, as shown in the previous section, cathodic discharges can occur when processing at high (2,500 Hz) frequency. The effects of coating thickness were investigated using Al-1050 plates, processed for various times. Mass gain and thickness measurements are presented in Figure 7.5. The rate of coating growth remains approximately linear for 50 Hz processing, but a change occurs during high frequency processing at between 20 and 25 minutes, when the coating growth rate and mass gain drop significantly.

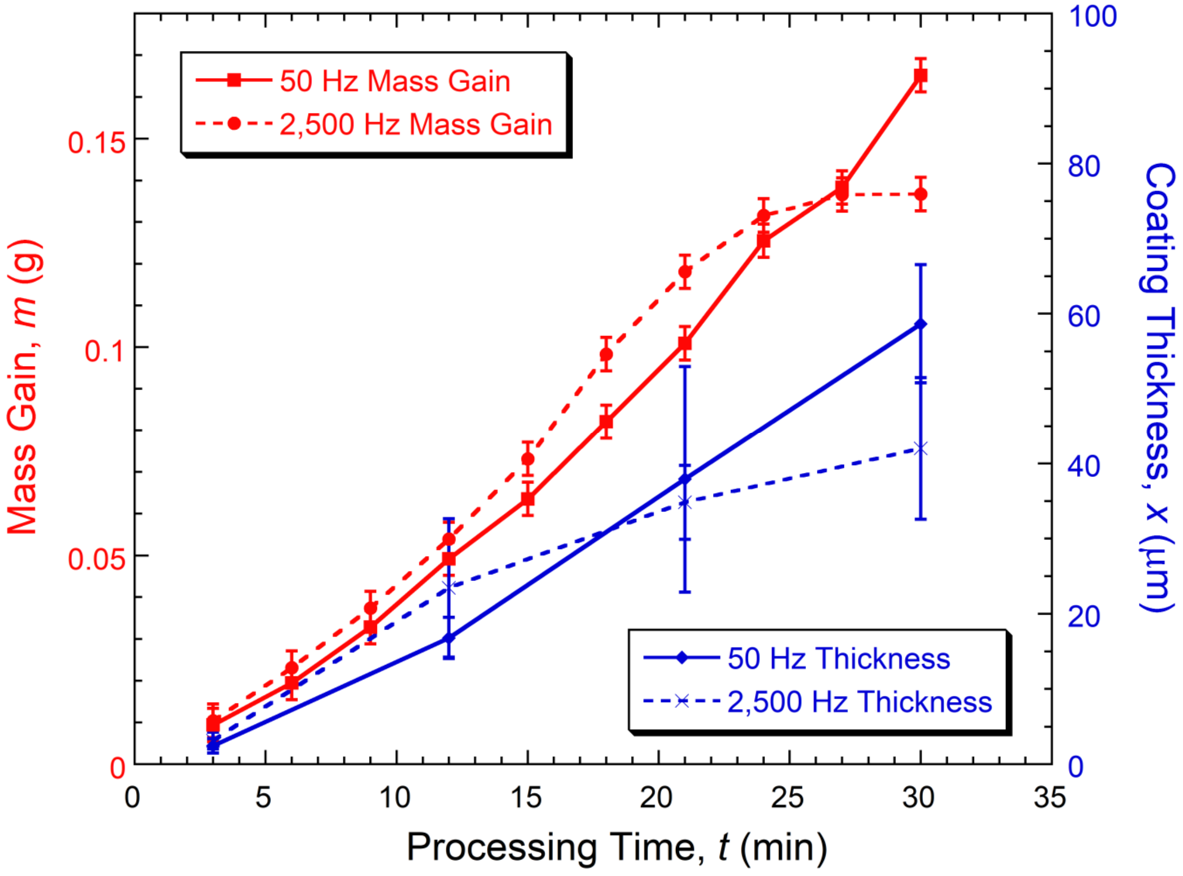

Figure 7.5 Mass gain and coating thickness measurements for Al-1050 plates, as a function of processing time for 50 Hz and 2,500 Hz process supply frequencies.

This change in coating growth rate coincides with the onset of cathodic discharges during the high frequency processing. These cathodic discharges only form once the coating thickness has reached around 30–40 μm. Figure 7.6 shows the number of cathodic and anodic discharges that occurred during a 173 ms camera recording (covering ~430 cycles of the applied potential), of a 30 mm^2 area in the centre of the plates, after different processing times. This is a relatively short snapshot of the process and the number of active discharge sites is quite small, so there are some statistical variations in the data presented. However, a clear trend can be seen, with the number of cathodic discharges increasing significantly above ~20 minutes of processing, rising to a plateau value after ~25 minutes of processing. Anodic discharges, on the other hand, occurred throughout the process, with their frequency dropping off with increasing time (at least over the initial 15 minutes of processing). This observation of anodic discharges becoming rather less frequent, but more energetic, as the coating becomes thicker, has been made many times previously. Noting the log scale of this plot, it can be seen that, even when cathodic discharges become established, they remain substantially less common than anodic ones.

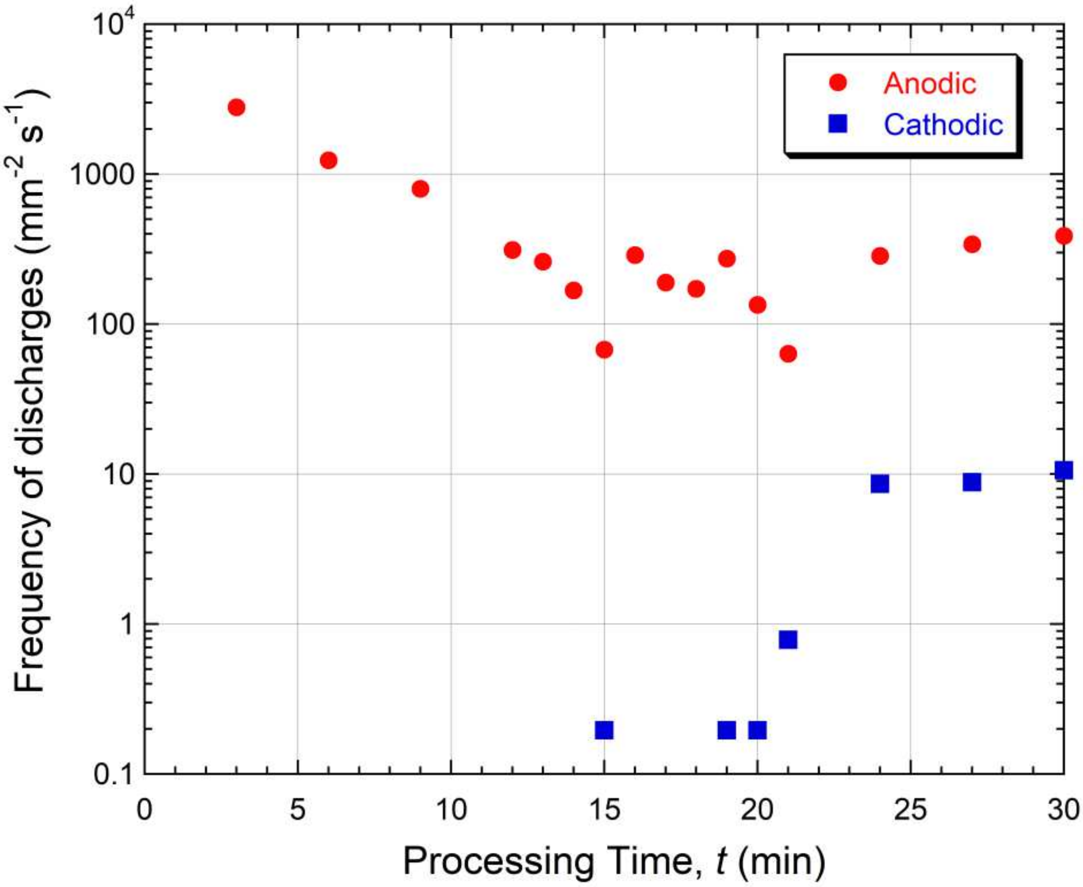

Figure 7.6 Data for the spatial and temporal frequency of both anodic and cathodic discharge during processing at 2,500 Hz, taken from a series of short video sequences (each 173 ms long), covering a representative (30 mm^2) area of the sample.

The evolution of the applied potential, which is allowed to vary freely to achieve a set current density of 30 A dm^{-2}, is shown in Figure 7.7. The anodic voltage for high and low frequency remain very similar throughout processing. The cathodic voltage, at 50 Hz, gradually increases with processing time from around -110 V to -145 V after 30 minutes of processing. At 2,500 Hz, the cathodic voltage increase at a faster rate from -135 V to -250 V in the first 20 minutes of processing, and then at a more gradual rate for the remaining 10 minutes. The initial increase in cathodic voltage implies the cathodic process is more difficult at higher frequency, due to some kinetic effects. The change in gradient coincides with the increase in the number of cathodic discharges. This suggests a change occurs in the cathodic process at this time. Once a critical cathodic voltage is reached, cathodic discharges are able to occur readily, and carry much of the imposed current, rather than the discharge of protons at hydrogen gas.

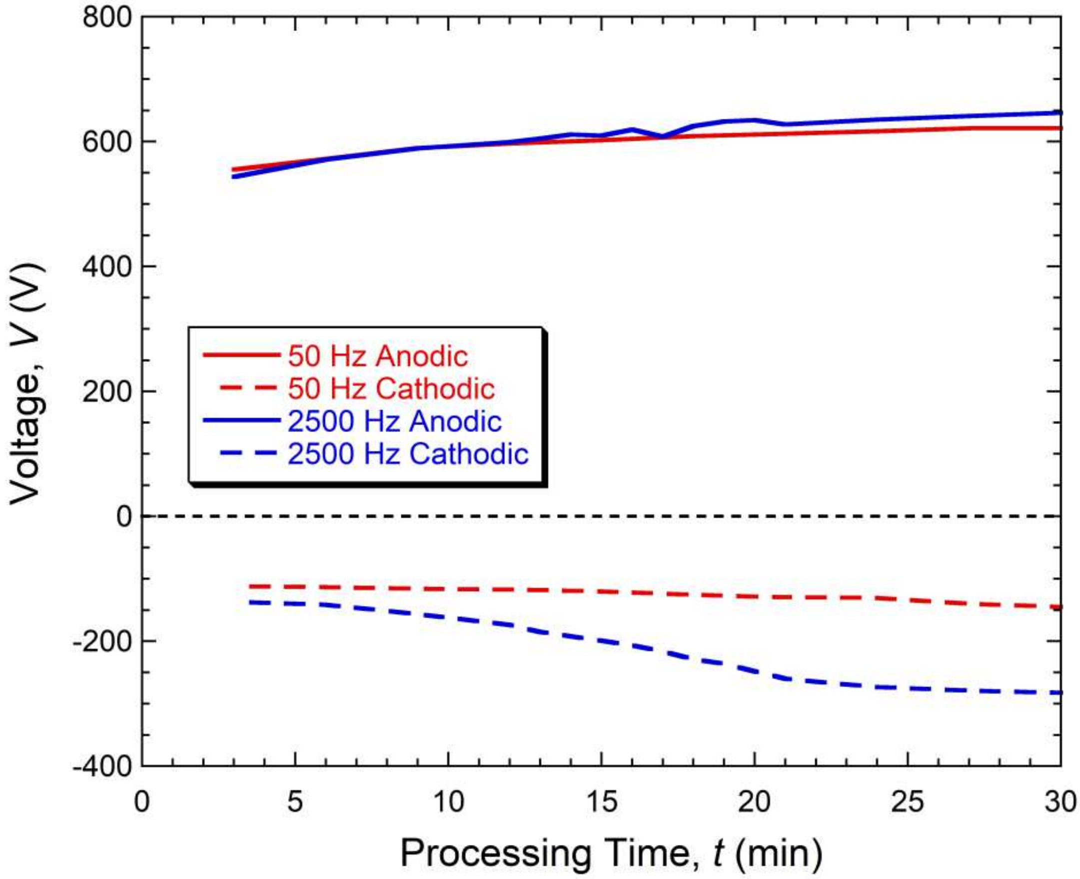

Figure 7.7 Evolution of the anodic and cathodic voltage during PEO processing at 50 Hz (red) and 2,500 Hz (blue) of Al-1050 plates at 30 A dm^{-2}. The anodic voltage is very similar throughout processing for both cases, however, the cathodic voltage at high frequency deviates from the low frequency case.

7.3.2 Microstructural effects of high frequency and cathodic discharges

The plates processed for 3, 12, and 30 minutes at 50 Hz and 2,500 Hz were chosen for microstructural examination. The micrographs in Figure 7.8 show the evolution of the coating free surface at 50 Hz and 2,500 Hz. In general, the samples processed for the same times at different frequencies have similar microstructures. At short processing times, the discharge channel pores are relatively small (around 1 μm diameter) and numerous. Longer PEO processing causes the features to coarsen, with pancake diameters reaching several tens of microns across, as has been widely reported. However, the sample processed for 30 minutes at 2,500 Hz contains a number of large, deep craters, which are not present in the 50 Hz 30 minute sample. One such crater can be seen in the centre of the bottom right image of Figure 7.8. A more complete impression can be seen in Figure 7.9, which shows a low magnification image of the 30 minute sample processed at 2,500 Hz. There are clearly several large craters (up to 100 μm across) surrounded by large regions of relatively smooth coating.

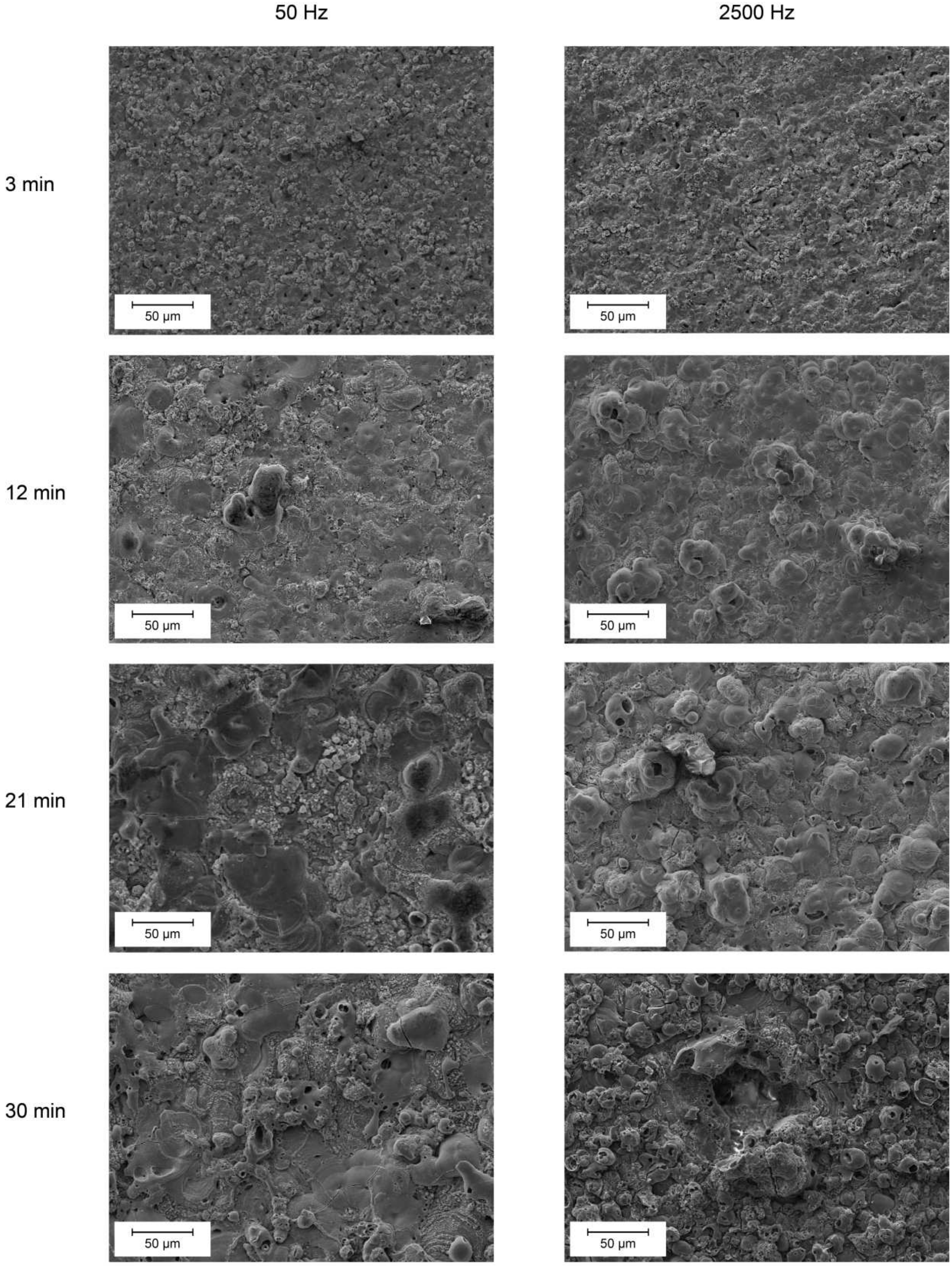

Figure 7.8 Micrographs showing the free surface of coatings formed on Al-1050 at 50 Hz and 2,500 Hz, for 3, 12, 21 and 30 minutes of PEO processing.

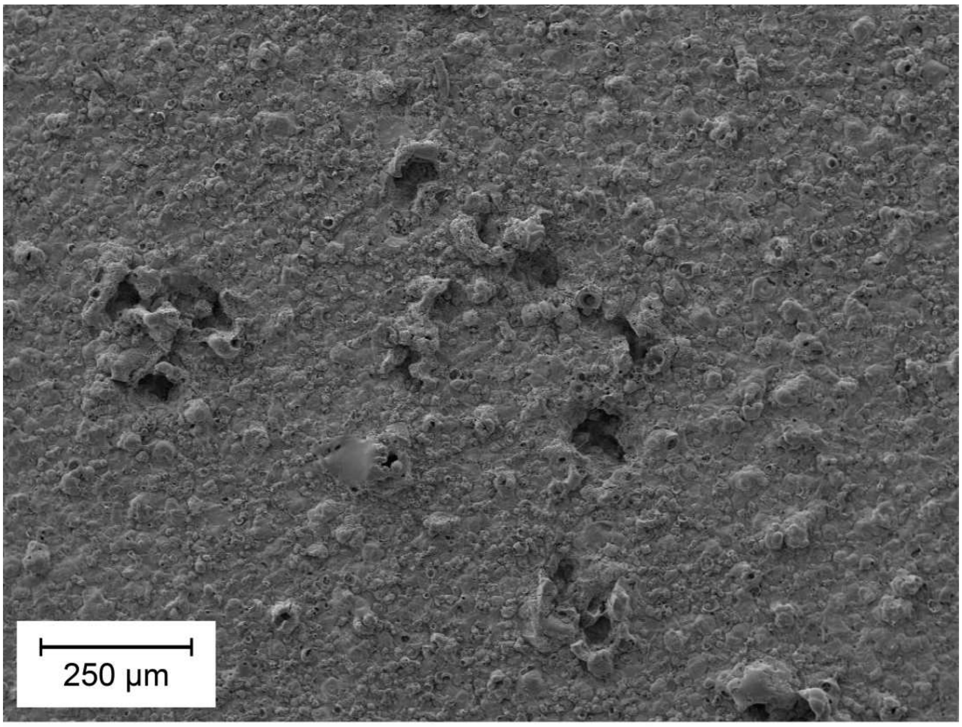

Figure 7.9 Low magnification micrograph of the free surface of a sample processed for 30 minutes at 2,500 Hz, showing several large craters surrounded by relatively smooth coating.

Figure 7.10 shows the cross-sections of coatings produced at 50 Hz and 2,500 Hz for various stages of PEO processing. At short processing times (3 minutes), the substrate coating interface is relatively smooth, and similar to an uncoated sample. The samples processed for 12 minutes appear very similar for both frequencies, with microcracks, sub-micron pores, and coarse pores (5–10 μm). Differences become more apparent at longer processing times, with the higher frequency samples appearing more homogenous and dense, and the lower frequency samples exhibiting an outer layer that not well bonded to the lower part of the coating.

Although large sections of the high frequency samples appeared to give an attractive microstructure, there were also some large-scale defects. Examples of such defects are shown in Figure 7.11. A large dip in the coating substrate interface can be seen, with an eruption of coating material above. These were open to the free surface and are likely to be the cross-sections of the craters seen in Figure 7.9. Additionally, cracks can be seen that penetrate right down to the substrate, which are likely to be detrimental to corrosion resistance. It seems likely that these craters were the result of cathodic discharges, quite possibly as a consequence of energetic, long-lived cascades. They form only under the conditions (high frequency, with relatively thick coatings) confirmed above as being those that are required in order to stimulate such cathodic discharges.

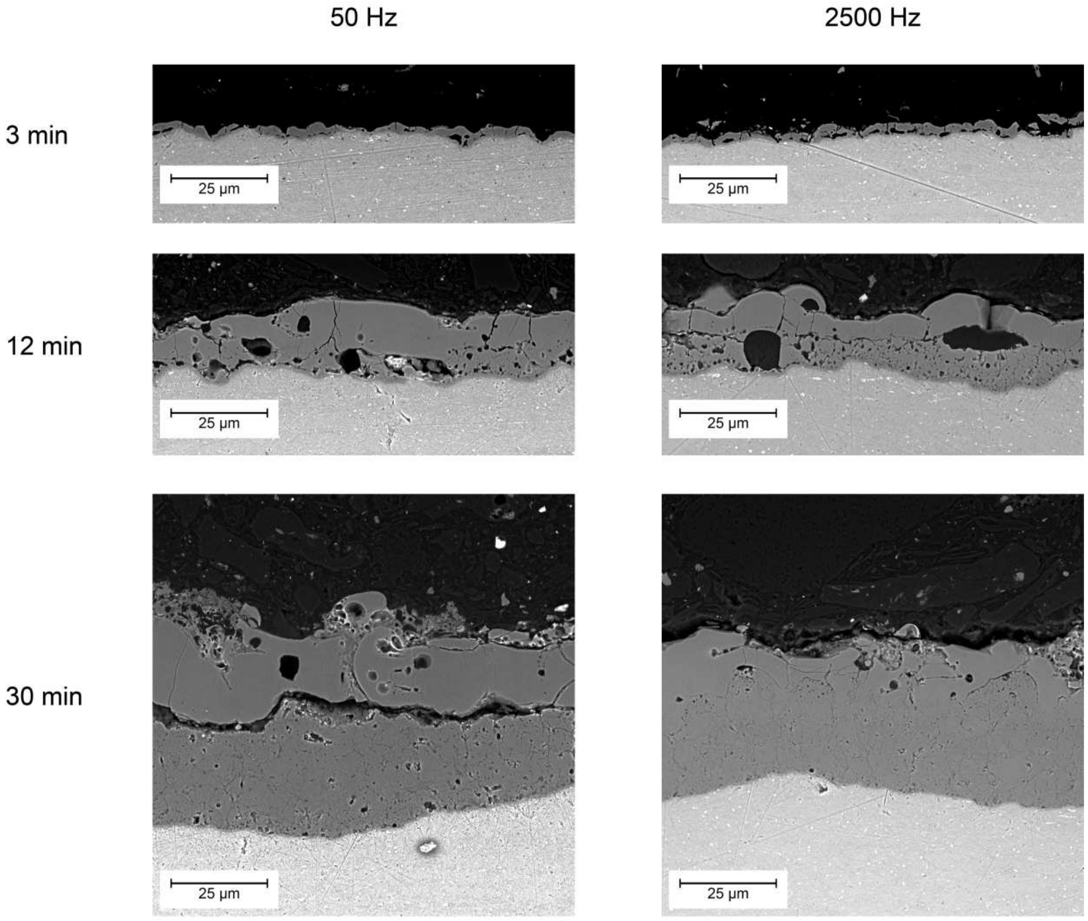

Figure 7.10 Micrographs showing the cross-sections of coatings formed on Al-1050 at 50 Hz and 2,500 Hz, for 3, 12, and 30 minutes of PEO processing.

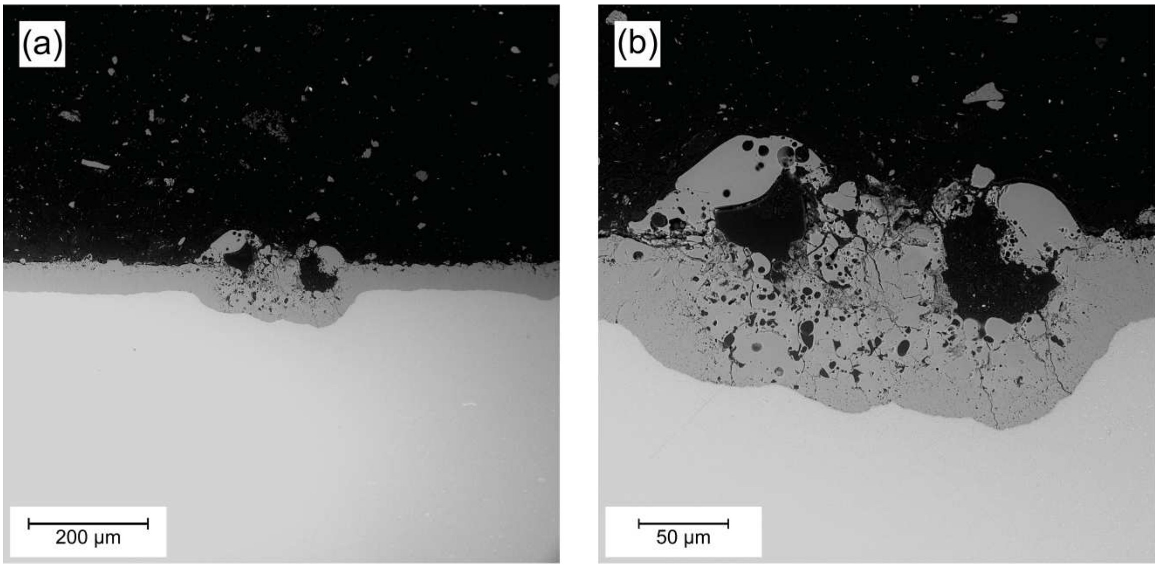

Figure 7.11 Micrographs showing examples of large craters in the cross-sections of samples processed at 2,500 Hz for 30 minutes at (a) low magnification, showing a large crater surrounded by a relatively homogenous coating, and (b) a higher magnification image of (a), where it can be seen that there are cracks penetrating through the coating all the way down to the substrate.

7.4 Gas evolution under different electrical regimes

Gas evolution is not routinely monitored during PEO processing, however, there are some limited studies outlined in §3.3. In the present work, only the gas evolution rates were measured, with no compositional analysis, which are of potential interest in considering the processes occurring during PEO. Two frequencies are considered, 50 Hz and 2,500 Hz. The experimental set-up is depicted in Figure 4.6. Two samples were processed in parallel, a shunt sample, and a monitoring sample. The gas is only collected from the monitoring sample, and the current flowing to the monitoring sample is measured.

The results of the gas evolution monitoring are shown in Figure 7.12, along with the mass gain of standard plate samples processed under similar conditions (i.e. the data presented in Figure 7.5). It can be seen that the gas evolution rate and mass gain is approximately constant throughout processing at 50 Hz supply frequency. However, at 2,500 Hz supply frequency the gas evolution rate follows the same trend as 50 Hz up until ~20 minutes of processing, where there is an abrupt change in gradient. This coincides with a change in gradient of the mass gain, for 2,500 Hz processing conditions, which actually levels off completely after ~25 minutes of processing. It can be seen that the gas evolution rates are significantly higher than the maximum electrochemical Faraday gas yield, indicated by the black dotted line, assuming all the current (taken to be 0.6 A) produces H_2 under cathodic polarisation, and O_2 under anodic polarisation.

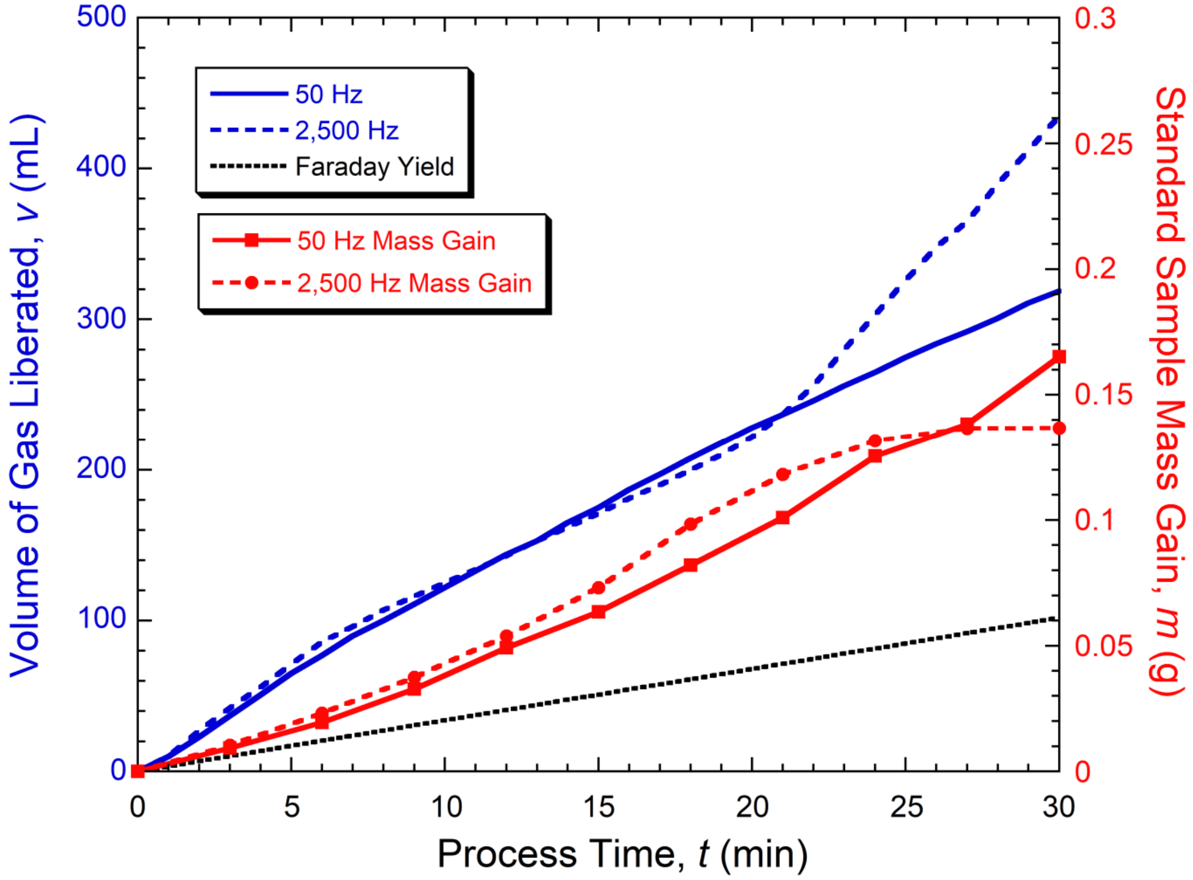

Figure 7.12 Plot showing the volume of gas liberated from the monitoring sample, and the mass gain of standard plate samples (processed individually) under similar conditions. The black dotted line shows the maximum electrochemical Faraday yield for a monitoring sample current of 0.6 A.

These results confirm previous reports that gas liberation during PEO exceeds the Faraday yield. Although the composition has not been measured, it is highly likely to be a mixture of H_2 and O_2 gas. Gas may be generated by, H_2 evolution under cathodic polarisation, a small amount of H_2 due to oxygen (from water molecules) combining with metal ions to form oxide, and a mixture of H_2 and O_2 gas from thermal decomposition of H_2O. Some simple calculations of the amounts of gas produced from potential sources are presented below.

For 50 Hz, with no cathodic discharges, it is likely that during the cathodic part of the cycle, all of the current is carried by hydrogen evolution on the sample. Assuming that this hydrogen is an ideal gas, the volume produced is

$$v_c = \frac{nRT}{P} \tag{11}$$

where R is the gas constant, T is the temperature of the gas, and P is the pressure of the gas and n is the number of moles of gas; which may be written as

$$n = \frac{I_c t}{4F} \tag{12}$$

where I_c is the average cathodic current through the sample, t is the process time and F is the Faraday constant. The factor of 4 comes from the cathodic half-cycle being 50% of the time, and one mole of e^- forms ½ mole of H_2 gas. It follows that

$$v_c = \frac{I_c tRT}{4FP} \tag{13}$$

During the 50 Hz run concerned, $I_c = 0.82$ A, and the temperature was ~22 °C (295 K). This gives, v_c ~90 mL, for 30 minutes of processing, assuming the pressure to be atmospheric (1 bar).

To produce the oxygen present in the coating, water must be decomposed, causing hydrogen gas to be released. Assuming that the coating is pure alumina, the volume of hydrogen gas, v_a, evolved in this way is given by

$$v_{\mathrm{a}} = \frac{nRT}{P} \tag{14}$$

with the number of moles now given by

$$n = \frac{\Delta m}{M_{\mathrm{r(Oxygen)}}} \tag{15}$$

where Δm is the mass gain of the monitoring sample and $M_{\mathrm{r(Oxygen)}}$ is the molecular weight of oxygen. The volume of gas produced in this way may be written as

$$v_{\mathrm{a}} = \frac{\Delta mRT}{M_{\mathrm{r(Oxygen)}}P} \tag{16}$$

For the 50 Hz case, after 30 minutes of processing, $\Delta m = 0.0126$ g, giving $v_{\mathrm{a}} = 19$ mL. The total amount of gas evolved during this run was $v_{\mathrm{total}} = 320$ mL, meaning this is a relatively small contribution.

The remainder of the gas evolved is likely to be produced via thermal decomposition of water molecules. Relatively large quantities of water do enter the plasma and become ionized during discharge formation. It is thermodynamically favourable to reform H_2O from these ions as the plasma collapses and cools. However, the transient nature of discharges, as well as the very high temperatures that are rapidly quenched, means there may simply be kinetic effects preventing full recombination of hydrogen and oxygen as the plasma cools and collapses.

The increased gas evolution rate at 2,500 Hz occurs around the same time as cathodic discharge start to occur. It therefore seems highly likely that the cathodic discharges were responsible for the increased gas evolution rate. As this transition occurs, the majority of the cathodic current will no longer be carried by hydrogen evolution, but rather as discharges in a similar manner to the anodic half-cycle. Simple calculations show that the gas is not being evolved in a purely electrochemical manner, and the discharges are the obvious source of this excessive gas evolution. There are no issues in terms of conservation of energy here, since the electrical power put into the

PEO process is large compared to the energy required to produce this volume of gas by thermal decomposition of H_2O molecules. The same mechanism (of water entering the plasma, becoming ionised and failing to recombine fully on cooling) is expected to operate for cathodic discharges as well as anodic ones. It follows that with discharges occurring during both half-cycles that the gas evolution rate should increase significantly, and, in fact, the gas evolution rate almost doubles after cathodic discharges start to occur.

7.5 Coating formation rates

Requiring explanation is the observed sharp drop in the rate of mass gain (i.e. the oxide formation rate) as cathodic discharges become common. It might have been expected that the oxide formation rate would rise (with oxide now being formed, via similar mechanisms, in both anodic and cathodic parts of the cycle). However, the observations made regarding the nature of the cathodic discharges must be taken into consideration. There are indications, such as the relatively high discharge currents in Figure 7.3, that cathodic discharges tend to be more energetic than anodic ones. This is consistent with the microstructural observations, with cathodic discharge sites, such as those in Figure 7.9, showing evidence of more violent events than those typical of anodic discharges. It certainly seems possible that, rather than new (molten) oxide being redistributed fairly smoothly around adjoining regions of the coating, as apparently happens during anodic discharges, cathodic discharges may result in much of this material, and possibly previously-formed oxide in the vicinity, being ejected into the electrolyte. This could give rise to almost any net rate of mass change, including the observed one of being close to zero.

It may also be noted that losing material in this way during individual discharges in a cascade sequence might be expected to prolong that cascade. New oxide formation normally leads eventually to the electrical resistance of the region rising sufficiently to terminate the cascade, but this mechanism would not operate effectively under these circumstances. This is something that it should be possible to confirm experimentally, although tracking an individual cascade through its complete lifetime is not simple, using either electrical or optical monitoring, because these cascade lifetimes tend to be very long on the scale of discharge lifetimes.

7.6 Summary

The information presented here from synchronised high-speed video and electrical monitoring, as well as microstructural observations and gas monitoring start to provide valuable information regarding the phenomena occurring during the cathodic half-cycle of PEO processing, and some of the effects of high frequency processing. As has been widely reported, during 50 Hz processing, discharges solely occur during the anodic half-cycle. The voltage during the cathodic half-cycle is substantially lower than for the anodic half-cycle, for the same imposed current density, and both polarities exhibit a gradual increase in voltage with processing time. This is due to asymmetry in the metal-oxide-electrolyte system rather than being causing by processing parameters. The increase is most likely caused by the increasing coating thickness. If breakdown occurs over a thin residual oxide layer at the base of a pore channel, then as the coating thickens, there is increased resistance from the column of electrolyte filling the pore channel.

High frequency processing leads to breakdown under cathodic polarisation. This only occurs after a certain processing time or coating thickness has been achieved, around 20 minutes with the present conditions. The cathodic voltage tends to increase at a much faster rate than at lower frequencies, up until cathodic discharges start. This implies the normal cathodic process, which is most likely to be hydrogen evolution, becomes more difficult at higher frequencies, which is a kinetic effect. At higher frequencies, there is less time for the H^+ ions to move, under the influence of the electric field, through the coating and reach the bottom of pore channels where they are discharged as hydrogen gas. As the coating thickens, there is a greater distance for the

H^+ ions to move, meaning a larger electric field is required to maintain the imposed current, hence the cathodic voltage rises. Once the electric field reaches a critical value, dielectric breakdown can occur and cathodic discharges are initiated, in a similar manner to anodic discharges. These cathodic discharges are able to carry the imposed current, instead of the conventional process of hydrogen evolution, meaning the cathodic voltage no longer needs to increase at such a fast rate. Interestingly, the gas evolution rate increases once cathodic discharges start. The cathodic process is no longer simply hydrogen evolution, so it might be expected that gas evolution should decrease. However, it is clear that the volume of gas liberated is well above the electrochemical Faraday yield. This means the discharges must be contributing to gas liberation in an alternative manner, most likely through thermal decomposition of water molecules into hydrogen and oxygen gas. Although thermodynamically favourable, there may not be sufficient time for recombination of the ions as the plasma is quenched. Therefore, as more discharges occur (during the cathodic half-cycle as well as the anodic half-cycle) the volume of gas liberated actually increases.

Thermodynamically there is no reason that cathodic discharges cannot contribute to oxide formation. A discharge simply exposes metallic substrate to an oxidising agent in the electrolyte (via a high temperature plasma), so they might regarded as beneficial. However, the mass gain of samples processed at high frequency actually levels off after cathodic discharges start. The cathodic discharges here tend to reach higher peak currents than anodic discharges and emit higher light intensity. The microstructural observations show that several large, deep craters in the sample surface have been generated by the cathodic discharges. This is perhaps unsurprising, given the significantly higher peak currents (and electrical energy) associated with cathodic discharges, compared to anodic discharges, making them particularly violent. Coating material is likely to be blasted off the surface by such discharges, leaving behind large craters and preventing further mass gain. Of course, anodic discharges may subsequently occur in these “damaged” regions to re-grow a thick oxide layer, or the cathodic discharges may also be generating oxide material, but these large craters are unlikely to be an attractive feature of a PEO coating. Cracks can be seen to penetrate right through to the substrate material, which would lead to poor corrosion resistance. However, there do appear to be some benefits of the high frequency processing. The cross sections of high frequency coatings, between the large craters, appear be to more homogenous and dense, than equivalent coatings produced at 50 Hz. There may be potential benefits to producing coatings at these high frequencies if the damaging cathodic discharges can be avoided or their intensity reduced.

Chapter 8

Conclusions

8.1 Characteristics of discharge events

Characteristics of individual discharge events on aluminium have been investigated in the present work using a combination of experimental techniques. High-speed video monitoring, synchronised with electrical measurements, gas evolution studies, and microstructural examinations have elucidated a number of features of the PEO process, which include:

a) Individual discharges have a strong tendency to occur in sequences termed "cascades", at well-defined physical locations, which was confirmed by high-speed photography. Previously established electrical characteristics, such as typical lifetimes and incubation periods between discharges within a cascade, were verified by high-speed photography, along with their evolution with coating thickness.

b) Cascades persist at particular locations over multiple cycles of the applied potential, particularly for thicker coatings. The number of discharges in a cascade has been observed to run into many hundreds (for a cascade that was still active), although it is likely that the true number may be into the thousands.

c) The microstructural effects of a discharge cascade are confined to an approximately circular region, a few tens of microns in diameter, centred on a discharge channel. The discharge channel extends almost through the entire coating thickness to the substrate, where there is a thin oxide layer, which was shown by tomography of an active discharge channel.

d) Discharges persist in the same location, even if the PEO process is interrupted, the sample removed, dried, and replaced in the electrolyte before the process is restarted. This strongly suggests that it is residual microstructural features, particularly the pore channels, that are ensuring that the cascade persists in the same location, rather than short term effects such as residual thermal or electrical fields.

e) The ignition of a discharge, and creation of a plasma channel through the thickness of the coating, is quickly followed by formation and growth of a large hemi-spherical gas bubble, centred on the plasma channel.

f) This bubble grows rapidly, typically reaching a radius of about 500 μm during the lifetime of the discharge. It seems likely that this bubble growth is responsible for a sharp increase in the electrical resistance of the current path, leading to the current shutting off. From the observed rate of growth of the bubble, it is concluded that the peak over-pressure within it is relatively low (of the order of 1 atmosphere).

g) These features indicate that the sequence of events occurring during a discharge cascade is as follows;

   i) The discharge is initiated by dielectric breakdown across the oxide layer at the base of the pore channel.

   ii) A high temperature plasma forms, currents starts to flow and Joule heating occurs.

  iii) Metallic substrate atoms are exposed to oxidising agents from the electrolyte in the plasma. A gas bubble forms above the discharge channel, which expands and causes the electrical resistance to increase. This in turn causes the current to shut off, and the plasma to cool and collapse.

  iv) New oxide material condenses in the surrounding regions of the discharge channel. The bubble shrinks as water vapour condenses, heating up the surrounding electrolyte.

  v) The pore channel refills with electrolyte, and the process starts again.

h) During high frequency power supply regimes, discharges can occur under cathodic polarisation. These discharges tend to be violent (higher energy than anodic discharges, with more light emission), and cause large craters to form in the coating.

i) Cathodic discharges are likely to be caused by the higher cathodic applied potentials, which are established to maintain a set current density, at high frequency compared with low frequency processing. This is a kinetic effect, most likely related to the mobility of hydrogen and hydroxyl ions through the electrolyte within the pores on the coating.

j) Gas evolution rates are significantly above the electrochemical Faraday yield. This strongly suggests another mechanism of gas evolution, related to discharges, is occurring, such as thermal decomposition of water molecules. Once cathodic discharges start, the gas evolution rate increases significantly, providing further evidence that the discharges are responsible for the excessive gas evolution.

8.2 Energetics of individual discharges

It is noted that energy consumption during the PEO process is relatively high. Improved understanding of discharge characteristics may point the way towards promising measures to reduce this. The information presented from synchronised current monitoring and high-speed video imaging of individual discharges formed during PEO processing at 50 Hz AC allows the following conclusions to be drawn:

a) An order of magnitude estimate relating to substrate oxidation associated with individual discharges is ~10^{13}–10^{14} J m^{-3}.

b) Estimates of the aggregate discharge energy involved in a cascade of, say, 1,000 discharges, and the relationship between this and the volume of oxide created provides some understanding of why cascades persist for extended sequences. The associated increase in the average coating thickness of a 100 μm diameter circular area is ~5 μm., which is moderate increase if the coating is already 100 μm thick. Eventually, this process presumably raises the electrical resistance of the region sufficiently for the cascade concerned to shut down.

c) It is deduced that the bubble growth at the top of a discharge channel occurs as a consequence of the rapid volatilisation of a large quantity of water (electrolyte), which remains at relatively low temperature and pressure as bubble expansion occurs. Once the discharge current has been shut off, the bubble contracts rapidly as this water vapour condenses, releasing most of the energy of the discharge into the bulk of the electrolyte and raising its temperature.

d) A semi-quantitative audit has been carried out concerning the injected electrical energy and its transformation between the forms represented by the existence of the plasma, the melting and volatilisation of substrate and coating, the vaporisation of water to create the bubble and the heating of the bulk electrolyte.

8.3 Future work

There is significant scope for work relating to understanding the fundamentals of the PEO process. The exact mechanisms of discharge cascade initiation and termination are yet to be fully understood, and should be the focus of further investigations. Some of the techniques used here would provide a useful tool for such investigations, and could be supplemented by additional techniques, for example, time-resolved optical emission spectroscopy to determine the evolution of the electron temperatures and densities within a discharge plasma.

Accurate measurement of the gas composition evolved during PEO processing would be very useful to verify the source of the excessive gas yield. For example, the gas composition would be expected to change when the cathodic process switches from hydrogen evolution to cathodic discharges carrying the cathodic current.

Further investigations of the microstructural effects of high frequency processing would be beneficial, including varying the duty cycle and current delivered during each half-cycle. There is some limited evidence that high frequency processing could provide an attractive coating microstructure (dense and homogeneous), but only if powerful cathodic discharges can be avoided.

List of Publications

The work of this thesis is based on the following publications:

SC Troughton & TW Clyne *Cathodic Discharges During High Frequency Plasma Electrolytic Oxidation*. Surface and Coatings Technology, 2018. **352**: p. 591–599.

TW Clyne & SC Troughton *A review of recent work on discharge characteristics during plasma electrolytic oxidation of various metals*. International Materials Reviews, 2018. p. 1–36.

SC Troughton, A Nominé, J Dean & TW Clyne *Effect of individual discharge cascades on the microstructure of plasma electrolytic oxidation coatings*. Applied Surface Science, 2016. **389**: p. 260–269.

SC Troughton, A Nominé, AV Nominé, G Henrion & TW Clyne *Synchronised electrical monitoring and high-speed video of bubble growth associated with individual discharges during plasma electrolytic oxidation*. Applied Surface Science, 2015. **359**: p. 405–411.

A Nominé, SC Troughton, AV Nominé, G Henrion & TW Clyne *High speed video evidence for localised discharge cascades during plasma electrolytic oxidation*. Surface and Coatings Technology, 2015. **269**: p. 125–130.

Other related publications:

M Coto, SC Troughton, J Duan, RV Kumar & TW Clyne *Development and assessment of photo-catalytic membranes for water purification using solar radiation*. Applied Surface Science, 2018. **433**: p. 101–107.

References

1. Sabatini, G, L Ceschini, C Martini, JA Williams, and IM Hutchings, *Improving sliding and abrasive wear behaviour of cast A356 and wrought AA7075 aluminium alloys by plasma electrolytic oxidation.* Materials & Design, 2010. **31**(2): p. 816-828.
2. Cheng, YL, JH Cao, ZM Peng, Q Wang, E Matykina, P Skeldon, and GE Thompson, *Wear-resistant coatings formed on Zircaloy-2 by plasma electrolytic oxidation in sodium aluminate electrolytes.* Electrochimica Acta, 2014. **116**: p. 453-466.
3. Li, QB, J Liang, BX Liu, ZJ Peng, and Q Wang, *Effects of cathodic voltages on structure and wear resistance of plasma electrolytic oxidation coatings formed on aluminium alloy.* Applied Surface Science, 2014. **297**: p. 176-181.
4. Ma, C, M Zhang, Y Yuan, X Jing, and X Bai, *Tribological behavior of plasma electrolytic oxidation coatings on the surface of Mg8Li1Al alloy.* Tribology International, 2012. **47**: p. 62-68.
5. Treviño, M, NF Garza-Montes-de-Oca, A Párez, MAL Hernández-Rodíguez, A Juárez, and R Colás, *Wear of an aluminium alloy coated by plasma electrolytic oxidation.* Surface and Coatings Technology, 2012. **206**(8-9): p. 2213-2219.
6. Khorasanian, M, A Dehghan, MH Shariat, ME Bahrololoom, and S Javadpour, *Microstructure and wear resistance of oxide coatings on Ti-6Al-4V produced by plasma electrolytic oxidation in an inexpensive electrolyte.* Surface and Coatings Technology, 2011. **206**(6): p. 1495-1502.
7. Aliofkhazraei, M, A Sabour Rouhaghdam, and T Shahrabi, *Abrasive wear behaviour of Si_3N_4/TiO_2 nanocomposite coatings fabricated by plasma electrolytic oxidation.* Surface and Coatings Technology, 2010. **205**(Supplement 1): p. S41-S46.
8. Martini, C, L Ceschini, F Tarterini, JM Paillard, and JA Curran, *PEO layers obtained from mixed aluminate–phosphate baths on Ti–6Al–4V: Dry sliding behaviour and influence of a PTFE topcoat.* Wear, 2010. **269**(11–12): p. 747-756.
9. Wasekar, NP, A Jyothirmayi, LR Krishna, and G Sundararajan, *Effect of micro arc oxidation coatings on corrosion resistance of 6061-Al alloy.* Journal of Materials Engineering and Performance, 2008. **17**(5): p. 708-713.

10. Zhendong, W, J Zhaohua, Y Zhongping, W Zhijiang, and Z Xuelin, *Study on structure and corrosion resistance of micro arc oxidation black ceramic coatings on aluminum alloy.* Rare Metal Materials and Engineering, 2007. **36**: p. 687-689.
11. Fatimah, S, MP Kamil, JH Kwon, M Kaseem, and YG Ko, *Dual incorporation of SiO2 and ZrO2 nanoparticles into the oxide layer on 6061 Al alloy via plasma electrolytic oxidation: Coating structure and corrosion properties.* Journal of Alloys and Compounds, 2017. **707**: p. 358-364.
12. Xu, L, JN Ding, XJ Xu, XY Niu, BQ Li, and GG Cheng, *Wettability and Corrosion Resistance of Ultrafine-Grained Titanium by Micro-arc Oxidation.* Rare Metal Materials and Engineering, 2015. **44**(12): p. 3100-3104.
13. Hwang, DY, YM Kim, DY Park, B Yoo, and DH Shin, *Corrosion resistance of oxide layers formed on AZ91 Mg alloy in KMnO4 electrolyte by plasma electrolytic oxidation.* Electrochimica Acta, 2009. **54**(23): p. 5479-5485.
14. Malayoglu, U, KC Tekin, and S Shrestha, *Influence of post-treatment on the corrosion resistance of PEO coated AM50B and AM60B Mg alloys.* Surface and Coatings Technology, 2010. **205**(6): p. 1793-1798.
15. Hussein, RO, DO Northwood, and X Nie, *The effect of processing parameters and substrate composition on the corrosion resistance of plasma electrolytic oxidation (PEO) coated magnesium alloys.* Surface and Coatings Technology, 2013. **237**: p. 357-368.
16. Mori, Y, A Koshi, J Liao, H Asoh, and S Ono, *Characteristics and corrosion resistance of plasma electrolytic oxidation coatings on AZ31B Mg alloy formed in phosphate - Silicate mixture electrolytes.* Corrosion Science, 2014. **88**: p. 254-262.
17. Krishna, LR, G Poshal, and G Sundararajan, *Influence of Electrolyte Chemistry on Morphology and Corrosion Resistance of Micro Arc Oxidation Coatings Deposited on Magnesium.* Metallurgical and Materials Transactions a-Physical Metallurgy and Materials Science, 2010. **41A**(13): p. 3499-3508.
18. Dicu, M, A Matei, M Abrudeanu, and C Ducu, *Synthesis and properties of the porous titania coatings formed on titanium by plasma electrolytic oxidation for biomedical application.* Journal of Optoelectronics and Advanced Materials, 2011. **13**(3): p. 324-331.
19. Koegler, WS and LG Griffith, *Osteoblast response to PLGA tissue engineering scaffolds with PEO modified surface chemistries and demonstration of patterned cell response.* Biomaterials, 2004. **25**(14): p. 2819-2830.
20. Whiteside, P, E Matykina, JE Gough, P Skeldon, and GE Thompson, *In vitro evaluation of cell proliferation and collagen synthesis on titanium following plasma electrolytic oxidation.* Journal of Biomedical Materials Research - Part A, 2010. **94**(1): p. 38-46.
21. Robinson, HJ, AE Markaki, CA Collier, and TW Clyne, *Cell adhesion to plasma electrolytic oxidation (PEO) titania coatings, assessed using a centrifuging technique.* Journal of the Mechanical Behavior of Biomedical Materials, 2011. **4**(8): p. 2103-2112.

22. Siu, HT and HC Man, *Fabrication of bioactive titania coating on nitinol by plasma electrolytic oxidation.* Applied Surface Science, 2013. **274**(0): p. 181-187.
23. Hornberger, H, S Virtanen, and AR Boccaccini, *Biomedical coatings on magnesium alloys - A review.* Acta Biomaterialia, 2012. **8**(7): p. 2442-2455.
24. Mohedano, M, BJC Luthringer, B Mingo, F Feyerabend, R Arrabal, PJ Sanchez-Egido, C Blawert, R Willumeit-Romer, ML Zheludkevich, and E Matykina, *Bioactive plasma electrolytic oxidation coatings on Mg-Ca alloy to control degradation behaviour.* Surface and Coatings Technology, 2017. **315**: p. 454-467.
25. Tang, H, Y Han, T Wu, W Tao, X Jian, YF Wu, and FJ Xu, *Synthesis and properties of hydroxyapatite-containing coating on AZ31 magnesium alloy by micro-arc oxidation.* Applied Surface Science, 2017. **400**: p. 391-404.
26. Yao, ZP, LL Li, and ZH Jiang, *Adjustment of the ratio of Ca/P in the ceramic coating on Mg alloy by plasma electrolytic oxidation.* Applied Surface Science, 2009. **255**(13-14): p. 6724-6728.
27. Gu, XN, N Li, WR Zhou, YF Zheng, X Zhao, QZ Cai, and LQ Ruan, *Corrosion resistance and surface biocompatibility of a microarc oxidation coating on a Mg-Ca alloy.* Acta Biomaterialia, 2011. **7**(4): p. 1880-1889.
28. Zhang, L, JQ Zhang, CF Chen, and YH Gu, *Advances in microarc oxidation coated AZ31 Mg alloys for biomedical applications.* Corrosion Science, 2015. **91**: p. 7-28.
29. Akpan, UG and BH Hameed, *Parameters affecting the photocatalytic degradation of dyes using TiO_2-based photocatalysts: A review.* Journal of Hazardous Materials, 2009. **170**(2-3): p. 520-529.
30. Awazu, K, M Fujimaki, C Rockstuhl, J Tominaga, H Murakami, Y Ohki, N Yoshida, and T Watanabe, *A plasmonic photocatalyst consisting of sliver nanoparticles embedded in titanium dioxide.* Journal of the American Chemical Society, 2008. **130**(5): p. 1676-1680.
31. Shin, YK, WS Chae, YW Song, and YM Sung, *Formation of titania photocatalyst films by microarc oxidation of Ti and Ti–6Al–4V alloys.* Electrochemistry Communications, 2006. **8**(3): p. 465–470.
32. Akatsu, T, Y Yamada, Y Hoshikawa, T Onoki, Y Shinoda, and F Wakai, *Multifunctional porous titanium oxide coating with apatite forming ability and photocatalytic activity on a titanium substrate formed by plasma electrolytic oxidation.* Materials Science & Engineering C-Materials for Biological Applications, 2013. **33**(8): p. 4871-4875.
33. He, J, Q Luo, QZ Cai, XW Li, and DQ Zhang, *Microstructure and photocatalytic properties of WO_3/ TiO_2 composite films by plasma electrolytic oxidation.* Materials Chemistry and Physics, 2011. **129**(1-2): p. 242-248.
34. Bayati, MR, F Golestani-Fard, and AZ Moshfegh, *How photocatalytic activity of the MAO-grown TiO_2 nano/micro-porous films is influenced by growth parameters?* Applied Surface Science, 2010. **256**(13): p. 4253-4259.
35. Mizukoshi, Y, N Ohtsu, S Semboshi, and N Masahashi, *Visible light responses of sulfur-doped rutile titanium dioxide photocatalysts fabricated by anodic oxidation.* Applied Catalysis B: Environmental, 2009. **91**(1-2): p. 152-156.

36. Oh, H-J and C-S Chi, *Eu–N-doped TiO_2 photocatalyst synthesized by micro-arc oxidation.* Materials Letters, 2012. **86**: p. 31-33.
37. Coto, M, SC Troughton, J Duan, RV Kumar, and TW Clyne, *Development and assessment of photo-catalytic membranes for water purification using solar radiation.* Applied Surface Science, 2018. **433**: p. 101-107.
38. Luttrell, TH, S; Tao, J; Kramer, A; Sutter, E; Batzill, M, *Why is anatase a better photocatalyst than rutile? - Model studies on epitaxial TiO_2.* Scientific Reports, 2014. **4**: p. 4043.
39. Mirelman, LK, JA Curran, and TW Clyne, *The Production of Anatase-rich Photoactive Coatings by Plasma Electrolytic Oxidation.* Surface and Coatings Technology, 2012. **207**: p. 66-71.
40. Xin, SG, LX Song, RG Zhao, and XF Hu, *Influence of cathodic current on composition, structure and properties of Al2O3 coatings on aluminum alloy prepared by micro-arc oxidation process.* Thin Solid Films, 2006. **515**(1): p. 326-332.
41. Matykina, E, R Arrabal, M Mohedano, B Mingo, J Gonzalez, A Pardo, and MC Merino, *Recent advances in energy efficient PEO processing of aluminium alloys.* Transactions of Nonferrous Metals Society of China, 2017. **27**(7): p. 1439-1454.
42. Curran, JA, *Thermal and Mechanical Properties of Plasma Electrolytic Oxide Coatings*, in *A dissertation submitted for the Degree of Doctor of Philosophy, University of Cambridge*2005.
43. Martin, J, A Melhem, I Shchedrina, T Duchanoy, A Nomine, G Henrion, T Czerwiec, and T Belmonte, *Effects of electrical parameters on plasma electrolytic oxidation of aluminium.* Surface and Coatings Technology, 2013. **221**: p. 70-76.
44. Yerokhin, AL, A Shatrov, V Samsonov, P Shashkov, A Pilkington, A Leyland, and A Matthews, *Oxide ceramic coatings on aluminium alloys produced by a pulsed bipolar plasma electrolytic oxidation process.* Surface and Coatings Technology, 2005. **199**(2-3): p. 150-157.
45. Jaspard-Mécuson, F, T Czerwiec, G Henrion, T Belmonte, L Dujardin, A Viola, and J Beauvir, *Tailored aluminium oxide layers by bipolar current adjustment in the Plasma Electrolytic Oxidation (PEO) process.* Surface and Coatings Technology, 2007. **201**(21): p. 8677-8682
46. Hussein, RO, X Nie, and DO Northwood, *Influence of process parameters on electrolytic plasma discharging behaviour and aluminum oxide coating microstructure.* Surface and Coatings Technology, 2010. **205**(6): p. 1659-1667.
47. Dunleavy, CS, IO Golosnoy, JA Curran, and TW Clyne, *Characterisation of discharge events during plasma electrolytic oxidation.* Surface and Coatings Technology, 2009. **203**(22): p. 3410–3419.
48. Stojadinovic, S, R Vasilic, M Petkovic, Z Nedic, B Kasalica, I Belca, and L Zekovic, *Luminescence properties of oxide films formed by anodization of aluminum in 12-tungstophosphoric acid.* Electrochimica Acta, 2010. **55**(12): p. 3857-3863.

49. Stojadinović, S, R Vasilić, M Petković, and L Zeković, *Plasma electrolytic oxidation of titanium in heteropolytungstate acids.* Surface and Coatings Technology, 2011. **206**(2–3): p. 575-581.
50. Petković, M, S Stojadinović, R Vasilić, and L Zeković, *Characterization of oxide coatings formed on tantalum by plasma electrolytic oxidation in 12-tungstosilicic acid.* Applied Surface Science, 2011. **257**(24): p. 10590-10594.
51. Matykina, E, R Arrabal, P Skeldon, and GE Thompson, *Transmission electron microscopy of coatings formed by plasma electrolytic oxidation of titanium.* Acta Biomaterialia, 2009. **5**(4): p. 1356-1366.
52. Rogov, AB and VR Shayapov, *The role of cathodic current in PEO of aluminum: Influence of cationic electrolyte composition on the transient current-voltage curves and the discharges optical emission spectra.* Applied Surface Science, 2017. **394**: p. 323-332.
53. Venkateswarlu, K, N Rameshbabu, D Sreekanth, M Sandhyarani, AC Bose, V Muthupandi, and S Subramanian, *Role of electrolyte chemistry on electronic and in vitro electrochemical properties of micro-arc oxidized titania films on Cp Ti.* Electrochimica Acta, 2013. **105**: p. 468-480.
54. Simchen, F, M Sieber, and T Lampke, *Electrolyte influence on ignition of plasma electrolytic oxidation processes on light metals.* Surface and Coatings Technology, 2017. **315**: p. 205-213.
55. Yerokhin, AL, X Nie, A Leyland, A Matthews, and SJ Dowey, *Plasma electrolysis for surface engineering (Review).* Surface and Coatings Technology, 1999. **122**(2-3): p. 73-93.
56. Walsh, FC, CTJ Low, RJK Wood, KT Stevens, J Archer, AR Poeton, and A Ryder, *Plasma electrolytic oxidation (PEO) for production of anodised coatings on lightweight metal (Al, Mg, Ti) alloys.* Transactions of the Institute of Metal Finishing, 2009. **87**(3): p. 122-135.
57. Jiang, YL, JK Wang, B Hu, ZP Yao, QX Xia, and ZH Jiang, *Preparation of a novel yellow ceramic coating on Ti alloys by plasma electrolytic oxidation.* Surface and Coatings Technology, 2016. **307**: p. 1297-1302.
58. Wang, S and PC Liu, *The technology of preparing green coating by conducting micro-arc oxidation on AZ91D magnesium alloy.* Polish Journal of Chemical Technology, 2016. **18**(4): p. 36-40.
59. Yang, W, JL Wang, DP Xu, JH Li, and T Chen, *Characterization and formation mechanism of grey micro-arc oxidation coatings on magnesium alloy.* Surface and Coatings Technology, 2015. **283**: p. 281-285.
60. Shao, ZC, QF Zhang, L Yang, M Wang, and H Gao, *Preparation of Dark-Red Membrane by Micro-Arc Oxidation on AM50 Alloys.* Materials and Manufacturing Processes, 2015. **30**(12): p. 1505-1509.
61. Wang, ZJ, XY Nie, H Hu, and RO Hussein, *In situ fabrication of blue ceramic coatings on wrought Al Alloy 2024 by plasma electrolytic oxidation.* Journal of Vacuum Science & Technology A, 2012. **30**(2).

62. Dou, Q, WF Li, GG Zhang, and XF Wan, *Preparation and characterisation of black ceramic coating on AZ91D magnesium alloy by plasma electrolytic oxidation with reduced energy consumption.* Materials Research Innovations, 2015. **19**.
63. Hwang, IJ, KR Shin, JS Lee, YG Ko, and DH Shin, *Formation of black ceramic layer on aluminum alloy by plasma electrolytic oxidation in electrolyte containing Na 2WO 4.* Materials Transactions, 2012. **53**(3): p. 559-564.
64. Li, K, WF Li, GG Zhang, and P Guo, *Preparation of black PEO layers on Al-Si alloy and the colorizing analysis.* Vacuum, 2015. **111**: p. 131-136.
65. Martin, J, P Leone, A Nomine, D Veys-Renaux, G Henrion, and T Belmonte, *Influence of electrolyte ageing on the Plasma Electrolytic Oxidation of aluminium.* Surface and Coatings Technology, 2015. **269**: p. 36-46.
66. Lu, XP, M Mohedano, C Blawert, E Matykina, R Arrabal, KU Kainer, and ML Zheludkevich, *Plasma electrolytic oxidation coatings with particle additions - A review.* Surface and Coatings Technology, 2016. **307**: p. 1165-1182.
67. Arrabal, R, E Matykina, P Skeldon, and GE Thompson, *Incorporation of zirconia particles into coatings formed on magnesium by plasma electrolytic oxidation.* Journal of Materials Science, 2008. **43**(5): p. 1532-1538.
68. Li, HX, WJ Li, RG Song, and ZG Ji, *Effects of different current densities on properties of MAO coatings embedded with and without a-Al2O3 nanoadditives.* Materials Science and Technology, 2012. **28**(5): p. 565-568.
69. Lu, XP, C Blawert, KU Kainer, and ML Zheludkevich, *Investigation of the formation mechanisms of plasma electrolytic oxidation coatings on Mg alloy AM50 using particles.* Electrochimica Acta, 2016. **196**: p. 680-691.
70. Lu, XP, C Blawert, YD Huang, H Ovri, ML Zheludkevich, and KU Kainer, *Plasma electrolytic oxidation coatings on Mg alloy with addition of SiO2 particles.* Electrochimica Acta, 2016. **187**: p. 20-33.
71. Wang, P, T Wu, YT Xiao, J Pu, M Xu, CL Xiang, and XY Guo, *Effects of Al2O3 Micro Powder Addition Amount on Characteristics of Micro-arc Oxidation Coating Formed on Magnesium Alloy.* Rare Metal Materials and Engineering, 2017. **46**(5): p. 1260-1264.
72. Sundararajan, G and L Rama Krishna, *Mechanisms Underlying the Formation of Thick Alumina Coatings through the MAO Coating Technology.* Surface and Coatings Technology, 2003. **167**: p. 269-277.
73. Curran, JA and TW Clyne, *Thermo-physical Properties of Plasma Electrolytic Oxide Coatings on Aluminium.* Surface and Coatings Technology, 2005. **199**(2-3): p. 168-176.
74. Dunleavy, CS, JA Curran, and TW Clyne, *Time dependent statistics of plasma discharge parameters during bulk AC plasma electrolytic oxidation of aluminium.* Applied Surface Science, 2013. **268**(0): p. 397-409.
75. Monfort, F, A Berkani, E Matykina, P Skeldon, GE Thompson, H Habazaki, and K Shimizu, *Development of anodic coatings on aluminium under sparking conditions in silicate electrolyte.* Corrosion Science, 2007. **49**: p. 672–693.

76. Curran, JA, H Kalkanci, Y Magurova, and TW Clyne, *Mullite-rich plasma electrolytic oxide coatings for thermal barrier applications.* Surface and Coatings Technology, 2006. **201**(21): p. 8683-8687.
77. Dunleavy, CS, JA Curran, and TW Clyne, *Self-similar scaling of discharge events through PEO coatings on aluminium.* Surface and Coatings Technology, 2011. **206**(6): p. 1051-1061.
78. Mécuson, F, T Czerwiec, T Belmonte, L Dujardin, A Viola, and G Henrion, *Diagnostics of an electrolytic microarc process for aluminium alloy oxidation.* Surface and Coatings Technology, 2005. **200**(1-4): p. 804-808.
79. Tillous, EK, T Toll-Duchanoy, and E Bauer-Grosse, *Microstructure and 3D microtomographic characterization of porosity of MAO surface layers formed on aluminium and 2214-T6 alloy.* Surface and Coatings Technology, 2009. **203**(13): p. 1850-1855.
80. Arrabal, R, E Matykina, T Hashimoto, P Skeldon, and GE Thompson, *Characterization of AC PEO coatings on magnesium alloys.* Surface and Coatings Technology, 2009. **203**: p. 2207-2220.
81. Nie, X, E Meletis, J Jiang, A Leyland, A Yerokhin, and A Matthews, *Abrasive wear/corrosion properties and TEM analysis of Al2O3 coatings fabricated using plasma electrolysis.* Surface and Coating Technology, 2002. **149**: p. 245-251.
82. Tillous, K, T Toll-Duchanoy, E Bauer-Grosse, L Hericher, and G Geandier, *Microstructure and phase composition of microarc oxidation surface layers formed on aluminium and its alloys 2214-T6 and 7050-T74.* Surface and Coatings Technology, 2009. **203**(19): p. 2969-2973.
83. Curran, JA and TW Clyne, *Porosity in plasma electrolytic oxide coatings.* Acta Materialia, 2006. **54**(7): p. 1985-1993.
84. Zhang, X, S Aliasghari, A Nemcova, TL Burnett, I Kubena, M Smid, GE Thompson, P Skeldon, and PJ Withers, *X-ray Computed Tomographic Investigation of the Porosity and Morphology of Plasma Electrolytic Oxidation Coatings.* Acs Applied Materials & Interfaces, 2016. **8**(13): p. 8801-8810.
85. Dean, J, T Gu, and TW Clyne, *Evaluation of Residual Stress Levels in Plasma Electrolytic Oxidation Coatings using a Curvature Method.* Surface and Coatings Technology, 2015. **269**: p. 47-53.
86. Lee, JH and SJ Kim, *Effects of silicate ion concentration on the formation of ceramic oxide layers produced by plasma electrolytic oxidation on Al alloy.* Japanese Journal of Applied Physics, 2017. **56**(1).
87. Javidi, M and H Fadaee, *Plasma electrolytic oxidation of 2024-T3 aluminum alloy and investigation on microstructure and wear behavior.* Applied Surface Science, 2013. **286**: p. 212-219.
88. Xin, SG, LX Song, RG Zhao, and XF Hu, *Phase composition and properties of the micro-arc oxidation coating on aluminium matrix composite.* Journal of Inorganic Materials, 2006. **21**(1): p. 223-229.

89. Friedemann, AER, TM Gesing, and P Plagemann, *Electrochemical rutile and anatase formation on PEO surfaces.* Surface and Coatings Technology, 2017. **315**: p. 139-149.
90. Ao, N, DX Liu, SX Wang, Q Zhao, XH Zhang, and MM Zhang, *Microstructure and Tribological Behavior of a TiO2/hBN Composite Ceramic Coating Formed via Micro-arc Oxidation of Ti-6Al-4V Alloy.* Journal of Materials Science and Technology, 2016. **32**(10): p. 1071-1076.
91. Yerokhin, AL, A Leyland, and A Matthews, *Kinetic aspects of Aluminium Titanate layer formation on Titanium Alloys by Plasma Electrolytic Oxidation.* Applied Surface Science, 2002. **200**(1-4): p. 172-184.
92. Yao, ZP, YF Liu, YJ Xu, ZH Jiang, and FP Wang, *Effects of cathode pulse at high frequency on structure and composition of Al2TiO5 ceramic coatings on Ti alloy by plasma electrolytic oxidation.* Materials Chemistry and Physics, 2011. **126**(1-2): p. 227-231.
93. Matykina, E, R Arrabal, DJ Scurr, A Baron, P Skeldon, and GE Thompson, *Investigation of the mechanism of plasma electrolytic oxidation of aluminium using O-18 tracer.* Corrosion Science, 2010. **52**(3): p. 1070-1076.
94. Monfort, F, A Berkani, E Matykina, P Skeldon, GE Thompson, H Habazaki, and K Shimizuc, *A Tracer Study of Oxide Growth during Spark Anodizing of Aluminum.* Journal of The Electrochemical Society, 2005. **152**(6): p. C382-C387.
95. Stojadinovic, S, R Vasilic, and M Peric, *Investigation of plasma electrolytic oxidation on valve metals by means of molecular spectroscopy - a review.* Rsc Advances, 2014. **4**(49): p. 25759-25789.
96. Michaelis, A, *Valve Metal, Si and Ceramic Oxides as Dielectric Films for Passive and Active Electronic Devices*, in *Advances in Electrochemical Science and Engineering, vol.10*, R. Alkire, et al., Editors. 2008, Wiley: Weinheim. p. 1-106.
97. Tuckerman, ME, A Chandra, and D Marx, *Structure and dynamics of OH-(aq).* Accounts of Chemical Research, 2006. **39**(2): p. 151-158.
98. Nominé, A, AV Nominé, NS Braithwaite, T Belmonte, and G Henrion, *High-Frequency-Induced Cathodic Breakdown during Plasma Electrolytic Oxidation.* Physical Review Applied, 2017. **8**(3).
99. Conway, BE and BV Tilak, *Interfacial processes involving electrocatalytic evolution and oxidation of H-2, and the role of chemisorbed H.* Electrochimica Acta, 2002. **47**(22-23): p. 3571-3594.
100. Reed, T, *Free Energy of Formation of Binary Compounds*. 1971, Cambridge, Ma: MIT Press.
101. Stull, DR and H Prophet, *JANAF Thermochemical Tables, NSRDS-NBS 37*. 1971: US Dept of Commerce, National Bureau of Standards.
102. Wang, YL, ZH Jiang, and ZP Yao, *Microstructure, bonding strength and thermal shock resistance of ceramic coatings on steels prepared by plasma electrolytic oxidation.* Applied Surface Science, 2009. **256**(3): p. 650-656.

103. Wang, YL, ZH Jiang, and ZP Yao, *Preparation and properties of ceramic coating on Q235 carbon steel by plasma electrolytic oxidation.* Current Applied Physics, 2009. **9**(5): p. 1067-1071.
104. Yerokhin, AL, VV Lyubimov, and RV Ashitkov, *Phase formation in ceramic coatings during plasma electrolytic oxidation of aluminium alloys.* Ceramics International, 1998. **24**(1): p. 1-6.
105. Charlu, TV, OJ Kleppa, and TB Reed, *High temperature Combustion Calorimetry 3. Enthalpies of Formation of Titanium Oxides.* Journal of Chemical Thermodynamics, 1974. **6**(11): p. 1065-1074.
106. Matykina, E, R Arrabal, P Skeldon, GE Thompson, P Wang, and P Wood, *Plasma electrolytic oxidation of a zirconium alloy under AC conditions.* Surface and Coatings Technology, 2010. **204**(14): p. 2142-2151.
107. Sandhyarani, M, N Rameshbabu, K Venkateswarlu, D Sreekanth, and C Subrahmanyam, *Surface morphology, corrosion resistance and in vitro bioactivity of P containing ZrO2 films formed on Zr by plasma electrolytic oxidation.* Journal of Alloys and Compounds, 2013. **553**: p. 324-332.
108. Apelfeld, AV, AM Borisov, BL Krit, VB Ludin, MN Polyansky, EA Romanovsky, SV Savushkina, IV Suminov, NV Tkachenko, AV Vinogradov, and VG Vostrikov, *The study of plasma electrolytic oxidation coatings on Zr and Zr-1% Nb alloy at thermal cycling.* Surface and Coatings Technology, 2015. **269**: p. 279-285.
109. He, SX, YL Ma, H Ye, XD Liu, ZY Dou, QD Xu, HJ Wang, and PC Zhang, *Ceramic oxide coating formed on beryllium by micro-arc oxidation.* Corrosion Science, 2017. **122**: p. 108-117.
110. Urbahs, A, M Urbaha, V Zujevs, K Savkovs, G Rijkuris, and P Kaunas Univ Technol, *Composition and Structure of Micro Arc Oxidation Coatings*, in *Transport Means 2013*. 2013, Kaunas Univ Technology Press: Kaunas. p. 101-105.
111. Lu, LH, JW Zhang, and DJ Shen, *Characterization of anatase coatings on NiTi shape memory alloy by plasma electrolytic oxidation method*, in *Frontiers of Manufacturing and Design Science Ii, Pts 1-6*, D. Sun, W.P. Sung, and R. Chen, Editors. 2012, Trans Tech Publications Ltd: Stafa-Zurich. p. 3837-3841.
112. Stojadinovic, S, N Tadic, NM Sisovic, and R Vasilic, *Real-time imaging, spectroscopy, and structural investigation of cathodic plasma electrolytic oxidation of molybdenum.* Journal of Applied Physics, 2015. **117**(23).
113. Rudnev, VS, DL Boguta, TP Yarovaya, and PM Nedozorov, *Coatings based on niobium oxides and phosphates formed on niobium alloy.* Protection of Metals and Physical Chemistry of Surfaces, 2014. **50**(3): p. 360-362.
114. Sowa, M, A Kazek-Kesik, A Krzakala, RP Socha, G Dercz, J Michalska, and W Simka, *Modification of niobium surfaces using plasma electrolytic oxidation in silicate solutions.* Journal of Solid State Electrochemistry, 2014. **18**(11): p. 3129-3142.
115. Stojadinovic, S, N Tadic, N Radic, P Stefanov, B Grbic, and R Vasilic, *Anodic luminescence, structural, photoluminescent, and photocatalytic properties of*

anodic oxide films grown on niobium in phosphoric acid. Applied Surface Science, 2015. **355**: p. 912-920.

116. Sowa, M, J Worek, G Dercz, DM Korotin, AI Kukharenko, EZ Kurmaev, SO Cholakh, M Basiaga, and W Simka, *Surface characterisation and corrosion behaviour of niobium treated in a Ca- and P-containing solution under sparking conditions.* Electrochimica Acta, 2016. **198**: p. 91-103.
117. Stojadinovic, S and R Vasilic, *Orange-red photoluminescence of Nb2O5: Eu3+, Sm3+ coatings formed by plasma electrolytic oxidation of niobium.* Journal of Alloys and Compounds, 2016. **685**: p. 881-889.
118. Ge, YL, YM Wang, YF Zhang, LX Guo, DC Jia, JH Ouyang, and Y Zhou, *The improved thermal radiation property of SiC doped microarc oxidation ceramic coating formed on niobium metal for metal thermal protective system.* Surface and Coatings Technology, 2017. **309**: p. 880-886.
119. Petkovic, M, S Stojadinovic, R Vasilic, and L Zekovic, *Characterization of oxide coatings formed on tantalum by plasma electrolytic oxidation in 12-tungstosilicic acid.* Applied Surface Science, 2011. **257**(24): p. 10590-10594.
120. Sowa, M, A Kazek-Kesik, RP Socha, G Dercz, J Michalska, and W Simka, *Modification of tantalum surface via plasma electrolytic oxidation in silicate solutions.* Electrochimica Acta, 2013. **114**: p. 627-636.
121. Strehlow, W and E Cook, *Compilation of Energy Band Gaps in Elemental and Binary Compound Semiconductors and Insulators.* Journal of Physical and Chemical Reference Data, 2009. **2**(1): p. 163-199.
122. Fromhold, AT and EL Cook, *Kinetics of Oxide Film Growth on Metal Crystals: Electron Tunneling and Ionic Diffusion.* Physical Review, 1967. **158**(3): p. 600-612.
123. Munoz, AG and JB Bessone, *Anodic oxide growth on aluminium surfaces modified by cathodic deposition of Ni and Co.* Thin Solid Films, 2004. **460**(1-2): p. 143-149.
124. Robertson, J, *High dielectric constant gate oxides for metal oxide Si transistors.* Reports on Progress in Physics, 2006. **69**(2): p. 327-396.
125. Hussein, RO, X Nie, and DO Northwood, *A spectroscopic and microstructural study of oxide coatings produced on a Ti–6Al–4V alloy by plasma electrolytic oxidation.* Materials Chemistry and Physics, 2012. **134**(1): p. 484-492.
126. Nomine, A, SC Troughton, AV Nomine, G Henrion, and TW Clyne, *High speed video evidence for localised discharge cascades during plasma electrolytic oxidation.* Surface and Coatings Technology, 2015. **269**: p. 125–130.
127. Troughton, SC, A Nomine, AV Nomine, G Henrion, and TW Clyne, *Synchronised Electrical Monitoring and High Speed Video of Bubble Growth associated with Individual Discharges During Plasma Electrolytic Oxidation.* Applied Surface Science, 2015. **359**: p. 405-411.
128. Troughton, SC, A Nomine, J Dean, and TW Clyne, *Effect of individual discharge cascades on the microstructure of plasma electrolytic oxidation coatings.* Applied Surface Science, 2016. **389**: p. 260-269.
129. Van, TB, SD Brown, and GP Wirtz, *Mechanism of Anodic Spark Deposition.* American Ceramic Society Bulletin, 1977. **56**(6): p. 563-566.

130. Kasalica, B, M Petkovic, I Belca, S Stojadinovic, and L Zekovic, *Electronic transitions during plasma electrolytic oxidation of aluminum.* Surface and Coatings Technology, 2009. **203**(20-21): p. 3000-3004.
131. Matykina, E, A Berkani, P Skeldon, and G Thompson, *Real-time imaging of coating growth during plasma electrolytic oxidation of titanium.* Electrochimica Acta, 2007. **53**(4): p. 1987-1994.
132. Yerokhin, AL, LO Snizhko, NL Gurevina, A Leyland, A Pilkington, and A Matthews, *Discharge characterisation in plasma electrolytic oxidation of aluminium.* Journal of Physics D: Applied Physics, 2003. **36**(17): p. 2110-2120.
133. Habazaki, H, S Tsunekawa, E Tsuji, and T Nakayama, *Formation and characterization of wear-resistant PEO coatings formed on β-titanium alloy at different electrolyte temperatures.* Applied Surface Science, 2012. **259**: p. 711-718.
134. Klapkiv, M, H Nykyforchyn, and V Posuvailo, *Spectral Analysis of an Electrolytic Plasma in the Process of Synthesis of Aluminium Oxide.* Materials Science, 1994. **30**: p. 333-343.
135. Klapkiv, M, *Simulation of synthesis of oxide-ceramic coatings in discharge channels of a metal-electrolyte system* Materials Science, 1999. **35**: p. 279-283.
136. Klapkiv, MD, *State of an electrolytic plasma in the process of synthesis of oxides based on aluminum.* Materials Science, 1995. **31**: p. 494-499.
137. Jovović, J, S Stojadinović, NM Šišović, and N Konjević, *Spectroscopic characterization of plasma during electrolytic oxidation (PEO) of aluminium.* Surface and Coatings Technology, 2011. **206**(1): p. 24-28.
138. Hussein, RO, X Nie, DO Northwood, A Yerokhin, and A Matthews, *Spectroscopic study of electrolytic plasma and discharging behaviour during the plasma electrolytic oxidation (PEO) process.* Journal of Physics D: Applied Physics, 2010. **43**(10).
139. Jovović, J, S Stojadinović, NM Šišović, and N Konjević, *Spectroscopic study of plasma during electrolytic oxidation of magnesium- and aluminium-alloy.* Journal of Quantitative Spectroscopy and Radiative Transfer, 2012. **113**(15): p. 1928-1937.
140. Stojadinović, S, J Jovović, M Petković, R Vasilić, and N Konjević, *Spectroscopic and real-time imaging investigation of tantalum plasma electrolytic oxidation (PEO).* Surface and Coatings Technology, 2011. **205**(23–24): p. 5406-5413.
141. Stojadinović, S, R Vasilić, M Petković, B Kasalica, I Belča, A Žekić, and L Zeković, *Characterization of the plasma electrolytic oxidation of titanium in sodium metasilicate.* Applied Surface Science, 2013. **265**(0): p. 226-233.
142. Yerokhin, AL, LO Snizhko, NL Gurevina, A Leyland, A Pilkington, and A Matthews, *Spatial characteristics of discharge phenomena in plasma electrolytic oxidation of aluminium alloys.* Surface and Coatings Technology, 2004. **177**: p. 779-783.
143. Cheng, Y, F Wu, E Matykina, P Skeldon, and GE Thompson, *The influences of microdischarge types and silicate on the morphologies and phase compositions of plasma electrolytic oxidation coatings on Zircaloy-2.* Corrosion Science, 2012. **59**: p. 307-315.

144. Matykina, E, R Arrabal, P Skeldon, and GE Thompson, *Optimisation of the plasma electrolytic oxidation process efficiency on aluminium.* Surface and Interface Analysis, 2010. **42**(4): p. 221-226.
145. Matykina, E, R Arrabal, A Pardo, M Mohedano, B Mingo, I Rodriguez, and J Gonzalez, *Energy-efficient PEO process of aluminium alloys.* Materials Letters, 2014. **127**: p. 13-16.
146. Snizhko, LO, AL Yerokhin, A Pilkington, NL Gurevina, DO Misnyankin, A Leyland, and A Matthews, *Anodic processes in plasma electrolytic oxidation of aluminium in alkaline solutions.* Electrochimica Acta, 2004. **49**: p. 2085–2095.
147. Snizhko, LO, AL Yerokhin, NL Gurevina, VA Patalakha, and A Matthews, *Excessive Oxygen Evolution during Plasma Electrolytic Oxidation of Aluminium.* Thin Solid Films, 2007. **516**: p. 460-464.
148. Snezhko, LA, AL Erokhin, OA Kalinichenko, and DA Misnyankin, *Hydrogen Release on the Anode in the Course of Plasma Electrolytic Oxidation of Aluminium.* Materials Science, 2016. **52**(3): p. 421-430.
149. Cheng, YL, ZM Peng, XQ Wua, JH Cao, P Skeldon, and GE Thompson, *A comparison of plasma electrolytic oxidation of Ti-6Al-4V and Zircaloy-2 alloys in a silicate-hexametaphosphate electrolyte.* Electrochimica Acta, 2015. **165**: p. 301-313.
150. Cheng, YL, T Wang, SX Li, YL Cheng, JH Cao, and HJ Xie, *The effects of anion deposition and negative pulse on the behaviours of plasma electrolytic oxidation (PEO)-A systematic study of the PEO of a Zirlo alloy in aluminate electrolytes.* Electrochimica Acta, 2017. **225**: p. 47-68.
151. Sengupta, SK, AK Srivastava, and R Singh, *Contact glow discharge electrolysis: A study on its origin in the light of the theory of hydrodynamic instabilities in local solvent vaporisation by Joule heating during electrolysis.* Journal of Electroanalytical Chemistry, 1997. **427**(1-2): p. 23-27.
152. Sengupta, SK, R Singh, and AK Srivastava, *A study on the origin of nonfaradaic behavior of anodic contact glow discharge electrolysis - The relationship between power dissipated in glow discharges and nonfaradaic yields.* Journal of the Electrochemical Society, 1998. **145**(7): p. 2209-2213.
153. Wang, JH, MH Du, FZ Han, and J Yang, *Effects of the ratio of anodic and cathodic currents on the characteristics of micro-arc oxidation ceramic coatings on Al alloys.* Applied Surface Science, 2014. **292**: p. 658-664.
154. Rakoch, AG, AA Gladkova, Z Linn, and DM Strekalina, *The evidence of cathodic micro-discharges during plasma electrolytic oxidation of light metallic alloys and micro-discharge intensity depending on pH of the electrolyte.* Surface and Coatings Technology, 2015. **269**: p. 138-144.
155. Sah, SP, E Tsuji, Y Aoki, and H Habazaki, *Cathodic pulse breakdown of anodic films on aluminium in alkaline silicate electrolyte - Understanding the role of cathodic half-cycle in AC plasma electrolytic oxidation.* Corrosion Science, 2012. **55**: p. 90-96.

156. Nomine, A, J Martin, G Henrion, and T Belmonte, *Effect of cathodic micro-discharges on oxide growth during plasma electrolytic oxidation (PEO).* Surface and Coatings Technology, 2015. **269**: p. 131-137.
157. Fatkullin, AR, EV Parfenov, A Yerokhin, DM Lazarev, and A Matthews, *Effect of positive and negative pulse voltages on surface properties and equivalent circuit of the plasma electrolytic oxidation process.* Surface and Coatings Technology, 2015. **284**: p. 427-437.
158. Rogov, AB, A Yerokhin, and A Matthews, *The Role of Cathodic Current in Plasma Electrolytic Oxidation of Aluminum: Phenomenological Concepts of the "Soft Sparking" Mode.* Langmuir, 2017. **33**(41): p. 11059–11069.
159. Wang, HY, RF Zhu, YP Lu, GY Xiao, J Ma, and YF Yuan, *Preparation and Mechanism of Controllable Micropores on Bioceramic TiO2 Coatings by Plasma Electrolytic Oxidation.* Surface Review and Letters, 2013. **20**(5).
160. Kharanagh, VJ, MAF Sani, and E Rafizadeh, *Effect of current frequency on coating properties formed on aluminised steel by plasma electrolytic oxidation.* Surface Engineering, 2014. **30**(3): p. 224-228.
161. Zou, B, GH Lu, GL Zhang, and YY Tian, *Effect of current frequency on properties of coating formed by microarc oxidation on AZ91D magnesium alloy.* Transactions of Nonferrous Metals Society of China, 2015. **25**(5): p. 1500-1505.
162. Yerokhin, A, EV Parfenov, and A Matthews, *In situ impedance spectroscopy of the plasma electrolytic oxidation process for deposition of Ca- and P-containing, coatings on Ti.* Surface and Coatings Technology, 2016. **301**: p. 54-62.
163. Slonova, AI and OP Terleeva, *Morphology, structure, and phase composition of microplasma coatings formed on Al-Cu-Mg alloy.* Protection of Metals, 2008. **44**(1): p. 65-75.
164. Melhem, A, G Henrion, T Czerwiec, JL Briancon, T Duchanoy, F Brochard, and T Belmonte, *Changes induced by process parameters in oxide layers grown by the PEO process on Al alloys.* Surface and Coatings Technology, 2011. **205**: p. S133-S136.
165. Matykina, E, R Arrabal, A Mohamed, P Skeldon, and GE Thompson, *Plasma electrolytic oxidation of pre-anodized aluminium.* Corrosion Science, 2009. **51**(12): p. 2897-2905.
166. Matykina, E, R Arrabal, P Skeldon, GE Thompson, and P Belenguer, *AC PEO of aluminium with porous alumina precursor films.* Surface and Coatings Technology, 2010. **205**(6): p. 1668-1678.
167. Gebarowski, W and S Pietrzyk, *Growth Characteristics of the Oxide Layer on Aluminium in the Process of Plasma Electrolytic Oxidation.* Archives of Metallurgy and Materials, 2014. **59**(1): p. 407-411.
168. Gebarowski, W and S Pietrzyk, *Influence of the Cathodic Pulse on the Formation and Morphology of Oxide Coatings on Aluminium Produced by Plasma Electrolytic Oxidation* Archives of Metallurgy and Materials, 2013. **58**(1): p. 241-245.

169. Hamdan, A, C Noel, F Kosior, G Henrion, and T Belmonte, *Dynamics of bubbles created by plasma in heptane for micro-gap conditions*. Journal of the Acoustical Society of America, 2013. **134**(2): p. 991-1000.